FINAL REPORT

NASA GRANT NAG8-724

Period of Performance
7/1/88-6/30/91

VIBRATION ISOLATION TECHNOLOGY: SENSITIVITY OF SELECTED CLASSES OF EXPERIMENTS TO RESIDUAL ACCELERATIONS

Principal Investigator

J. IWAN D. ALEXANDER

Center for Microgravity and Materials Research
The University of Alabama in Huntsville
Huntsville, Alabama 35899

1. Introduction

This is the final report for the period of performance 7/1/88-6/30/92. The project was originally proposed for three years. Funds were not made available for the third year. A no-cost extension of the second year was requested in order to complete as much of the original project as possible.

2. Summary

The following tasks were described in the original and continuation proposals.

Task 1:	Order of Magnitude Estimates
Task 2 :	Thermo-capillary Convection - Two Dimensional (fixed planar surface)
Task 3:	Thermo-capillary Convection - Three Dimensional and Axisymmetric
Task 4:	Liquid Bridge/ Floating-Zone Sensitivity
Task 6:	Transport in Closed Containers
Task 7 :	Interaction: Design and Development Stages
Task 8:	Interaction: Testing Flight Hardware
Task 9:	Reporting

Work was completed on all aspects of these tasks despite the lack of funding for the third year. The only part of the original proposal which was not addressed was the effect of vibration on diffusion experiments.

A review of work related to experiment sensitivity to residual acceleration has been published and a copy of the article is attached in **Appendix 1.** In the third semi-annual report we stated that Task 2 should complete by June-July of 1990 (i.e. earlier than originally anticipated). Since that report was issued NASA MSFC extended the P.O.P. of the second year's work to June 1991 as continuation funds are not yet available. We completed Task 2 during this period and a paper describing the results is in preparation for journal publication. (Task 2 involves an analysis of the residual acceleration sensitivity of thermocapillary driven flow in a 2-D rectangular region. The free surface is held planar.) The work is summarized in **Section 4.**

Task 3, which involves the examination of axisymmetric thermocapillary convection has been started early in the process of developing a method for the examination of non-isothermal liquid bridge. A code for the axisymmetric isothermal and non-isothermal (i.e. thermocapillary driven convection is included along with a deformable free surface) liquid bridge sensitivity analysis has been developed and a comparison with 1-D results has been made. These results will be reported in **Section 3.**

Five papers, and one extended abstract, summarizing work carried out entirely (or partly*) under the VIT project have been accepted for publication:

1. *Microgravity Experiment Sensitivity to Residual Accelerations: A Review*, Microgravity Science and Technology,III, No.2, 52-68, 1990. **(See Appendix 1)**
2. *The Sensitivity of a Liquid Bridge to Axial Vibration*, with Y. Q. Zhang, Physics of Fluids, A 2, 1966-1974, 1990. **(See Appendix 2)**

3.* *Bridgman Crystal Growth in Low Gravity: A Scaling Analysis*, with F. Rosenberger, in Low Gravity Fluid Dynamics and Transport Phenomena, R. L. Sani and J. N. Koster (eds.), (AIAA, Washington D.C., 1990) pp. 87-117. **(See Appendix 3)**

4. *A Finite Difference Method for a Model Float Zone Free Surface Problem*, with Y. Q. Zhang, to appear in the Journal of Numerical Methods in Fluids, 1990. **(See Appendix 4)**

5. *The Sensitivity of a Non-Isothermal Liquid Bridge to Residual Acceleration*, with Y. Q. Zhang, to appear in the Proceedings of the International Union of Theoretical and Applied Mechanics Symposium on Microgravity Fluid Mechanics, Bremen, September, 1991. **(See Appendix 5)**
6. *The Sensitivity of a Non-Isothermal Liquid Bridge to Residual Acceleration*, to appear as an extended abstract of the above article in Microgravity Science and Technology, August/September 1991.

A paper describing our work on 2D thermocapillary flow is in preparation. Results of work for the VIT project have been (will be) presented at the following conferences and workshops and invited lectures:

1. *Sensitivity of Liquid Bridge and Floating Zone Shapes Subject to Axial Vibrations,* presented at the Alabama Materials Research Conference, University of Alabama in Huntsville, Sept. 20th and 21st 1989.
2. *Sensitivity of Thermocapillary Flow to Residual Acceleration,* presented at the Alabama Materials Research Conference, University of Alabama in Huntsville, Sept. 20th and 21st 1989.
3. *Experiment Sensitivity: Determination of Requirements for Vibration Isolation,* Proceedings of the NASA Workshop on Vibration Isolation Technology Microgravity Science Experiments, Sept. 28-29 1988.
4. *Sensitivity of Crystal Growth Experiments to Residual Accelerations,* presented at the Gordon Conference on Gravitational Effects in Materials and Processes, July 30 -August 4, 1989, Plymouth State College, Plymouth, New Hampshire.
5. *The Sensitivity of a Non-Isothermal Liquid Bridge to Residual Acceleration*, with Y. Q. Zhang, to be presented at the IUTAM Symposium on Microgravity Fluid Mechanics, Bremen, September, 1991.

3. Liquid Bridge/Floating-Zone Sensitivity

This section refers to Task 4 and concerns the sensitivity of an *isothermal liquid bridge* to axial acceleration and was been extended to non-isothermal situations covered under Task 3. The first annual report contained a detailed description of a one-dimensional model and the sensitivity results obtained using that model, this work was subsequently been refined published in the journal *Physics of Fluids*. A reprint is attached in **Appendix 2.**

The 1-D model had been used to examine the sensitivity of an isothermal liquid bridge to axial vibration. The results indicate that the zone is most sensitive to accelerations with frequencies close to or equal to the lowest natural frequency of the zone. For the purposes of this project it is most useful to assess the sensitivity of the zone in terms of predicted Space Station and/or Spacelab environments. For the cases examined, we have seen that frequencies around the 0.1 Hz range appear to be the most sensitive. The low frequency ($< 10^{-2}$ Hz) acceleration environment predicted for the space station[1] should not exceed levels of 10^{-5} g. Higher frequencies can be associated with acceleration magnitudes of up to 10^{-2} g. In terms of these predicted levels, or those measured on past missions[1], the practical sensitivity range is restricted to disturbances with frequencies ranging from

10^{-1} - 10 Hz.

During the second year, work on a full axisymmetric calculation started. A model was developed for both isothermal and non-isothermal bridges. The adaptation of two numerical algorithms for the solutions of these problems has been successfully completed and preliminary calculations have been made.

The early stages of development and verification of the isothermal code (and the ability of the method to handle buoyancy-driven flows in fixed geometries) was outlined in the third semi-annual report and an updated account is given below.

For the solution of the axisymmetric isothermal and non-isothermal problems our objectives were:

1. To develop a full numerical model of the axisymmetric free surface response of an isothermal liquid bridge (suspended between rigid disks of equal radius) subject to axial vibration and to compare it to the sensitivities predicted by a previously developed 1-D model
2. To develop a full numerical model of the axisymmetric free surface response of a non-isothermal liquid bridge subject to axial vibration. The presence of a temperature gradient gives rise to a thermocapillary flow. We wish to investigate the interaction between the free surface motion induced by vibration, and the surface-driven flow. Interaction of these flows with internal buoyancy-driven flow driven by the vibration is expected to be negligible but is included in the basic model.

Any algorithm that is capable of solving the equations governing the second objective must be capable of solving the first objective. Added complications result from the fact that the coupled heat transfer and Navier-Stokes-Boussinesq equations must also be solved to satisfy the second objective. In addition, it is convenient to use steady-state solutions for thermocapillary convection as initial conditions. As a result we have developed two algorithms which are based on the same numerical methods; one is used to compute steady-state velocity and temperature fields and free surface shape for the following problem, the other is used to calculate the time dependent response.

3.1 Steady State interface shapes and thermocapillary convection

Consider a cylindrical liquid zone held between two parallel coaxial circular rigid disks (radius = R_o) separated by a distance L. The liquid is a non-isothermal incompressible Newtonian fluid. The bridge is held between the disks by surface tension. The free surface of the bridge is a gas-liquid interface and is described by $r=R(z,t)$. The two disks are maintained at a constant temperature T_o. Surface heating is provided through a parabolic ambient temperature $T_\infty(z)$ and the heat transfer coefficient at the free surface is denoted by h. In addition, we make the assumptions that the gravitational acceleration is parallel to the cylinder axis and that the velocity, temperature and free surface deformation are axisymmetric. Furthermore, we let the surface tension at the free surface vary linearly with temperature and assume that the Boussinesq approximation holds.

The governing equations are made dimensionless by scaling length, time and velocity with R_o, R_o/U^* and U^*, respectively . Here U^* is a characteristic velocity given by

$$U^* = \frac{|\gamma|\Delta T}{\mu}$$

where $\Delta T=T_{max}-T_{min}$ represents the maximum temperature difference at the surface, $|\gamma|$ is the absolute value of the derivative of the surface tension with respect to temperature, and μ is the dynamic viscosity. We shall refer to a "half zone" model when the ambient temperature has extrema at the end disks and a "full zone" when the temperature maximum occurs between the disks. For a full zone we shall take T_{max} to be $T_\infty(0)$, and T_{min} to be T_o, where $\Lambda = L/R_o$ is the aspect ratio.

The non-dimensional pressure is

$$p = \frac{p^* + \rho_0 g z}{\rho_0 U^{*2}} R_0$$

where p^* is the dimensional pressure, g is the gravitational acceleration, z is the dimensionless axial coordinate, and ρ_0 is the density corresponding to the reference temperature. The temperature is rendered dimensionless using $T_{max} - T_{min}$. With these scales the dimensionless equations in a cylindrical coordinate system can be written as

$$\frac{1}{r}\frac{\partial(ru)}{\partial r} + \frac{\partial w}{\partial z} = 0 \, , \tag{1}$$

$$u\frac{\partial u}{\partial r} + w\frac{\partial u}{\partial z} = -\frac{\partial p}{\partial r} + \frac{1}{Re}\left(\frac{\partial^2 u}{\partial r^2} + \frac{1}{r}\frac{\partial u}{\partial r} + \frac{\partial^2 u}{\partial z^2} - \frac{u}{r^2}\right) , \tag{2}$$

$$u\frac{\partial u}{\partial r} + w\frac{\partial w}{\partial z} = -\frac{\partial p}{\partial z} + \frac{1}{Re}\left(\frac{\partial^2 w}{\partial r^2} + \frac{1}{r}\frac{\partial w}{\partial r} + \frac{\partial^2 w}{\partial z^2}\right) + \frac{Gr}{Re^2}T, \tag{3}$$

$$u\frac{\partial T}{\partial r} + w\frac{\partial T}{\partial z} = \frac{1}{Ma}\left(\frac{\partial^2 T}{\partial r^2} + \frac{1}{r}\frac{\partial T}{\partial r} + \frac{\partial T}{\partial z^2}\right) , \tag{4}$$

where the Reynolds number, Re, Marangoni number, Ma and Grashof number Gr, are respectively

$$Re = \frac{R_o U^*}{\nu} \quad , \quad Ma = \frac{|\gamma|\Delta T R_o}{\mu\kappa} \, , \quad Gr = \frac{g\beta\Delta T R_o^3}{\nu^2} \, .$$

Here, ν is the kinematic viscosity, κ is the thermal diffusivity, β is the volume thermal expansion coefficient, and g is the gravitational acceleration. At the disks, the boundary conditions are

$$u = w = T = 0, \text{ at } z = \pm\frac{\Lambda}{2}. \tag{5}$$

The symmetry conditions at the centerline r = 0 are

$$u = \frac{\partial w}{\partial r} = \frac{\partial T}{\partial r} = . \tag{6}$$

The free surface is located at $r = R(z)$ where the boundary conditions are:

$$p - Gz + \lambda = \frac{2Re^{-1}}{1+\left(\frac{\partial R}{\partial z}\right)^2}\left[\frac{\partial u}{\partial r} + \left(\frac{\partial R}{\partial z}\right)^2 \frac{\partial w}{\partial z} - \frac{\partial R}{\partial z}\left(\frac{\partial w}{\partial r} + \frac{\partial u}{\partial z}\right)\right] +$$

$$\frac{Re^{-1}\left(C_o^{-1} - T\right)}{\left[1+\left(\frac{\partial R}{\partial z}\right)^2\right]^{3/2}}\left[\frac{1+\left(\frac{\partial R}{\partial z}\right)^2}{R} - \frac{\partial^2 R}{\partial z^2}\right], \tag{7}$$

$$\left[1 - \left(\frac{\partial R}{\partial z}\right)^2\right]\left(\frac{\partial u}{\partial z} + \frac{\partial w}{\partial r}\right) + 2\frac{\partial R}{\partial z}\left(\frac{\partial u}{\partial r} - \frac{\partial w}{\partial z}\right) = -\left[1+\left(\frac{\partial R}{\partial z}\right)^2\right]^{\frac{1}{2}}\left(\frac{\partial T}{\partial z} + \frac{\partial R}{\partial z}\frac{\partial T}{\partial r}\right), \tag{8}$$

$$u + w\frac{\partial R}{\partial z} = 0 \ , \tag{9}$$

$$\frac{1}{\left(1 + \left(\frac{\partial R}{\partial z}\right)^2\right)^{\frac{1}{2}}}\left(\frac{\partial T}{\partial r} - \frac{\partial R}{\partial z}\frac{\partial T}{\partial z}\right) + Bi\left(T - T_\infty\right) = 0, \tag{10}$$

where

$$C_o = \frac{\gamma \Delta T}{\gamma_o}, \quad Bi = \frac{hR_o}{\kappa}, \quad G = \frac{gR_o}{U^{*2}}$$

and are, respectively, the capillary number, Biot number, and dimensionless gravitational acceleration, γ_o is the mean surface tension, and κ is thermal conductivity. The force balance at the free surface in the normal and tangential directions are given by eqs. (7) and (8), respectively. Equation (9) is the kinematic boundary condition at the liquid-gas interface. The thermal boundary condition at the interface is given by equation (10) in which the equivalent heat transfer coefficient h contains the effect of the radiant and convective heat transfer. The constant λ in (7) represents a dimensionless reference pressure difference[2,3] across the interface. In model float zone systems with fixed rigid endwalls, such as the one discussed here, λ is determined by the following constant volume constraint

$$V = \int_{\frac{-\Lambda}{2}}^{\frac{\Lambda}{2}} \pi R^2(z) dz = V_o \equiv \text{constant} . \tag{11}$$

Finally, the condition that the contact lines between the liquid end disks are fixed is

$$R = 1 \text{ at } z = \pm \Lambda/2. \tag{12}$$

Numerical Method

In the case of a two dimensional axisymmetric flow, the governing equations can be simplified by introducing the stream function, ψ, and vorticity, ω, as new dependent variables:

$$u = \frac{1}{r}\frac{\partial\psi}{\partial z}, \quad V = \frac{1}{r}\frac{\partial\psi}{\partial r} \tag{13}$$

$$\omega = \frac{\partial u}{\partial z} - \frac{\partial w}{\partial r} \quad . \tag{14}$$

From (13), (12), (2) and (3) the following equation is obtained for ω

$$u\frac{\partial\omega}{\partial r} + w\frac{\partial\omega}{\partial z} - \frac{\omega u}{r} = \frac{1}{Re}\left(\frac{\partial^2\omega}{\partial r^2} + \frac{1}{r}\frac{\partial\omega}{\partial r} + \frac{\partial^2\omega}{\partial z^2}\right) - \frac{1}{Re}\frac{\omega}{r^2} - \frac{Gr}{Re^2}\frac{\partial T}{\partial r} \quad . \tag{15}$$

Substitution of (13) into (14) yields

$$r\omega = \frac{\partial^2\psi}{\partial r^2} - \frac{1}{r}\frac{\partial\psi}{\partial r} + \frac{\partial^2\psi}{\partial z^2} \, . \tag{16}$$

The original set of three equations governing mass and momentum has been reduced to two equations governing the steam function and vorticity.

The steady free boundary problem for cylindrical liquid zone is solved iteratively, since the location of the free surface is *a priori* unknown. To obtain a solution we adopt a Picard iterative procedure[4] as follows:

1. Guess the free surface shape for the initial iterate;
2. Obtain the approximate temperature and velocity fields by transforming the governing equations and boundary conditions to a circular cylindrical domain via a non-orthogonal transformation and solve them using a pseudo-unsteady semi-implicit method;
3. Obtain the pressure at the free surface by integrating the transformed momentum equation;
4. Use the normal force balance condition at the free surface to decide how to update the free surface location;
5. Return to step 2. Repeat until convergence is obtained.

Non-orthogonal Transformation

The region occupied by the liquid zone is transformed into a fixed circular cylindrical computational region using a non-orthogonal coordinate transformation, i.e.

$$\eta = z \quad , \quad \xi = \frac{r}{R(z)} \quad . \tag{17}$$

It then follows that

$$\frac{\partial}{\partial r} \rightarrow \frac{1}{R}\frac{\partial}{\partial \zeta}\ , \ \frac{\partial}{\partial z} \rightarrow \frac{\partial}{\partial \eta} - \frac{\zeta}{R}\frac{\partial R}{\partial \eta}\frac{\partial}{\partial \zeta}\ . \tag{18}$$

The advantage of this transformation is that the free boundary coincides exactly with a coordinate line in a computational grid and regeneration of mesh during the outer iteration is avoided. For the sake of simplicity, a pseudo-unsteady method in association with a semi-implicit discretization with respect to time is used.

The resulting system of governing equations is solved as the time (pseudo) derivatives of T, ψ and $\omega \rightarrow 0$. The discretization in time employs an explicit Adams-Bashforth scheme for the nonlinear convective terms and the implicit scheme for the viscous terms. Other terms in the equation are treated explicitly. For spatial discretization, central differences are used. The A.D.I. form for the vorticity equation is then

$$\begin{aligned} &\frac{2}{\Delta\tau}\left(\omega_{ij}^{n+1/2} - \omega_{ij}^{n}\right) + \frac{3}{2}(L_2\omega)_{ij}^{n} - \frac{1}{2}(L_2\omega)_{ij}^{n-1} - \frac{1}{Re}\left(\frac{\partial^2\omega}{\partial\eta^2}\right)_{ij}^{n} \\ &\qquad - \frac{1}{Re}\left(A\frac{\partial^2\omega}{\partial\eta^2} + B\frac{\partial\omega}{\partial\zeta}\right)_{ij}^{n+1} + (S_2)_{ij}^{n} = 0\ , \end{aligned} \tag{19}$$

$$\begin{aligned} &\frac{2}{\Delta t}\left(\omega_{ij}^{n+1} - \omega_{ij}^{n+1/2}\right) + \frac{3}{2}(L_2\omega)_{ij}^{n} - \frac{1}{2}(L_2\omega)_{ij}^{n-1} - \frac{1}{Re}\left(\frac{\partial^2\omega}{\partial\eta^2}\right)_{ij}^{n+1} \\ &\qquad - \frac{1}{Re}\left(A\frac{\partial^2\omega}{\partial\zeta^2} + B\frac{\partial\omega}{\partial\zeta}\right)_{ij}^{n+1/2} + (S_2)_{ij}^{n} = 0\ . \end{aligned} \tag{20}$$

where

$$L_1 = \frac{1}{R^2\zeta}\left(\frac{\partial\psi}{\partial\eta}\frac{\partial}{\partial\zeta} - \frac{\partial\psi}{\partial\zeta}\frac{\partial}{\partial\eta}\right),$$

$$L_2 = \frac{1}{R^2\zeta}\left(\frac{\partial\psi}{\partial\eta}\frac{\partial}{\partial\zeta} - \frac{\partial\psi}{\partial\zeta}\frac{\partial}{\partial\eta}\right) - \frac{u}{R\zeta}\ ,$$

$$S_1 = -\frac{1}{Ma}C\frac{\partial^2 T}{\partial\eta\partial\zeta}\ , \ S_2 = \frac{1}{Re}\left(\frac{\omega}{R^2\zeta} - C\frac{\partial^2\omega}{\partial\eta\partial\zeta}\right) + \frac{Gr}{Re^2}\frac{1}{R}\frac{\partial T}{\partial\zeta}\ ,$$

$$S_3 = -C\frac{\partial^2\psi}{\partial\eta\partial\zeta} + R\zeta w\ .$$

Here the superscript n+1/2 denotes the intermediate step associated with the ADI method[7]. The velocities (at the nth step) are taken from the values at the previous step values. Thus, except for the thermal condition at free boundary, these are Dirichlet boundary conditions. The heat transfer equation is also discretized in an ADI form. The resulting system of discretized equations is solved using a factorization method[5].

We define a steady state to occur reached when the residuals ($\partial\omega/\partial\tau$, $\partial T/\partial\tau$, $\partial\psi/\partial\tau$) of the vorticity, energy and stream function equations are less than 10^{-7}. That is,

$$\max\left|\frac{F_{ij}^{n+1} - F_{ij}^{n}}{\Delta\tau}\right| < 10^{-7} \; . \tag{21}$$

Where F represents the vorticity, temperature and stream function at the n+1th and nth iterative step. The numerical solution is second order accurate in space.

Having computed the vorticity and stream functions for a given surface shape, it remains to iterate on the condition for the balance of force normal to the surface in order to obtain the final steady surface shape. In addition, the shape must satisfy the volume constraint (11) and boundary conditions.

Two iterative schemes for determining the interface are discussed in this section. In both schemes, the new velocities and temperatures are taken from the current calculated values and the pressure at interface can be obtained by taking the η component of momentum equation and integrating with respect to η. This yields

$$p = \int_0^{\eta}\left[-\frac{1}{R}\left(\frac{\partial\psi}{\partial s}\frac{\partial w}{\partial\zeta} - \frac{\partial\psi}{\partial\zeta}\frac{\partial w}{\partial s}\right) + \frac{1}{Re}\left(\frac{\partial^2 w}{\partial s^2} + A\frac{\partial^2 w}{\partial\zeta^2} + B\frac{\partial w}{\partial\zeta} + C\frac{\partial^2 w}{\partial s\partial\zeta}\right) + \frac{Gr}{Re^2}T\right]\left(1 + \left(\frac{\partial R}{\partial s}\right)^2\right)^{1/2} ds \, .$$

The first scheme (I) involves successive approximation by the direct solution of

$$p - G\eta + \lambda - \frac{2\,Re^{-1}}{1 + \left(\frac{\partial R}{\partial\eta}\right)^2}\left[\frac{1}{R}\frac{\partial u}{\partial\zeta} + \left(\frac{\partial R}{\partial\eta}\right)^2\left(\frac{\partial w}{\partial\eta} - \frac{1}{R}\frac{\partial R}{\partial\eta}\frac{\partial w}{\partial\zeta}\right) - \frac{\partial R}{\partial\eta}\left(\frac{1}{R}\frac{\partial w}{\partial\zeta} + \frac{\partial u}{\partial\eta} - \frac{1}{R}\frac{\partial R}{\partial\eta}\frac{\partial u}{\partial\zeta}\right)\right]$$

$$= Re^{-1}\left(C_o^{-1} - T\right)\frac{1}{\left[1 + \left(\frac{\partial R}{\partial\eta}\right)^2\right]^{3/2}}\left[\frac{1 + \left(\frac{\partial R}{\partial\eta}\right)^2}{R} - \frac{\partial^2 R}{\partial\eta^2}\right] . \tag{22}$$

This scheme is based on the following principle. A shape is assigned to the free surface with the calculated pressure, velocity and temperature. An initial guess for the pressure constant λ is made. The new interface shape is then determined directly from (22). The integral (11) is then evaluated to check whether the volume constraint has been satisfied. If it is not satisfied an inner iteration is made using a Newton-Raphson procedure to calculate the following improved estimate of λ:

$$\lambda^{k+1} = \lambda^{k} - \left(\frac{\partial V}{\partial\lambda}\right)^{-1}\Delta V \quad , \tag{23}$$

where

$$\Delta V = \int_{-\Lambda/2}^{\Lambda/2} \pi R^2 d\eta - V_o . \tag{24}$$

The above procedure for determining λ is quite effective and is repeated until the volume constraint is satisfied. $R(\eta)$ is then updated. New velocity, pressure and temperature fields are calculated using the updated value of $R(\eta)$. The outer iteration is repeated until

$$\max \left| R^{n+1} - R^n \right| < \varepsilon \quad , \tag{25}$$

where we take $\varepsilon = 10^{-4}$.

The second scheme (II), used by Ryskin and Leal[7], uses the residual of the normal component of force balance to drive the shape to its steady position. This is equivalent to equating the residual with an artificial capillary force. This effective force causes a local displacement of the interface in the direction of the force. The magnitude of the local displacement is proportional to this force. The interface shape at each iteration is thus modified so as to reduce the residual until the condition (22) is met. It follows that at each iteration the improved interface shape is given by

$$R_j^{m+1} = R^m + \alpha Ex_j, \tag{26}$$

where Ex_j is the residual of the force balance equation at the jth surface location and the constant coefficient α is determined by numerical experiment. In order to ensure convergence, α should be small. We found that the values of α which led to rapid convergence depended on the product of Re^{-1} and C_o^{-1}. If α is chosen to be too small the amount of CPU time used increases substantially.

The change in volume between the mth and (m+1)th iteration can be found from the volume constraint (11) and equation (26) and neglecting higher order terms, i.e.

$$\int_{-\Lambda/2}^{\Lambda/2} Ex_j \, R_j^m \, d\eta = 0. \tag{27}$$

The pressure constant λ is contained in Ex_j and is obtained by satisfying (24). Even then the liquid bridge may still change volume slightly at each iteration owing to numerical error and higher-order effects. These small changes can accumulate and eventually result in a gross error. To prevent this, the formula (26) is modified to

$$R_j^{m+1} = R_j^m \left(\frac{V_o}{V_m} \right)^{1/2} + \alpha Ex_j \ . \tag{28}$$

We have used the method described earlier to examine the influence of various parameters on momentum and heat transport and meniscus shape. In addition, a comparison between the results obtained with the combined scheme and those of Hyer et al.[7] has been made.

A parametric study of the effects of varying the temperature difference ΔT (keeping

Ma/Gr fixed), Marangoni number, Ma, Nusselt number, Nu, aspect ratio, Λ, and Grashof number, Gr, has been made and are described in **Appendix 4.**

Unsteady interface shapes (g-jitter response) for isothermal and non-isothermal bridges.

To obtain the time dependent internal and free surface response of isothermal and non-isothermal liquid bridges to axial acceleration we employed the following procedure. To obtain a solution we follow the approach of Kang and Leal[8] and adopt a Picard iterative procedure[4] as follows:

1. Use the free surface shape, stream function, vorticity, velocities, and temperature computed from the steady calculation as the initial condition. (For the isothermal case the liquid bridge is initially static with a free surface shape given by the prevailing steady axial acceleration ;
2. To obtain the temperature and velocity fields at the next time step we transform the governing equations and boundary conditions to a circular cylindrical domain via a non-orthogonal transformation and solve them using a semi-implicit Adams-Bashforth/Crank-Nicolson time discretization. Centered differences are used for the spatial approximation ;
3. Obtain the pressure at the free surface by integrating the transformed momentum equation;
4. Use the normal force balance condition at free surface to determine the updated free surface location at the new time step;
5. Return to step 2. Repeat until convergence is obtained.

Our early results showed good agreement between the predictions of the 1-D isothermal model and the axisymmetric calculations (see Table 1) Further calculations have been made and for the cases examined to date these findings are confirmed. For the cases examined to date, the effect of thermo-capillary convection on the response of the free surface shape has been found to be negligible Our results are given in **Appendix 5**

Table 1: Comparison of Bridge Radii (R) (to 3 decimal places) at two locations predicted by 1-D and axisymmetric (2D) models, $g=1.42\times10^{-3}$ ms^{-2}, the frequency of axial vibration is 3 Hz.

Time (s)	0	0.22	0.39	0.48
$R_{1\text{-}D}$	1.001	1.149	1.017	0.891
R_{axisym}	1.001	1.146	0.998	0.919
$R_{1\text{-}D}$	1.001	1.159	0.994	0.909
R_{axisym}	1.001	1.150	0.986	0.929

4. Thermocapillary Convection -2D

The work for Task 2 involves the solution of the incompressible Navier-Stokes - Boussinesq equations in a rectangular region with one "free surface" boundary condition which equates the tangential viscous force at the surface to the temperature gradient along the surface. A pseudo-spectral Chebyshev collocation method[5] has been employed. The basic approach and the equations to be solved were outlined in the first annual report.

The objective is to study the effect of g-jitter on thermocapillary flows for a range of dynamic Bond numbers $Bd = \rho g L^2/[\partial\gamma/\partial T]$ (here the denominator represents the change in surface tension with respect to temperature). To date we have examined fluids with Prandtl numbers in the range 10^{-2} to 10, which spans the range associated with most experimental materials. Marangoni numbers in the range 1 to 10^3 have been subjected to single frequency excitations with amplitudes in the range 10^{-4}-10^{-2} g. As expected, the sensitivity of the flow to a given residual acceleration depends on the relative magnitudes of the Reynolds number and the Grashof number (see discussion in the 1st annual report and 3rd semi-annual report).

Description of the model system

The physical system currently under examination involves a 2-D rectangular region which is bounded by three rigid walls and a "free surface". Two of the rigid walls are isothermal with temperatures T_H and T_C. The other boundaries are adiabatic (no perpendicular heat flux) and the "free surface" is constrained to be a straight line. This retains the essential character of a free liquid surface while removing the numerical problems associated with a deformable one. The forces at the interface may be decomposed into components normal and tangent to it. Contributions to the force balance include the fluid pressure, the viscous forces, and the capillary forces. For the normal component of force balance, the difference between the pressure and viscous forces on either side of the interface are proportional to the interface curvature multiplied by the surface tension γ. For the tangential force balance at the interface, the difference in the shear stress components is balanced by a gradient in surface tension. Such gradients will arise when there is a temperature gradient along the interface. The gradient in temperature produces a gradient in surface tension that induces shear stresses and, thus, fluid (thermocapillary) motion. In our calculations the residual gravity vector is capable of taking any orientation with respect to the boundaries and can be time-dependent.

We approached this problem using a pseudo-spectral technique which incorporated the influence matrix method. Comparison of our results for steady flows with results obtained by Carpenter and Homsy [9] and Zebib et al. [10] indicate that our method has superior spatial accuracy over finite difference and finite volume methods. (See comparisons in tables 2 and 3.) Our g-jitter results confirm our earlier predictions that, for Ma>>1, if the free surface is not allowed to deform thermocapillary effects dominate for the range of container dimensions, acceleration magnitudes and frequencies typically associated with spacecraft experiments. The results of our work comprise the Master's thesis (Universitie D'Aix-Marseille, France) of Ms. Helene Cordier who worked at the CMMR this year. A paper intended for journal publication which describes our results is now being prepared.

5. Thermo-capillary Convection - Three Dimensional and Axisymmetric

Owing to the premature termination of the grant this work could not be completed although some progress was made during the no-cost extension. This work is described in **Appendix 3**.

6. Transport in Closed Containers

In the original proposal we agreed to make available the results of related work at the CMMR not funded through this grant. These results were included in the appendices of the 3rd semi-annual report and a summary is given in the paper in **Appendix 1**.

7. References

1. J. Sullivan, Grumman Space Station Freedom Program Support Division, Reston,

Virginia, personal communication.

2. J. L. Duranceau and R. A. Brown, "Thermal-Capillary analysis of small-scale floating zones: Steady state calculations", *J. Crystal Growth* **75** 367-389.
3. J. L. Duranceau and R. A. Brown, "Finite element analysis of melt convection and interface morphology in earthbound and Microgravity Floating Zones", in Taylor G. Wang (ed.) *Drops and Bubbles Third International Colloquium 1988*, AIP Conference Proceedings 197, American Institute of Physics, New York, 1989, pp. 133-144.
4. J. M. Floryan, "Numerical methods for viscous flows with moving boundaries," Appl. Mech. Rev. **42** (1989) 323-341.
5. R. Peyret and T. D. Taylor, *Computational Methods for Fluid Flow*, Springer Verlag, New York (1983).
6. G. Ryskin and L. G. Leal, "Numerical solution of free boundary problems in fluid mechanics. Part 1.The finite-difference technique," J. Fluid Mech. **148** (1984) 1.
7. J. Hyer, D.F. Jankowski and G.P. Neitzel, "Thermo-capillary convection in a model float zone, to be published AIAA Journal of Thermophysics and Heat Transfer, 1990.
8. I. S. Kang and L. G. Leal, "Numerical solution of axisymmetric, unsteady free-boundary problems at finite Reynolds number. I Finite difference scheme and its application to the deformation of a bubble in a uniaxial straining flow", *Physics of Fluids* **30** (1987) 1929-1940.
9. B. M. Carpenter and G. M. Homsy, "High Marangoni number convection in a square cavity: Part 2", *Physics of Fluids* **2** (A) (1990).
10. A. Zebib, G. M. Homsy and E. Meiburg, "High Marangoni number convection in a square cavity", *Physics of Fluids* **28** (1985).

Appendix 1

ORIGINAL CONTRIBUTIONS

© Hanser Publishers, Munich 1990

90A 51659

J. I. D. Alexander

Low-Gravity Experiment Sensitivity to Residual Acceleration: A Review

In this article, work related to the analysis of experiment sensitivity to residual acceleration experienced in low earth orbit spacecraft is reviewed. Most of the work discussed concerns heat, mass and momentum transfer in fluid physics and materials science experiments. On the basis of our current understanding of experiment sensitivity it is concluded that, in general, experimenters should be concerned about the effect of residual acceleration and that careful modelling included as part of an experiment program will enable optimal use of the limited experiment time available in space.

1 Introduction

It has been recognized for some time that the low-gravity acceleration environment associated with a spacecraft in low earth orbit offers an opportunity to study certain physical processes which are difficult to investigate under the gravitational acceleration experienced at the earth's surface. Our experience with such opportunities has led us to realize that the residual acceleration environment on board an orbiting spacecraft is not as low or as steady as would be desired for certain classes of experiments. The sources of the residual acceleration include [1-5] crew motions, mechanical vibrations (pumps, motors, excitations of natural frequencies of spacecraft structures), spacecraft maneuvers and basic attitude motion, atmospheric drag and the earth's gravity gradient. The accelerations are characterized by temporal variations in both magnitude and orientation. Such disturbances will, in particular, affect those experiments susceptible to buoyancy induced fluid motion [6]. Indeed, recent studies [7, 9] indicate that transient disturbances can have undesirable long term effects. The analysis of the sensitivity of any proposed flight experiment is necessary for a variety of reasons. These include the need to optimize the use of the limited time available for flight experiments, the interpretation of experimental results and the determination of tolerable acceleration levels to be used in planning for NASA's Space Station [3].

Examples of experiments that are conducted in the low-gravity environment include critical point studies [10], crystal growth [11-18], and diffusion experiments [19, 20]. Since these experiments involve density gradients in the fluid phase, they are inherently sensitive to the effects of buoyancy-driven fluid motion [21-25]. For certain types of systems it is known [7, 8, 26-37] that the associated physical processes (mass transfer, heat transfer, convection, oscillation and distortion of free surfaces) are sensitive to time-dependent accelerations. For example, the transfer of mass and heat in fluid systems can be significantly affected by oscillatory flows [28-37]. The effect of oscillation enhanced transport conditions on the local variation in composition during crystal growth is not well characterized for most of the systems relevant to crystal growth under microgravity conditions. Order of magnitude analyses [7, 8, 38] suggest that for certain combinations of physical properties and growth conditions, oscillations in the residual acceleration may adversely affect the mass transport conditions. For instance, the DMOS experiment [39] on STS 51-D showed extensive evidence of convective mixing of liquids. The degree of mixing is greater than can be attributed to the quasi-steady low-gravity component, but can be accounted for when oscillations in effective gravity are included in the description of the transport conditions.

It is possible that in future space laboratories some experiments will require isolation from vibration. The design of efficient isolation systems, however, requires determination of the tolerable acceleration levels (amplitudes and frequencies) for given experiments. The results of sensitivity analyses can be used in the development of vibration isolation systems to identify those experiments that will need isolation and by supplying data concerning frequency dependence, the effect of transients etc. The system can then be designed to filter out those bandwidths to which the experiment is predicted to respond adversely.

Low-gravity experiments which involve liquids with free surfaces are most likely to be sensitive to vibrations. Experiments of this type include studies of liquid bridges, equilibrium shapes of drops and bubbles [40-43], and thermocapillary flow experiments [43-46]. Evidence for the oscillation of liquid zone shapes was found on the D-1 mission. Long liquid bridges were more sensitive to residual gravity, and exhibited random oscillations in zone shape [40].

It should be recognized that the sensitivity of a given process to the overall low-gravity environment will depend on one or more of the following factors:

a) magnitude and direction of accelerations
b) system geometry
c) boundary conditions (e.g. insulated or conducting walls, solute sources and sinks), and
d) physical properties of the participating materials (viscosity, thermal and solute diffusivities).

Any analysis of the sensitivity to oscillatory accelerations and transient disturbances characteristic of the anticipated environment aboard Space Station, or any other spacecraft, must

---

Mail address: J. Iwan D. Alexander, Center for Microgravity and Materials Research, University of Alabama in Huntsville, Huntsville, Alabama 35899, USA.

PRECEDING PAGE BLANK NOT FILMED

take these factors into account. In general, a full mathematical characterization may not be practical. However, identification of sensitive experiments in combination with a judicious choice of simplified numerical models can be used to choose operating parameters that will optimize the use of the low-gravity environment. With this in mind, we review work related to the effects of steady and time-dependent residual accelerations, and associated work concerning transport in oscillating flows.

In sec. 2 we describe the components of the low-gravity environment. In sec. 3 previous work involving order of magnitude (OM) estimates is discussed. The application of OM analyses to acceleration-sensitivity determination is discussed in sec. 3.1. The results of simple analytical models are summarized in sec. 3.2. Work related to linear stability in the presence of modulated gravity is briefly discussed in sec. 3.3. The results of direct numerical simulations are reviewed in sec. 3.4. In sec. 4, the results and utility of residual acceleration analyses are summarized and discussed.

2 The Microgravity Environment

The low-gravity environment of a spacecraft has been referred to as a "zero gravity" environment. This is because any object within the craft is subject to roughly the same acceleration due to the earth's gravitational field. Thus, a free object may move along approximately the same orbital path as the spacecraft. As a consequence, to an observer in the spacecraft objects appear to behave as if no gravity were present. However, any body capable of motion relative to the spacecraft will experience an acceleration relative to the mass center of the spacecraft. This relative acceleration arises from several sources which include the gravity gradient of the earth, atmospheric drag and attitude motions, as well as machinery vibrations and crew activities.

The relative acceleration that is associated with the earth's gravity gradient is defined as follows. The mass center of the spacecraft is subject to a force $\boldsymbol{F}(\boldsymbol{r}_0)$ due to the gravitational attraction of the earth, where $\boldsymbol{r}_0$ is the position of the mass center of the craft with respect to the mass center of the earth. A particle at a position $\boldsymbol{r}$ within the spacecraft is subject to a force $\boldsymbol{F}(\boldsymbol{r})$. If, as a first approximation, we ignore the interaction between the spacecraft and the mass of the particle, and if the distance $|\boldsymbol{r} - \boldsymbol{r}_0|$ is small compared to the semi-major axis of the spacecraft orbit, the difference between the forces applied at $\boldsymbol{r}$ and $\boldsymbol{r}_0$ define the gravity gradient $\boldsymbol{G}$ as follows [2-6]

$$\boldsymbol{F}(\boldsymbol{r}) - \boldsymbol{F}(\boldsymbol{r}_0) = \boldsymbol{G}\boldsymbol{z}, \quad \boldsymbol{z} = \boldsymbol{r} - \boldsymbol{r}_0 . \tag{1}$$

If the spacecraft maintains a fixed orientation, for example with respect to the sun, there is no rotation of the spacecraft frame relative to the geocentric frame. In this type of orbit both the magnitude and the orientation of the residual acceleration vector change as a function of time and there will be no steady residual acceleration.

In addition to the gravity gradient acceleration the atmospheric drag force on the spacecraft can be significant [2-6], despite the fact that the atmospheric density at typical shuttle altitudes is only on the order of 10^{-12} kg m^{-3}. Atmospheric drag causes a slow inward spiral of the spacecraft. To an observer in the spacecraft the effect of atmospheric drag is to produce a relative acceleration that is equal in magnitude but opposite in sign to the atmospheric drag force. Table 1 gives atmospheric drag acceleration estimates and relative acceleration related to the gravity gradient and centrifugal force in µg per m from the mass center of a spacecraft that is in a circular orbit with a gravity gradient stabilized attitude. X_1 is parallel to the local vertical and X_2 is perpendicular to the orbital plane. For this attitude the acceleration points away from the mass center along X_1 and toward the mass center along X_2.

Table 1. Changes in residual acceleration components [µg m^{-1}] along the local vertical (X_1) and perpendicular to the oribital plane (X_2) associated with the gravity gradient stabilized attitude, and estimated atmoshperic drag accelerations. a and b are, respectively, best and worst drag estimates for the Shuttle (1) and NASA's Space Station (2). From [5]

altitude [km]	X_1	X_2	drag 1a	drag 1b	drag 2a	drag 2b
275	0.414	− 0.137	2.10	0.360	10.6	3.1
300	0.410	− 0.136	1.20	0.210	6.1	1.8
325	0.405	− 0.134	0.69	0.120	3.6	1.1
350	0.401	− 0.133	0.41	0.070	2.1	0.6
400	0.392	− 0.130	0.24	0.025	0.7	0.2
450	0.383	− 0.127	0.05	0.009	0.4	0.1
500	0.375	− 0.124	0.02	0.001	0.8	0.02

If the spacecraft does not maintain such a fixed orientation then, in addition to (1), centrifugal, Coriolis and Euler accelerations will become apparent in the spacecraft reference frame. They arise in conjuction with spacecraft attitude motions and depend on the nature of the rotation of the spacecraft frame of reference relative to a fixed geocentric frame. If a spacecraft in a quasi-circular orbit continuously rotates relative to the fixed geocentric frame such that a given direction in the spacecraft frame is always oriented parallel to the craft's position vector $\boldsymbol{r}_0$, a centrifugal acceleration will augment the gravity gradient in the direction parallel to the position vector, and cancel the component tangent to the flight path. Under these conditions there will be a steady component to the residual acceleration vector. In practice this situation arises, for example, in the so-called gravity gradient stabilized attitude.

Euler accelerations arise when the rate of rotation of the spacecraft frame changes as a function of time, as it would in a non-circular orbit, or as the semi-major axis of the orbit changes as the craft slowly spirals inward due to atmospheric drag. Coriolis accelerations will also be apparent but are proportional to the velocity of an object relative to the spacecraft. Thus, unless relative velocities are large, the Coriolis effect will be insignificant [6].

In addition to the above, there are a variety of residual acceleration components that occur over a broad range of amplitudes and frequencies. The nature and sources of these accelerations have been discussed in [1-3]. Figs. 1 and 2 are examples of residual accelerations measured on orbit.

3 Analyses of Residual Acceleration Effects

As discussed in the introduction, many experiments are undertaken in orbiting spacecraft in order to reduce or eliminate unwanted effects of buoyancy driven motions in fluids. Sources of buoyancy in fluids include discrete interfaces, as they occur, for example between immiscible fluids, solid par-

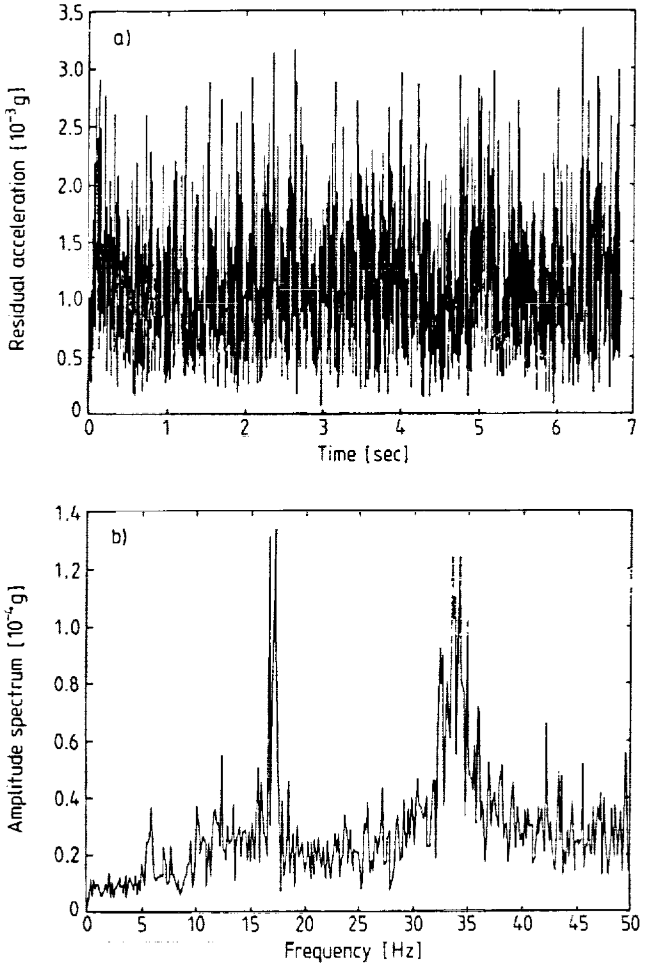

Fig. 1. An example of a relatively "quiet period" measured on SL-3 ($< 4 \cdot 10^{-3}$ g, g = 9.8 m s^{-2})
a) Total acceleration array, b) Combined amplitude spectrum, note components in the 5-6 Hz and 7-8 Hz, 10-12 Hz, 17 Hz and 30-35 Hz ranges. After Rogers and Alexander [47]

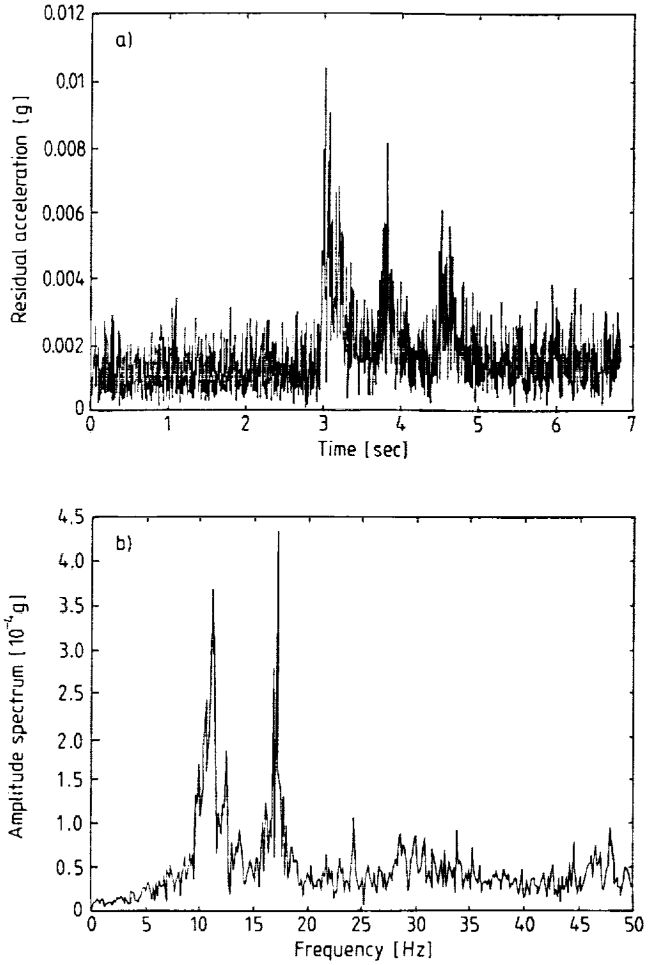

Fig. 2. "Window" containing three thruster pulses
a) Total acceleration array, maximum magnitude $\sim 1 \cdot 10^{-2}$ g, b) Combined amplitude spectrum, dominant frequency components 11 Hz and 17 Hz. After Rogers and Alexander [47]

ticles and fluids, and bubbles and fluids with different densities, other buoyancy sources are internal density gradients that arise as a consequence of gradients in temperature and concentration. The nature of the response of a bulk fluid to the effective body force associated with a low-gravity environment will depend, in part, on the relative orientation of the residual acceleration vector and the density gradient. In particular, if the integral of the effective body force $\varrho \boldsymbol{b}$ (where ϱ is the density and $\boldsymbol{b}$ the effective acceleration) acting on any closed circuit within the fluid is non-zero, motion will immediately ensue. That is, if

$$\int_C \mathrm{d}\boldsymbol{c} \cdot \varrho \boldsymbol{b} = \int_S \mathrm{d}\boldsymbol{A} \cdot \operatorname{curl} \varrho \boldsymbol{b}$$

$$= \int_S \mathrm{d}\boldsymbol{A} \cdot [\operatorname{grad} \varrho \times \boldsymbol{b} + \varrho \operatorname{curl} \boldsymbol{b}] \neq 0 , \qquad (2)$$

motion will occur. Note also, that even if there is no density gradient motion will occur if

$$\int_S \mathrm{d}\boldsymbol{A} \cdot \operatorname{curl} \varrho \boldsymbol{b} \neq 0 . \qquad (3)$$

This includes the case of "precessional stirring" [48]. This could occur, for example, when a spacecraft orbiting in a radial attitude (i.e. it continuously rotates about an axis perpendicular to the orbital plane) underwent an additional rotation about some axis other than the basic orbital axis.

There have been three approaches to the determination experiment sensitivity to the residual acceleration environment.

a) order of magnitude analyses [38, 49-52],
b) analytical models [5, 6, 39, 53-59], and
c) direct numerical simulation [9, 3, 60-73].

In addition to work directly related to microgravity, there is extensive literature on mass and heat transport in oscillatory flows [26-36], the effect of gravity modulation on the classical Bénard problem [74-77] and the linear stability of planar fluid surfaces [78, 79].

3.1 Order of Magnitude Analyses

An order of magnitude (OM) or dimensional analysis of a physical process involves the examination of the system of equations that are assumed to govern the process. For fluid physics and material science experiments, the relevant physical processes are governed by equations describing the transport of heat, mass and momentum in single and multi-component fluid systems. The usual approach to OM analyses [51] involves the definition of reference quantities which appropriately characterize the physical system (i.e. reference scales for velocity, time, length, forces, etc.). Application of these scales to the (dimensional) governing equations, followed by the definition of characteristic dimensionless groups admits a comparison of the order of magnitude of every term in each equation. There are several comprehensive discussions of OM analyses applied to low-gravity situations (e.g. [38, 49-51]).

The advantage of the OM approach is that a great deal of information pertaining to the sensitivity of a given experiment can be obtained with little computational effort. The disadvantages are related to the fact that the choice of characteristic reference quantities for length, velocity, time etc. are not, in general, known a priori [80]. Thus, in cases for which the chosen characteristic scale is not (for a given set of conditions) representative of the actual process, the results of the analysis may be in error, often by several orders of magnitude. In addition, application of OM analyses to the problem of g-sensitivity has invariably involved implicit linearization and often poorly represents the multi-dimensional nature of the physical process. This can also lead to incorrect OM predictions. Finally, analyses are generally restricted to the examination of a single component disturbance (e.g. $\sim \sin(\omega t)$). As a result, they may not properly indicate the response of the system to the typically complex multi-frequency disturbances characteristic of the spacecraft environment. It is nonetheless useful to examine the general trends predicted by such analyses since they can provide at least qualitative guidance for more detailed analytical and numerical studies.

The determination of tolerable g-levels using OM analyses is based upon estimations of the response of a system to either steady accelerations or time-dependent disturbances of the form

$$g(t) = a\cos(\omega t), \tag{4}$$

where ω is the angular frequency of the disturbance. The susceptibility of an experimental system to such disturbances is defined via the magnitude of a particular response (say a temperature, compositional or velocity fluctuation) which must not be exceeded in order to bring the experiment to a successful conclusion. The most obvious trend predicted by analyses to date is shown in figs. 3-5. The curves depict the maximum tolerable residual acceleration magnitude as a function of frequency, $f = \omega/2\pi$, for given experiments and have the form

$$g_{max} = F(\omega, \Pi_{crit}, p_i), \tag{5}$$

where Π_{crit} is the magnitude of the maximum allowable response, and the p_i, $i = 1, N$ represent the N material properties of the system (such as viscosity, thermal and species diffusivities). In general, below 10^{-2} to 10^{-3} Hz the response is expected to be either independent or weakly dependent on frequency. At higher frequencies the analyses indicate that the allowable residual acceleration magnitude increases as approximately the square of the frequency. This behavior can

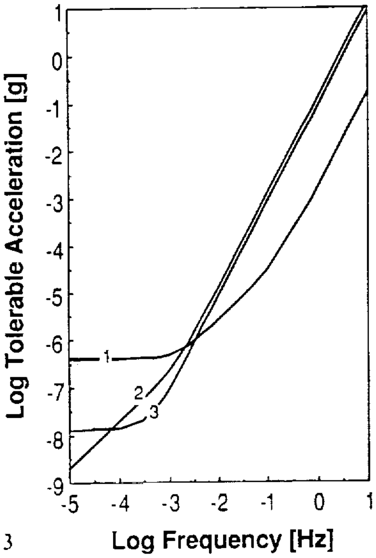

3

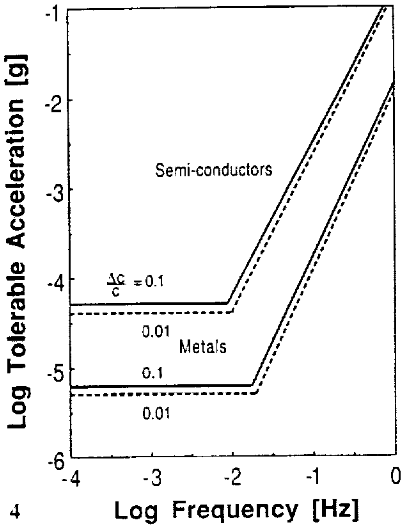

4

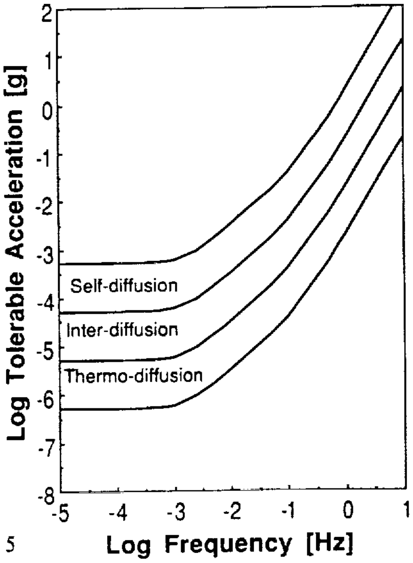

5

Fig. 3. Estimated tolerable residual accelerations (in units of $g = 9.8\ m\ s^{-2}$) as a function of frequency for: 1) a fluid physics experiment involving a temperature gradient, 2) a crystal growth experiment and 3) a thermodiffusion experiment. After Monti et al. [38]

Fig. 4. Estimated tolerable residual accelerations (in units of $g = 9.8\ m\ s^{-2}$) for semiconductor and metal solidification experiments. The sensitivity parameter is longitudinal segregation, $\Delta c/c$. $Pe_s = 5$, temperature gradient $= 50\ K\ cm^{-1}$, $k = 0.1$. After Monti et al. [36]

Fig. 5. Estimated tolerable residual acceleration (in units of $g = 9.8\ m\ s^{-2}$) ranges for diffusion experiments. After Monti et al. [36]

be understood upon consideration of the following OM estimates [38] (used to obtain fig. 3) for velocity, temperature and concentration changes associated with the acceleration (4):

$$V_g \sim \frac{g^* \Delta\varrho/\varrho}{(\omega^2 + \nu^2/L^4)^{1/2}} \tag{6}$$

$$\delta T \sim V_g \frac{\Delta T/L}{(\omega^2 + \kappa^2/L^4)^{1/2}}\,, \tag{7}$$

$$\delta C \sim V_g \frac{\Delta C/L}{(\omega^2 + D^2/L^4)^{1/2}}\,, \tag{8}$$

where g^* is the residual acceleration magnitude,
ϱ is the mass density,
and $\Delta\varrho/\varrho$ is the change in density due to temperature and/or composition;
$\Delta T/L$, $\Delta C/L$ and L are, respectively, a characteristic temperature gradient, concentration gradient and length;
κ is the thermal diffusivity.

The sensitivity limits are obtained by using either δT, δC or V_g as a sensitivity parameter and setting g^* equal to the allowable residual acceleration g_{max}.

For situations which involve mixed thermocapillary convection and buoyancy-driven convection the governing dimensionless groups are [51]:
the Bond number, $Bo = \varrho g^* L^2/\gamma$,
the Grashof number $Gr = \Delta T |\beta_T| g^* L^3/\nu^2$,
the Prandtl number $Pr = \nu/\kappa$,
and the Surface Reynolds number $Rs = |\gamma_T| \Delta T L/\mu\nu$.
Here $|\gamma_T|$ is the rate of change of surface tension γ with temperature,
β_T is the coefficient of thermal expansion,
ν is the kinematic viscosity,
μ is the shear viscosity.

These groups respectively represent the ratios of buoyancy force to surface force, buoyancy force to inertial force, thermal and momentum timescales, and surface force to inertial force.

The relative importance of gravity and thermocapillary forces can then be estimated upon considering the relative magnitudes of the velocity due to buoyancy and the velocity due to thermocapillary effects [50, 51]. The latter is given by

$$V^* = \frac{|\gamma_T|\,\Delta T}{\mu}\,. \tag{9}$$

For thermocapillary flow to dominate, the ratio of V_g to V^* must be less than one. For this to occur, the maximum magnitude of the acceleration must satisfy:

$$g^* < |\gamma_T| \frac{(\omega^2 + \nu^2/L^4)^{1/2}}{\nu\,\beta_T}\,. \tag{10}$$

Eq. (10) can be re-interpreted in terms of the ratio of the Grashof number, Gr, and the surface Reynolds number, Rs. The condition for buoyancy and thermocapillary forces to be the same magnitude is

$$Gr = Rs\,(St^2 + 1)^{1/2}\,, \tag{11}$$

where $St = \omega L^2/\nu$ is the Strouhal number.

This condition is illustrated in fig. 6. Three regimes of interest are identified. These regions are defined by the relative values of the Grashof, Strouhal and surface Reynolds numbers. In region I, the Strouhal number, St, is less than one, and the condition that thermocapillary forces dominate is equivalent to that for a steady flow. In region II, St is greater than one. In this region, for a fixed value of Rs, the value of Gr required to give buoyancy forces equal weight to thermocapillary forces increases with increasing values of the Strouhal number. This essentially reflects the fact that the characteristic time for the fluid response greatly exceeds the period of the disturbance. Thus, thermocapillary forces dominate at higher values than in region I. In region III buoyancy forces predominate over thermocapillary forces. For situations here a boundary layer scaling is appropriate i.e. $Rs \gg 1$ [50]. The relative importance of buoyancy can be estimated via the ratio

$$Gr = Rs^{5/3}(St^2 + 1)^{1/2}\,. \tag{12}$$

Fig. 7 depicts the relationship between the estimated tolerable g-level and the frequency of the acceleration for experi-

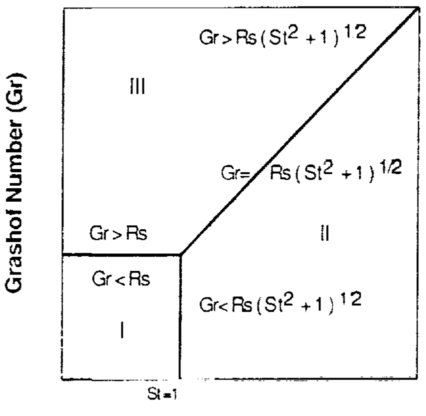

6

Fig. 6. Tolerable acceleration limits for a thermocapillary flow experiment expressed in terms of Grashof (Gr), Strouhal (St) and Surface Reynolds (Rs) numbers

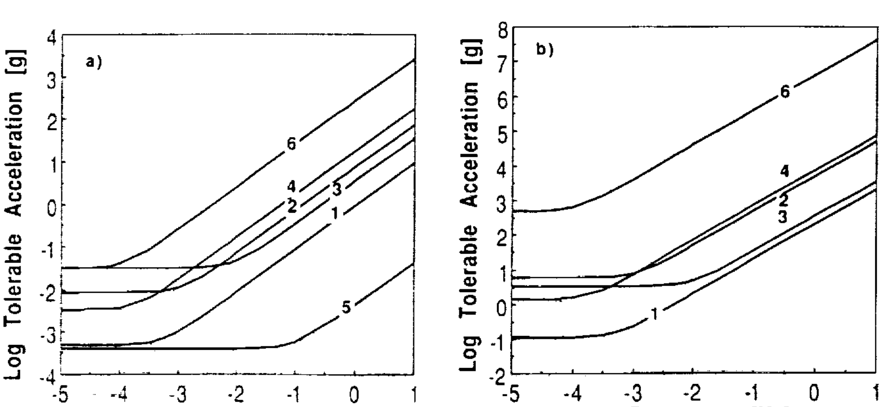

7

Fig. 7. Tolerable acceleration limits (in units of g = 9.8 m s^{-2}) as a function of frequency for the thermo-capillary experiments with properties listed in table 2. a) Gravity forces 1% of thermo-capillary forces, b) gravity forces 10% of thermo-capillary forces

e 2. Physical properties and dimensionless groups for various experimental systems: 1-di-methyl silicone oil [44], 2-methanol [81], 3-$NaNO_3$ [45], 4-indium 5-selenium - [82], 6-silicon [15]

eri- t	$\mu\, g$ [cm s^{-2}]	ν [cm^2 s^{-1}]	κ [cm^2 s^{-1}]	$\lvert\gamma_T\rvert$ [dyne cm^{-1} K^{-1}]	ΔT[K]	β_T [K^{-1}]	L [cm]	$Gr = \frac{\beta_T\, \Delta T H^3 g}{\nu^2}$	$Rs = \frac{\lvert\gamma_T\rvert\, \Delta T L}{\mu\nu}$	Gr/Rs	$GrRs^{-5/3}$	Pr
	$4.56\cdot10^{-2}$	$5.01\cdot10^{-2}$	$8.7\cdot10^{-4}$	$6.55\cdot10^{-2}$	32	$1.05\cdot10^{-3}$	3.8	$7.1985\cdot10^{5}\ g/g_0$	$3.486\cdot10^{3}$	206.5 g/g_0	0.898 g/g_0	57.6
	$5.8\cdot10^{-3}$	$7.4\cdot10^{-3}$	$1.08\cdot10^{-3}$	$7.7\cdot10^{-2}$	10	$1.2\cdot10^{-3}$	1	$2.1476\cdot10^{5}\ g/g_0$	$1.801\cdot10^{4}$	11.9 g/g_0	$1.736\cdot10^{-2}\ g/g_0$	6.85
	$2.82\cdot10^{-2}$	$1.48\cdot10^{-2}$	$1.67\cdot10^{-3}$	$5.5\cdot10^{-2}$	15	$3.8\cdot10^{-4}$	0.5	3188 g/g_0	1024	3.11 g/g_0	$3.06\cdot10^{-2}\ g/g_0$	8.86
	$1.94\cdot10^{-2}$	$2.76\cdot10^{-3}$	$2.17\cdot10^{-1}$	$6.2\cdot10^{-2}$	5	$1.21\cdot10^{-4}$	1.5	$2.6269\cdot10^{5}\ g/g_0$	8684	30.2 g/g_0	$7.16\cdot10^{-2}\ g/g_0$	$1.27\cdot10^{-2}$
	5.3	1.33	$4.0\cdot10^{-4}$	$7.7\cdot10^{-2}$	5	$2.23\cdot10^{-3}$	1.5	20.8 g/g_0	$8.19\cdot10^{-2}$	254 g/g_0	–	595
	$7.5\cdot10^{-3}$	$3.0\cdot10^{-3}$	$1.3\cdot10^{-1}$	$4.3\cdot10^{-1}$	50	$1.43\cdot10^{-4}$	2	$6.228\cdot10^{6}\ g/g_0$	$1.911\cdot10^{6}$	3.23 g/g_0	$2.12\cdot10^{-4}\ g/g_0$	$2.3\cdot10^{-2}$

ments with the physical properties given in table 2. These figures represent estimates based on two extreme flow regimes, penetrative or "viscous" flow (fig. 7a) and boundary layer flow (fig. 7b) and may be respectively considered as "worst" and "best" case estimates for the given sensitivity parameters. The curves have been determined for a sensitivity criterion which requires the tolerable acceleration levels to be such that the buoyancy forces should not exceed 10% of the thermocapillary forces (if the requirement had been 1%, the tolerable accelerations would be an order of magnitude smaller). In terms of acceleration levels predicted for the space station or measured on past missions the practical sensitive ranges are restricted to disturbances with frequencies less than 10 Hz. The majority of the estimates suggest that for these experimental parameters, periodic vibrations will generally not lead to significant buoyancy effects.

The above examples estimate the effects of simple single component accelerations. In reality, low-gravity disturbances tend to be associated with more than one frequency. Given that a system may respond to a multi-frequency disturbance in an "additive" way, tolerance curves such as these may underestimate the response to a given low-gravity disturbance. For example, models of the DMOS experiment, show that mass transport has an additive response to the (multi-frequency) residual acceleration [39]. Post flight analysis of the experiment results has demonstrated that the amount of mixing observed between organic liquids can be explained by the additive response of the system to a multicomponent disturbance.

In many cases an a priori choice of length or time scales may not be obvious. For example, in a study of dopant (solute) uniformity in directionally solidified crystals, the OM estimates of *Rouzaud* et al. [52] and *Camel* and *Favier* [83] are in agreement with the direct numerical simulations of *Chang* and *Brown* [84] for a Schmidt number (ratio of the melt's kinematic viscosity to dopant diffusivity) of 50 but overestimate the amount of radial segregation for a Schmidt number of 10.

The results of an order of magnitude or scaling analysis have been compared in [80] with those of numerical simulations of the effects of steady residual acceleration on compositional non-uniformity in directionally solidified crystals. The basic model consisted of a Bridgman-type system with an ampoule translated between hot and cold zones spearated by a thermal barrier. In order to apply the Camel-Favier technique [52, 83] to the numerical simulation, it was necessary to evaluate a proportionality constant, x_0^2. This relates the maximum convective velocity obtained in the numerical simulations with the Grashof number. The value of this constant depended on the orientation of the acceleration, and on the chosen length scale. The adiabatic zone length L_a yielded results which best showed the trends predicted by the Camel-Favier approach. Table 3 lists values of x_0 associated with different choices of L_a as a reference length. Having calculated x_0 we then determined the transport regime (see refs. [52, 80, 83] for details) by graphing, in fig. 8, $GrSc$ vs Pe_g for the case of the residual acceleration parallel to the interface. Here Sc (Schmidt number) gives the ratio of kinematic viscosity to thermal diffusivity, and $Pe_g = VL/D$, is a ratio of the translation rate to the characteristic diffusive speed where L is the characteristic diffusion length and D the solute diffusivity. The lateral composition non-uniformities in the crystal obtained from numerical simulations [9] are also given in fig. 8. A comparison between computed and predicted non-uniformity values showed that at high values of $GrSc$ (region Ic in fig. 8), the order of magnitude approach meets with some success but is less faithful at low values of $GrSc$ (for example the transition between regions Ib and II). Fig. 8 also contains two cases for which Pe_g is reduced at fixed $GrSc$. According to the estimates the lower $GrSc$ case should have yielded a higher compositional non-uniformity as the growth rate was reduced, i.e. the estimates predict that the system

Table 3. Comparison of numerical (ξ^*_m) and order of magnitude estimates ($_m$) of compositional non-uniformity for different choices of length scale [80]. The non uniformity x in these cases is given by $\xi = \lvert c(0) - c_\infty \rvert / c(0)$. c_∞ is the melt composition far from the crystal and, because $k < 1$, $c(0)$ is the maximum value of the composition at the interface

g-orientation	L [cm]	x_0	Gr	Sc	ξ^*_m[%]	ξ_m [%]	Pe_g	regime
parallel	1.0	0.066	145	10	61	10	5	II (b)
parallel	0.25	0.27	2.27	10	61	73	1.25	I (b)
parallel	1.0	0.066	145	15	71	5	7.5	II (b)
parallel	0.25	0.27	2.27	15	71	40	1.875	II (b)
parallel	1.0	0.066	145	25	73	2.5	12.5	II (b)
parallel	0.25	0.27	2.27	25	73	21	3.125	II (b)
parallel	1.0	0.066	145	10	12	18	0.5	I (b)
parallel	0.25	0.27	2.27	10	12	8	0.125	I (b)

ORIGINAL PAGE IS
OF POOR QUALITY

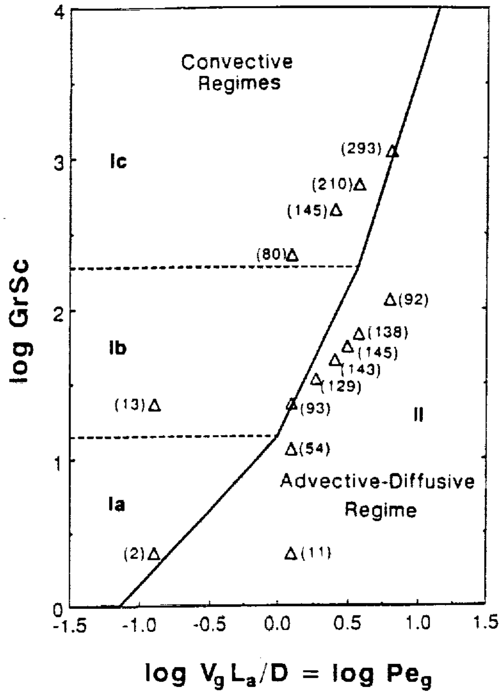

Fig. 8. A plot of GrSc vs. Pe_g for the results of numerical simulations for steady accelerations parallel to the crystal-melt interface [80]. The solid and dashed lines delineate the following transport regimes: I a–c convective regime; II advective-diffusive regime [83]. Note that the adiabatic zone length has been used to calculate the Grashof and growth Peclet numbers, and that $x_0 = 0.27$. Numbers in parentheses indicate the value of compositional non-uniformity $\xi = |c_{smax} - c_{smin}|/c_{sav} \cdot 100\%$, wehre c_s denotes the crystal composition at the melt-crystal interface, associated with each of the numerical results

moves closer to the convective diffusive transition. This was not reflected in the non-uniformity obtained from the numerical simulations. Evaluation of the numerical results showed that the increase in the characteristic diffusion length scale (associated with reduction in growth rate) led to an order of magnitude decrease in the solute gradient at the interface. Hence, because the system-wide variation in composition is small, the interfacial non-uniformity is correspondingly small.

The above results indicate that scaling arguments alone can at best be expected to yield order of magnitude accuracy. The limitations of scaling arguments are hardly surprising if one considers the neglect of the multi-dimensionality (boundary conditions, flow structure, etc.) of the physical situation which is inherent in such scalar descriptions. Of course, prior knowledge of the system behavior can be used to locally improve the accuracy of the scaling, (e.g. *Kimura* and *Bejan* [85]). Similarly, if a system locally exhibits one-dimensional behavior, such as boundary layer flow, then the appropriate scaling for the formal reduction of the transport equations can be used effectively to estimate the local system response. In general, however, our understanding of the response of systems to residual acceleration can be furthered only by an approach which uses scaling, mathematical modelling and, naturally, the results of experiments in a complementary fashion.

3.2 Analytical Models

A few attempts have been made to assess the effects of time-dependent residual acceleration using analytical models [53–59]. The first attempt to model the effects of disturbances on heat transfer between a fluid and a solid bounding medium was carried out by *Gebhard* [53]. Under the assumption that the fluid and its container would be subject to a "sequence of abrupt relative displacements spaced by a time interval τ_c ...", *Gebhard* took τ_c to be a random distributed variable. He showed that as τ_m (the most likely value of τ_c) decreases, the resulting heat transfer was greater than predicted by conduction in the absence of a disturbance. In particular, it was found that for $\tau_m < d^2/\kappa$ (where d is a characteristic length and κ is the thermal diffusivity) the heat transfer increased rapidly as τ_m decreased. The main limitation of this model is that fluid convection (and thus fluid properties such as kinematic viscosity) do not enter the analysis. It is well known that the response of heat transfer to convection varies according to the Prandtl number. In particular, for low-gravity flows (as we shall see later) the temperature field is less sensitive to convection for low Prandtl number fluids ($Pr < 1$).

Approximate solutions for transient convection in a cylinder with an azimuthal temperature variation have been obtained by *Dressler* [54]. Residual accelerations representing the motion of an astronaut and a transient rotation of the spacecraft were imposed on the system. Linear accelerations were imposed perpendicular to the cylinder axis. For kinematic viscosities of 10^{-2} cm^2 s^{-1}, cylinders of radius 1 and 2 cm with a maximum temperature difference of 95 K across the diameter were examined. The maximum fluid velocities consequent to the astronaut motion (modelled by a sequence of two step functions separated by 2 s with $4 \cdot 10^{-4}$ g magni-

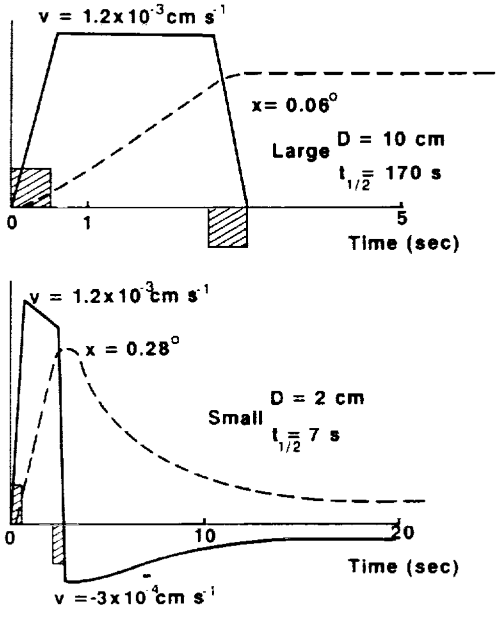

Fig. 9. Transient convection in large and small test cells due to residual accelerations caused by astronaut motion after Dressler [54]. Here x is the angular displacement, v the velocity and $t_{1/2}$ is the decay time given by $0.68 \cdot R^2/v$

tude, 0.5 s duration and zero mean, oriented perpendicular to the temperature gradient) were 12 μm s^{-1} for both the large and small diameter cylinders (see fig. 9). For the larger cylinder the second pulse reduced the velocity from 12 μm s^{-1} to 0 by the end of the pulse. The effect of the second pulse was to change the velocity in the small container from 12 to −3 μm s^{-1} by the end of the pulse. The velocity decayed asymptotically to zero reaching a value close to zero after 15 s. The reason the response was different for the two containers can be explained simply in terms of the momentum decay times ($t_{1/2} \sim R^2/\nu$) for each container. The velocity in the larger container had hardly begun to decay when the second impulse arrived. The shorter decay time associated with the smaller container meant that the impulse acted on a smaller magnitude velocity which explains the change in direction of the motion. While the disturbance had a mean value of zero the fluid particles attained a finite displacement (indicated by the value x of the angular displacement in fig. 6). Similarly, a disturbance corresponding to a simple spacecraft maneuver was examined. The simulated maneuver corresponded to a 90° rotation of the spacecraft at a rate of 1° s^{-1}. The maximum velocities associated with the centrifugal acceleration were, respectively, 40 and 35 μm s^{-1} for the large and small diameter cylinders.

Experiments involving free surfaces of liquids have a high probability of responding to residual accelerations. Indeed, unexpected results have been attributed to residual accelerations in several cases [40, 86-88]. Particular examples of such experiments involve liquid (float) zones. Three types of liquid zones are typically the subject of low-gravity experiments [89]: isothermal and non-isothermal zones suspended between inert solids (i.e. liquid bridges), and non-isothermal zones suspended between a feed rod and a growing crystal. The dimensionless group associated with the shape of isothermal static liquid zones is the Bond number, *Bo*, defined earlier. It expresses the relative importance of gravitational and surface forces. A comprehensive description of stable zone shapes in zero gravity, and as a function of *Bo*, is given by *Martinez* et al. [41]. Fig. 10 displays their results for the stability of static zones with a steady acceleration parallel to the zone axis. In order to relate the Bond number to a given acceleration level they give the value of $Bo = 1.4$ for a 1 l volume of water subject to an acceleration of 1 cm s^{-2}. For $Bo = 0$, the zone volume $V = V^* = \pi R^2 L$ and contact angle $a = 90°$ the maximum stable length is $2\pi R$ (the Rayleigh limit). *Coriell* et al. [90] investigated the effect of *Bo* on the maximum length of such zones and compared theoretical predictions with experimental results (see fig. 11). The actual length of the equilibrium zone is determined by the volume, the contact angle a and the static Bond number.

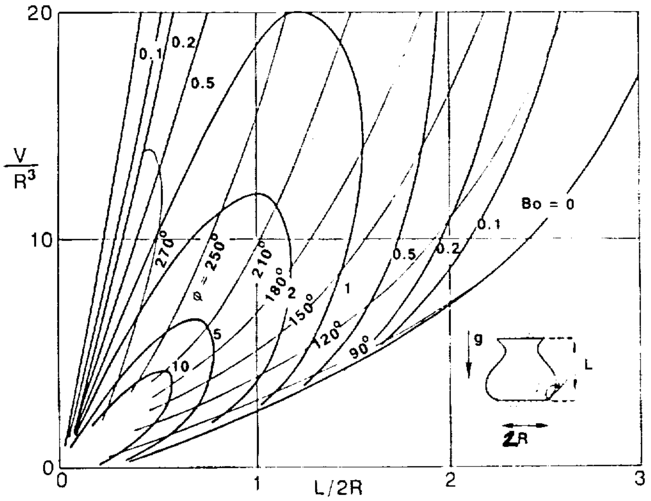

Fig. 10. Stability limits of an isothermal liquid bridge of volume V and length L suspended between discs of radius R and subject to a steady axial acceleration defined by a Bond number Bo, after Martinez et al. [41]. The angle Φ is defined in the inset

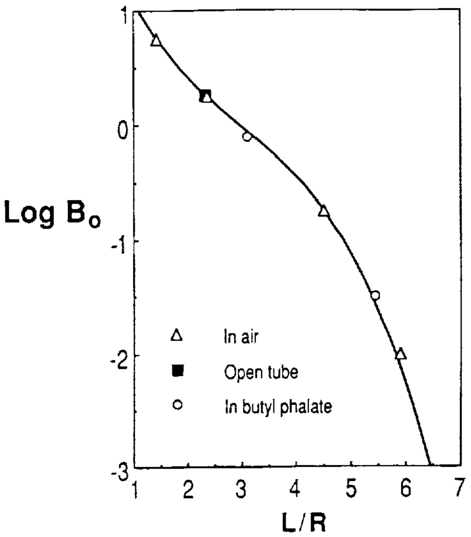

Fig. 11. The maximum stable zone length of an isothermal liquid zone suspended between inert solids of radius R as a function of Bond number: Comparison of theory and experiment. After Coriell et al. [90]

Estimates of the effect on the free surface shape of oscillatory residual acceleration parallel to the axis of an isothermal liquid bridge have been made by *Langbein* [55]. Not suprisingly, his calculations suggest that the sensitivity of the surface is highest for disturbances with frequencies close to the natural frequency of the bridge, typically in the 0.001-10 Hz range. For the example given in [55], the maximum acceleration magnitudes that can be tolerated by a bridge less than 90% of the maximum stable bridge length (given by the Rayleigh limit) range from $5 \cdot 10^{-8}$ to $5 \cdot 10^{-3}$ g. The criterion used to determine the tolerable residual acceleration was that the amplitudes of all surface shape excitations with frequencies other than the resonance frequency be kept to 0.1% of the radius of the column. Examples of the results of this analysis are shown in fig. 12. The curves represent the maximum tolerable axial acceleration for a given aspect ratio (fig. 12a), and for a surface response with a given number of nodes (fig. 12b). The results express the maximum tolerable frequency a_0 in terms of the g-jitter frequency ω, the resonant frequency, ω_m, of the liquid zone associated with the m^{th} node of the deformation of the zone surface, the viscosity of the liquid ν and the spatial wavenumber

$$a_0 < \min\left[\sqrt{\omega^2 - \omega_m^2)} - \omega\,\nu\,q_m\right], \tag{9}$$

where $\omega_m^2 = \gamma\, q_m^2 [(q_m R)^2 - 1]/\varrho R$, and
$q_m = (m+1)\,\pi/H$.

ORIGINAL PAGE IS
OF POOR QUALITY

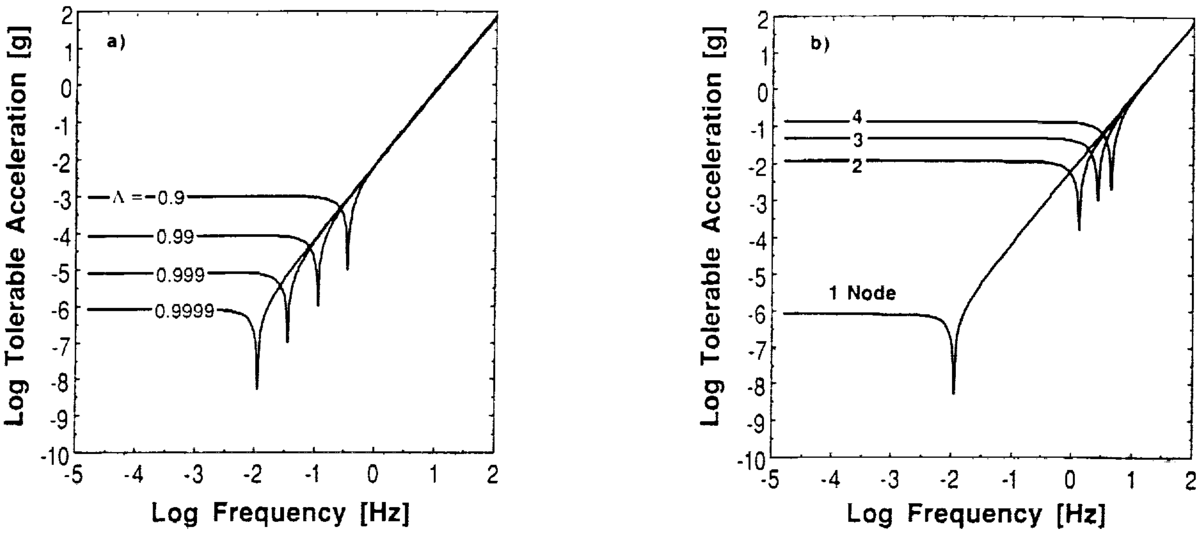

Fig. 12. Tolerable residual accleration (in units of g = 9.8 m s^{-2}) for experiments investigating resonance frequencies of liquid columns subject to axial acceleration, following Langbein [55]
a) Sensitivity for different aspect ratios $\Lambda = L/2\pi R$, b) Change in sensitivity with number of nodes in the deformation for $\Lambda = 0.9999$

R is the column radius, and
H the column height.

Note that the global minimum, and local minima of the tolerable acceleration curve occur at disturbance frequencies equal to the natural frequencies of the system.

Zhang and *Alexander* [91] have also analyzed this problem using a slender-body approximation. The problem of determining the axisymmetric response of the shape of the free surface of a cylindrical liquid column bounded by two solid regions is modelled by a 1-D system of non-linear equations. It is found that the sensitivity of the zone to breakage and shape changes depends on the static Bond number, aspect ratio and viscosity as well as the amplitude and frequency of the disturbance. The general trend is an increase in tolerable residual acceleration with increasing frequency. At the eigenfrequencies of the zone, however, there are strong deviations from this trend. At these frequencies this model also shows that the tolerable residual gravity level can be two orders of magnitude lower. These most sensitive frequencies have been found in the $10^{-2}-10^{-1}$ Hz range (see for example fig. 13). For the cases examined, maximum tolerable residual gravity levels as low as 10^{-6} *g* have been calculated. For higher viscosities the tolerable acceleration level is increased for all frequencies. The equilibrium shape, as determined by the steady background acceleration, has a prounounced effect on the response at low frequencies. A change in slenderness of the bridge markedly changes the sensitivity to residual acceleration as the Rayleigh limit is approached. It is clear that for liquid bridges, small magnitude accelerations cannot be ignored.

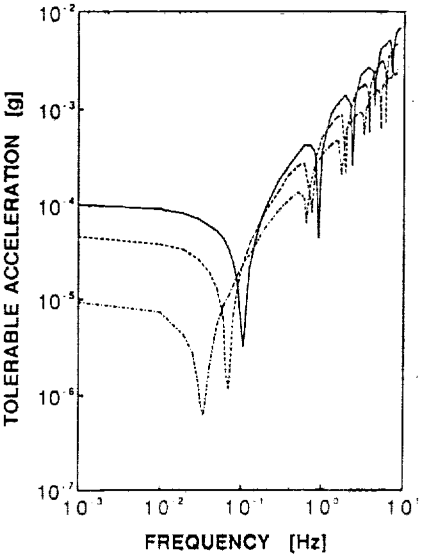

Fig. 13. Curves of tolerable acceleration (in units of g = 9.8 m s^{-2}) vs. frequency for a maximum liquid bridge shape change of 10% at Bo = 0.002, g_o = $1.42 \cdot 10^{-5}$ g and C = 0.001. The solid curve, the dotted curve, and the dotted-dashed curve are the results for aspect ratios L/2 R = 2.6, 2.826, and 3.024, respectively. From Zhang and Alexander [92]

For non-isothermal zones, the dimensionless groups introduced earlier in sec. 3.1 govern the problem. For molten silicon *Sekerka* and *Coriell* [89] have calculated the values of these groups. They are presented in table 4. The relative magnitudes of the terms suggest that on earth the zone shape will be dominated by the capillary effect (large *Bo*) for typical zone sizes, while under low-gravity conditions the zone shape will be influenced mainly by the temperature gradient along the interface. In addition (as discussed earlier) dynamic distortions may also be important. Considerations of the float zone crystal growth process introduce further complications which ultimately require independent analysis. In the previous cases, the surfaces of the inert solids between which the zone is suspended are usually planar. This is generally not the case for the crystal growth process. The actual shape depends primarily on the thermal conditions. The influence of the meniscus angle at either of the crystal-melt-vapor trijunctions can also be important and has been analyzed by *Heywang* [93] and *Coriell* et al. [94]. In addition to zone fail-

Table 4. Values of dimensionless groups for silicon calculated from the data of Chang and Wilcox [92]. The length scale is taken to be the zone radius R; β_l is estimated at $1.6 \cdot 10^{-4}\ K^{-1}$. For space, g_s is taken as $10^{-4}\ g$. ΔT is assumed to be $10\ ^\circ C$ (after Sekerka and Coriell [89])

Bo	*Bo*	*Gr*	$N_3 = \frac{\varrho \nu^2}{R\gamma}$	$Rs\, N_3 = \frac{\Delta T \lvert \gamma_T \rvert}{\gamma}$	*Pr*	*Rs*
earth						
$R = 1$ cm	3.4	$1.3 \cdot 10^5$	$4.3 \cdot 10^{-8}$	$6 \cdot 10^{-3}$	$2.3 \cdot 10^{-2}$	$1.4 \cdot 10^5$
$R = 10^{-2}$ cm	$3.4 \cdot 10^{-4}$	$1.3 \cdot 10^{-1}$	$4.3 \cdot 10^{-10}$	$6 \cdot 10^{-3}$	$2.3 \cdot 10^{-2}$	$1.4 \cdot 10^3$
space						
$R = 1$ cm	$3.4 \cdot 10^{-4}$	$1.3 \cdot 10$	$4.3 \cdot 10^{-8}$	$6 \cdot 10^{-3}$	$2.3 \cdot 10^{-2}$	$1.4 \cdot 10^5$

ure due to the classical capillary instability (or Rayleigh instability), a "dewetting" instability is found to be important. The instability arises when the angle between the meniscus and the melt-crystal interface is less than the wetting angle for the liquid melt on the solid crystal. For Si zones of greater than 1 cm radius, zone failure on earth occurs due to the Heywang instability [94, 95]. Zone failure by this mechanism is unlikely under low-gravity conditions.

Feuerbacher et al. [56] developed an ad hoc model to describe experiment sensitivity to residual accelerations. The model is based on the motion of a body in response to an applied sinusoidal oscillation. The governing equation is that of a damped harmonic oscillator. The tolerable residual acceleration are (as expected) found to increase with increasing frequency of the disturbance. Furthermore, there is a minimum tolerable acceleration at disturbance frequencies corresponding to the natural frequency of the system.

The effect of time dependent accelerations on experiments involving drops and bubbles has been examined for the cases of sinusoidal and Heaviside-function disturbances [57]. The criterion used to define the sensitivity is that the displacement of the drop not exceed 10% of the drop radius. For a given set of physical properties, the admissible accelerations can be expressed as a function of frequency (fig. 14). The tolerable acceleration levels exhibit trends similar to those depicted in figs. 4-6.

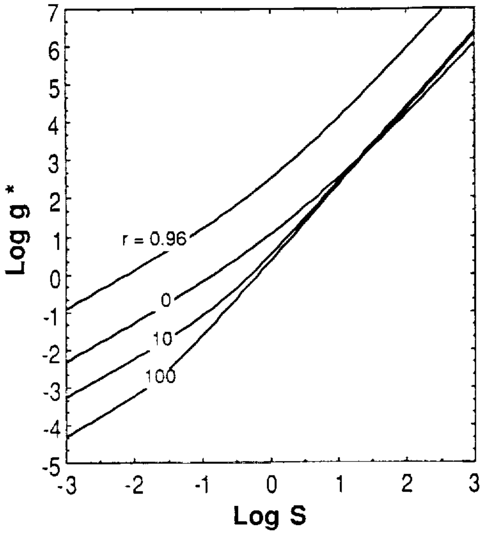

Fig. 14. Threshold intensity $g^* = g_r R^4/\nu^2 d_r$ as a function of normalized frequency $S = \omega R^2/2\nu$ after Dewandre [57]. Here g_r is the maximum tolerable acceleration, d_r the admissible displacement and r is the ratio of the drop density to that of the surrounding fluid

The influence of the gravity gradient, atmospheric drag and spacecraft attitude motion on the motion of a spherical solid particle immersed in viscous fluid has also been considered [5, 6]. The extent and nature of the influence of the gravity gradient and the atmospheric drag on the trajectory of the particle are, for a given value of the Stokes drag coefficient, shown to be dependent on the characteristic orbital attitude, the magnitude of the atmospheric drag accelerations and the distance of the particle from the mass center of the spacecraft.

Amin [59] has investigated the influence of g-jitter on heat transfer from an isothermal sphere maintained at a constant temperature greater than the ambient fluid temperature. The body force was taken to have a single frequency sinusoidal time dependence and a small amplitude. A significant result of the analysis is that the Reynolds stresses associated with the fluctuating flow result in a steady streaming motion. This has implications for both heat and mass transport in oscillating flows. For the low *Pr* fluids examined, it was concluded that buoyancy induced convection caused by high frequency g-jitter (with amplitudes $10^{-2}\ g$) will result in heat transfer conditions significantly different from pure conduction. However, it was found that in high Prandtl number fluids with small kinematic viscosities, low frequency g-jitter will influence on heat transfer.

Analyses of heat transfer in (laminar) oscillating flows in cylinders and between parallel plates [27-33] have shown that at high frequencies the effective thermal diffusivity is proportional to

$$\kappa_{eff} \sim \frac{\omega\, \Delta x^2}{Wo}\,, \tag{10}$$

while for low frequencies

$$\kappa_{eff} \sim \omega\, \Delta x^2\, Wo\,. \tag{11}$$

Here ω is the circular frequency,
Δx is the cross-stream average displacement of a fluid element over half the period of the oscillation, and
$Wo = L(\omega/\nu)^{1/2}$ is the Wormsley number which represents the ratio of the viscous response time to the period of the oscillation.

For a given frequency the heat transfer process was found to be most efficient for $Pr = \pi/Wo^2$ i.e. when the characteristic time, $\tau_k = L^2/\kappa$ associated with heat diffusion is equal to half the period of the oscillation. Fig. 15 illustrates this result for fluids with different diffusivities and $L = 1$ cm.

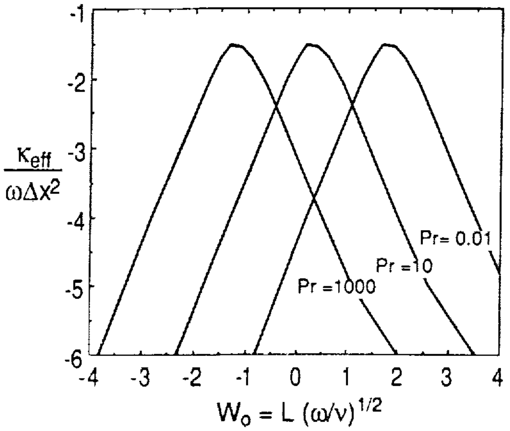

Fig. 15. Plot of effective diffusivity, κ_{eff} vs. Wormsely number Wo, after Kurzweg [31]

3.3 Linear Stability and Gravity Modulations

The stability of a heated fluid layer of infinite lateral extent is affected by gravity modulation and has received a limited amount of attention for the case of sinusoidally modulated gravity [74-77]. The static case, where the gravity vector is perpendicular to the layer and parallel to the temperature gradient, is stable unless the critical Rayleigh number is exceeded. The effect of gravity modulation is to introduce stability for given combinations of modulation amplitude and frequency for situations which in the absence of modulations would exhibit instability. In contrast, for the case where the gravity vector and the temperature gradient are anti-parallel (which is stable for a steady gravity vector), instability can occur due to gravity modulation.

The work of *Biringen* and *Peltier* [77] focused on the behavior of a 3-D Rayleigh-Bènard system subject to spatial and temporal gravity modulation. They used a pseudo-spectral method to examine the system numerically and studied the effects of sinusoidal and random gravity modulations with the gravity vector oriented perpendicular to the fluid layer. It was found that when the base acceleration was reduced from 1 *g* to zero, the system parameters that had resulted in a synchronous response at 1 *g* led to a conductive state for the modulated zero *g* case. The spatially random modulations about a zero *g* base acceleration led to excitations of the 3-D temperature field. These excitations were less pronounced than for the 1 *g* case. For temporally random modulations about zero *g*, the cases considered that where excited at 1 *g* no longer exhibited excitation.

The effect of oscillating accelerations and impulse forcing of an interface separating two immiscible fluids has recently been considered [78, 79]. Both these analyses are restricted to time-dependent accelerations with zero mean which are oriented perpendicular to the interface between the fluids. The linear stability of a basic state characterized by a planar interface and an oscillating pressure. For the case of an arbitrary oscillating disturbance it is shown that the linear evolution of an infinitesimal perturbation of the interface is governed by a single integro-differential equation. Except in the limit of zero surface tension the effect of viscosity is shown to be small. As surface tension becomes dominant, resonant instabilities are excited at lower and lower wavenumbers. The interface is found to be more unstable to impulse type forcing than to sinusoidal forcing [79].

3.4 Direct Numerical Simulation

The effects of low-gravity on the transport of heat and momentum have been examined in a number of articles [37, 60-71]. *Robertson* et al. [60, 61] found that for convection in circular cylinders with azimuthal variations in temperature at the boundary and the gravity vector applied perpendicular to the cylinder axis, the intensity of convection follows the prediction of Weinbaum's first order theory [96] for low Rayleigh numbers. Weinbaum's first order theory predicts a simple sinusoidal dependence of the maximum velocity as a function of orientation of the gravity vector. The effects of a variety of acceleration vectors (sinusoidal, cycloidal and linear periodic) on motion in three fluids corresponding to mercury, helium and water ($10^{-2} < Pr < 10$) were studied by *Spradley* et al. [62]. They found that the steady mean part of the applied disturbance is more important than the oscillatory part (frequency = 1 Hz) in determining the flow field and heat transfer. *Kamotani* et al. [37] solved a linearized approximation of the Boussinesq equations and investigated the effect of an applied acceleration consisting of a time mean part and an oscillatory part on the temperature and flow fields in a rectangular enclosure. They found that the thermal convection was predominantly oscillatory in nature. In addition they found that the acceleration perpendicular to the temperature gradient is the most important for the generation of fluid motion.

The response of natural convection of a Boussinesq fluid in a cylinder to residual acceleration has been examined by *Heiss* et al. [64], and *Schneider* and *Straub* [97]. In the work of *Heiss* et al. the calculations are three-dimensional and involve gravity pulses and a rotating gravity vector. The ends of the cylinder are held at different temperatures. The cylinder walls are taken to be either perfectly insulating or perfectly conducting. The results are presented in terms of the relevant dimensionless parameters in the original papers. Fig. 16 illus-

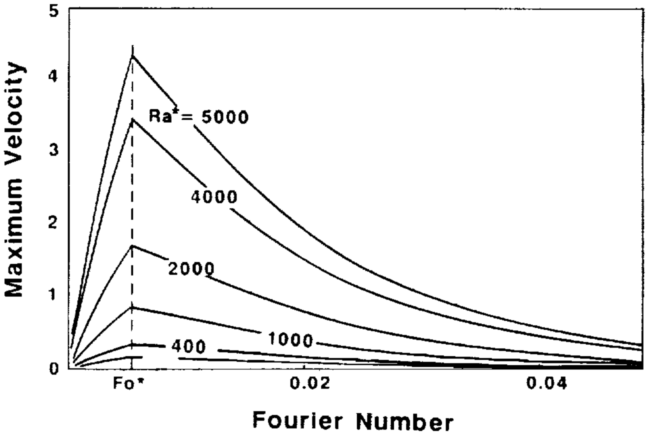

Fig. 16. Dimensionless maximum velocity caused by impulse disturbances as a function of Fourier number $F_0 = t\,\kappa^2/d$, after Heiss et al. [64]. Here t is the time [s], κ is the thermal diffusivity [$cm^2\,s^{-1}$], d is the diameter of the cylinder [cm]. The parameter Ra is the Rayleigh number associated with the disturbance which is of dimensionless duration $F_0^* = 5.5 \cdot 10^{-3}$. $Ra^* = \beta_T\, g\, L^3\, \Delta T/\nu\, \kappa$, where L is the cylinder length [cm], ΔT is the temperature difference between the ends of the cylinder [K], β_T is the coefficient of thermal expansion [K^{-1}], g is the magnitude of the acceleration [$cm\,s^{-2}$] and ν is the kinematic viscosity [$cm^2\,s^{-1}$]*

trates their results for impulse disturbances. The physical conditions were taken to correspond to: a cylinder of aspect ratio 1, with diameter = 1 cm, $\nu = 5 \cdot 10^{-3}$ cm^2 s^{-1}, $\kappa = 7.14 \cdot 10^{-3}$ cm^2 s^{-1}, $\beta = 2.5 \cdot 10^{-4}$, and a temperature difference, ΔT, of 25 K. The magnitude of the acceleration pulse (duration = 0.7 s) corresponding to a Rayleigh number, Ra^*, of 2,000 is $\sim 3 \cdot 10^{-3}$ g results in a maximum velocity of approximately 5.8 cm s^{-1}. The decay time for the flow field is about 5.6 s. Notice that for all the results, the decay time of the pulse is independent of the magnitude of Ra^*. For a rotating gravity vector of a given magnitude, the maximum velocity of the system is independent of the dimensionless frequency $f = f^* \, d^2/\kappa$, up to $f \sim 10$ whereupon it decreases rapidly with increasing frequency. For the fluid with the physical properties described in the previous example, f^* corresponds to $7.14 \cdot 10^{-2}$ s^{-1}.

Schneider and *Straub* [97] examined the effect of Prandtl number on the response to g-jitter for the same system as *Heiss* et al. They examined the response of the system to pulses of infinite length and sinusoidally varying pulses. For sinusoidal pulses they found for systems with $Pr = 0.71$ and 7.0 (air and water) that the maximum velocity decreased with increasing frequency for dimensionless frequencies, $F = f \, L^2/\kappa$, greater than 10. At $Pr = 7$ a maximum in the velocity was observed between $F = 10$ and 100 for the maximum amplitude pulse examined ($Ra = 2 \cdot 10^5$, or $|g| \approx 3 \cdot 10^{-4}$ g for a fluid with the properties of water, a 1 cm diameter cylinder and a temperature difference of 10 K). They determined that the system was least sensitive when the transient accelerations acted along the cylinder axis.

The extent to which gravity causes buoyancy-driven fluid motion (and thus, solute redistribution) during directional solidificaiton has been examined using numerical models of buoyancy-driven convection in cylindrical and rectangular geometries [9, 65-69, 84, 98-101]. Except for [9, 65-69] these studies are restricted to axisymmetric situations in which a steady gravity vector is oriented parallel to the axis of a cylindrical ampoule. *McFadden* and *Coriell* [66] have undertaken 2-D calculations of the effects of time-dependent accelerations on lateral compositional variations during directional solidification. The gravitational acceleration was assumed to have a uniform magnitude and rotation rate. The amount of compositional non-uniformity was found to increase with decreasing rate of rotation (see fig. 17).

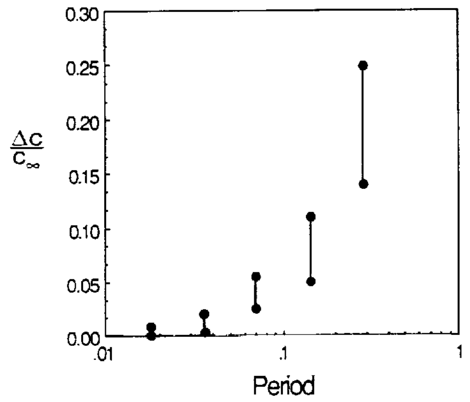

Fig. 17. Maximum lateral solute segregation $\Delta c/c_\infty$ (where c_∞ is the far-field solute concentration in the melt) in the crystal as a function of the period of the gravitational oscillation. After McFadden and Coriell [66]

Two- and three-dimensional models of directional solidification from dilute gallium-doped germanium melts have been used to determine the sensitivity of crystal compositional uniformity to both time-dependent and steady residual accelerations [9, 67, 69]. The specific boundary conditions, thermo-physical properties of the melt, growth rates and ampoule size are all found to play a role in the determination of the experiment sensitivity. For a given set of operating conditions, it is found that at growth rates on the order of 6.5 mm s^{-1} the orientation of the experiment with respect to the steady component of the residual gravity is a crucial factor in determining the suitability of the spacecraft as a means to suppress or eliminate unwanted effects caused by buoyant fluid motion. The worst case appears to be when the acceleration vector is parallel to the crystal interface. At growth rates on the order of microns per second, this orientation leads to compositional non-uniformities of 10-20% when the magnitude of the acceleration is of the order 10^{-6} g. If, however, the growth rate is lowered by an order of magnitude, the non-uniformity is reduced significantly (down to 1-5% in this case). Table 4 summarizes the results obtained for steady accelerations.

The directional solidification (Bridgman-Stockbarger) process is also extremely sensitive to transient disturbances. The response of the system to a variety of impulses will be discussed. For example, a $3 \cdot 10^{-3}$ g impulse of one second duration acting parallel to the interface of a growing crystal produces a response in the solute field which lasts for nearly 2,000 s. Consequently lateral and longitudinal compositional variations occur over a length of nearly 6 mm in the grown crystal.

The response of the solute field and the lateral non-uniformity to oscillatory accelerations varies from no response at all (at frequencies above 1 Hz with amplitudes below 10^{-3} g) to a significant response at 10^{-3} Hz at amplitudes on the order of 10^{-6} g. In addition, additive effects were observed for combinations of a steady and a low frequency residual acceleration component. These additive effects gave rise to significant lateral and longitudinal non-uniformities in concentration. A number of different types of periodic disturbances were employed. Single frequency disturbances of the form $g(t) = g_0 + g_n \cos(2\pi f_n t)$ were examined with $g_0 = 0$, $\sqrt{2} \cdot 10^{-6}$ and $\sqrt{2} \cdot 10^{-5}$ g, oriented parallel, perpendicular and at 45° to the crystal-melt interface. The frequency range examined was $f_n = 10^{-4}, 10^{-3}, 10^{-2}, 10^{-1}$, 1 and 10 Hz. For frequencies greater than 10^{-2} Hz, there were no discernable effects on the solute fields. The velocity field did, however, respond to the oscillatory disturbances. For the case of 10^{-3} Hz (at $5 \cdot 10^{-6}$ g) the response of the solute field was significant. Lateral and longitudinal non-uniformity levels in excess of 15% were calculated. Fig. 18-20 show the lateral non-uniformity as a function of time and highlights the additive effect of oscillatory and steady components of the residual acceleration.

The effect of a multiple frequency disturbance is illustrated in fig. 20. The acceleration consists of steady and periodic contributions with the form: $g(t) = g_0 + g_1 \cos(2\pi \, 10^{-3} t) + g_2 \cos(2\pi \, 10^{-2} t)$. Here $|g_0| = \sqrt{2} \cdot 10^{-6}$ g, $|g_1| = 3\sqrt{2} \cdot 10^{-6}$ g and $|g_2| = 3\sqrt{2} \cdot 10^{-5}$ g. The magnitude of

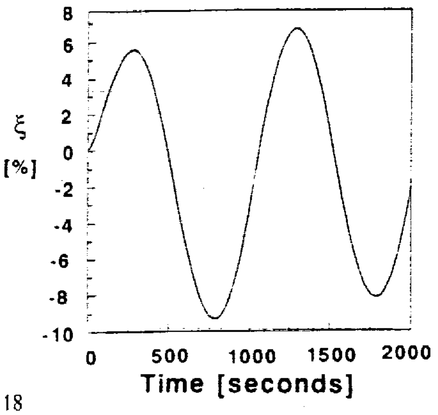

18

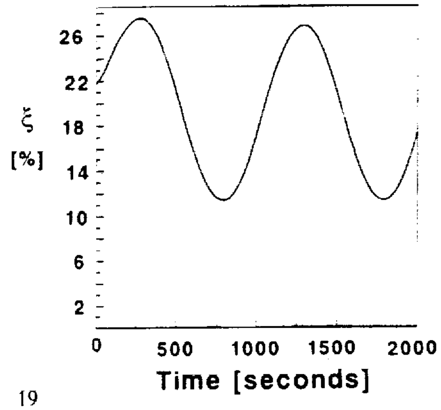

19

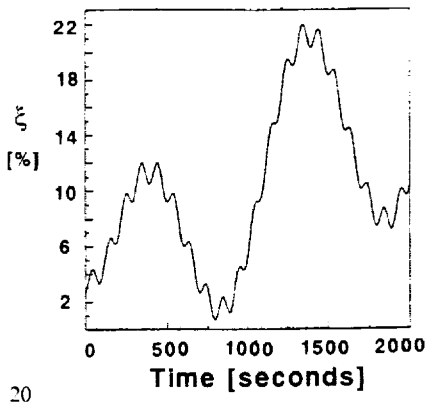

20

Fig. 18. Lateral non-uniformity in composition, ξ, plotted as a function of time for an oscillatory residual acceleration with a maximum magnitude of $3\sqrt{2}\cdot10^{-6}$ g and a frequency of 10^{-3} Hz, acting parallel to the crystal-melt interface [67]. The initial state was purely diffusive

Fig. 19. Lateral non-uniformity in composition, ξ, plotted as a function of time for a residual acceleration consisting of a steady part with magnitude $\sqrt{2}\cdot10^{-6}$ g and an oscillatory part with a maximum magnitude of $3\sqrt{2}\cdot10^{-6}$ g and a frequency of 10^{-3} Hz, acting parallel to the crystal-melt interface [67]. The calculation was started from a steady flow associated with a $\sqrt{2}\cdot10^{-6}$ g acceleration acting parallel to the interface

Fig. 20. Lateral non-uniformity in composition, ξ, plotted as a function of time for a multi-component disturbance consisting of a steady low g background plus two periodic components: $g(t) = g_0 + g_1 \cos(2\pi\ 10^{-3}\ t) + g_2 \cos(2\pi\ 10^{-2}\ t)$, where $|g_0| = \sqrt{2}\cdot10^{-6}$, $|g_1| = 3\sqrt{2}\cdot10^{-6}$, and $|g_2| = 3\sqrt{2}\cdot10^{-5}$ [67]. The calculation was started from a steady flow associated with a $\sqrt{2}\cdot10^{-6}$ g acceleration acting perpendicular to the interface

the compositional non-uniformity ξ is seen to vary with the frequencies of the acceleration. More recently, it has been shown [67] that, particularly at high frequencies, it is important to consider the long time behavior of the system, because for high frequency disturbances (≈ 0.1-1 Hz) the transient behavior of the system is more sensitive than the long time behavior. For example, the response to a 1 Hz 10^{-2} *g* acceleration was found to exhibit a concentration non-uniformity on the order of 10% during the first 80 s whereupon it decayed slowly to 1% of over a period of 2,500 s. In addition, calculations have been made using sample acceleration time histories obtained on *Spacelab* 3 (SL-3). The results varied according to the type of SL-3 data that were input. For the example shown in fig. 21. The response of the solute field was negligible, although the velocity field fluctuated on the order of the crystal growth rate. The system exhibited some response to transient disturbances (for example the structural response to thruster firings) that were superimposed on background low frequency acceleration. Low frequency (≤ 10^{-1} Hz) acceleration components with amplitudes of 10^{-3} *g* or more were also found to give rise to undesirable non-uniformity.

Griffin and *Mokatef* [72, 73] modelled the nature of melt convection in a Bridgman system subject to steady and unsteady axial acceleration. They also found that at conditions corresponding to low-gravity, the response time of the melt

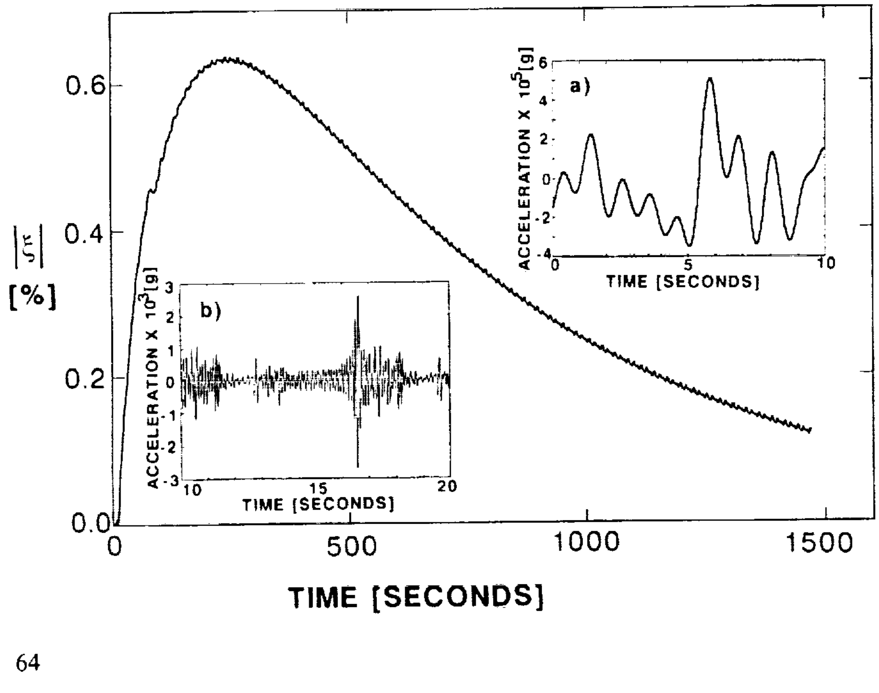

Fig. 21. Lateral non-uniformity |ξ| as a function of time for accelerations taken from a sample time series (see inset) constructed from data obtained on Spacelab 3 [69]. The acceleration consists of a repeated "noise" segment (length 10 s, 10^{-1} Hz < f < 1 Hz) and a thruster firing event (length 10 s, 10^{-1} Hz < f < 13 Hz). The latter is introduced at 10 and 80 s

Table 5. Compositional non-uniformity ξ [%] for Ge:Ga [9,80]; $\xi = (c_{smax} - c_{smin})/c_{sav}$, where c_s denotes the crystal composition at the melt-crystal interface

residual acceleration magnitude [g]		orientation		ampoule width [cm]			
				1		0.5	2.0
				growth rate [mm s^{-1}]			
		N	e_g	6.5	0.65	6.5	6.5
A)	10^{-4}	↑	←	80			
	10^{-5}		←	92.7	11.9	12.0	
			↙	70.9	11.3		
			↓	6.4	0.95		
	$5 \cdot 10^{-6}$		↓	3.2			
			↙	39			
			←	54.2			
	10^{-6}		←	11.3	2.0		
			↙	8.0			
			↓	0.7	0.0		
B)	10^{-5}		←	22.6			64.5
	10^{-6}		←	2.3			

e_g is the unit vector parallel to g, N is the normal vector to the crystal. L = 1 cm for all cases. Values in parentheses indicate 3-D results. All calculations were undertaken using the thermo-physical properties of gallium-doped germanium (9) and A) and B) refer to the operating conditions listed below.

Operating conditions

A) hot zone temperature (T_h) 1,331 K
distance between inlet and interface (L) 1.0 cm
height of adiabatic zone (L_a) 2.5 mm
ampoule width (diameter) 1.0 cm

B) hot zone temperature (T_h) 1,251 K

velocity is proportional to the momentum diffusion time (i.e. it is controlled by the characteristic system length scale and melt viscosity). In accord with the general trend exhibited by most physical systems discussed in this article, they found that the velocity response to sinusoidal g-jitter decreased as the inverse square of the momentum diffusion time.

A general conclusion that can be drawn from all attempts to characterize gravity-driven convective effects on directional solidification from two component melts is that the maximum lateral solute non-uniformity (radial segregation for the axisymmetric cases) occurs near the transition from diffusion dominated to convection dominated growth conditions [52, 84, 9]; that is, when convective velocities are of the same order of magnitude as the diffusive velocities. The conditions under which this "transition" takes place will depend on the specific nature of the forces driving convection. The orientation of the steady component of the gravity vector is crucial in determining the magnitude of the gravity vector at which this transition occurs. Thus, for a given set of operating conditions the orientation of the gravity vector determines the suitability of a low-gravity environment for directional solidification experiments.

Motivated by the growth of *t*riglycine *s*ulfate (TGS) crystals on *Spacelab* 3, [11], *Nadarajah* et al. [102] have examined the acceleration sensitivity of crystal growth from solution. Thermal and solutal convection were included in their analyses and the crystal growth rate was chosen as the sensitivity parameter for the response to convective transport. Simulations were carried out for steady, impulsive and periodic accelerations in order to determine tolerable acceleration levels. Long-time simulations of the experiment were conducted with steady background accelerations of 10^{-6} and 10^{-5} g. Impulsive and periodic disturbances of higher magnitudes were imposed at intermediate points. For steady accelerations the system was shown to have diffusion dominated transport at 10^{-6} g but for 10^{-5} g a transition to convection dominated transport occurs. Fig. 22 summarizes the results for oscillatory disturbances. For each case, the numbers correspond to the ratio $g \beta \Delta c / f v^*$, which is an estimate of the ratio of buoyancy to inertial forces. Here β is the solute expansion coefficent, Δc the characteristic concentration difference, f is the frequency of the acceleration and v^* is the calculated characteristic fluid velocity. Clearly, for this example, a simple estimate alone will not suffice to determine the system sensitivity. The system is relatively stable to impulsive and periodic disturbances unless their magnitudes are very large.

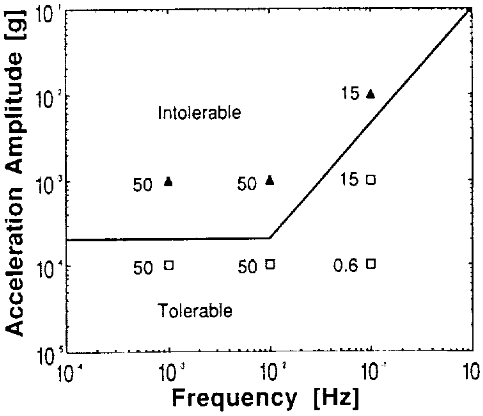

Fig. 22. Sensitivity of crystal growth from solution to various periodic disturbances. The solid line separates tolerable responses (10% or less growth rate fluctuations) from intolerable ones. For each case, the numbers correspond to the ratio $g \beta \Delta c / f v^*$, which is an estimate of the the ratio of bouyancy and inertial forces. After Nadarajah et al. [102]

4 Summary and Discussion

The work described in this paper examines the sensitivity of a variety of space experiments to residual accelerations. In all the cases discussed, the sensitivity is related to the dynamic response of a fluid. In some cases the sensitivity can be defined by the magnitude of the response of the velocity field. This response may involve motion of the fluid associated with internal density gradients, or the motion of a free liquid surface. For fluids with internal density gradients, the type of acceleration to which the experiment is sensitive will depend on whether buoyancy-driven convection must be small in comparison to other types of fluid motion (such as thermocapillary flow), or fluid motion must be suppressed or eliminated (such as in diffusion studies, or directional solidification experiments). In the latter case, the experiments (for example diffusion experiments and directional solidification experiments) are sensitive to steady and low frequency accelerations (< 10^{-2} Hz). For experiments such as the directional solidification of melts with two or more components, determination of the velocity response alone is insufficient to asses the sensitivity. The effect of the velocity on the composition and temperature field must be considered, particularly in the vicinity of the melt-crystal interface. As far as the response to transient disturbances is concerned the sensitivity is determined by both the magnitude and frequency the acceleration and the characteristic momentum and solute diffusion times.

The directional solidification of doped germanium crystals has been carried out on *Skylab* [17, 18, 103, 104] and the *Apollo-Soyuz* Test Project (ASTP) [105, 106]. The latter involved the directional solidification of seeded Ge melts. Melts were doped with gallium and some were doped with 1 % Si and 0.001 % Sb [105]. The results of these experiments revealed strong asymmetric non-uniformities in the space grown crystals. Lateral variations were also observed in samples grown under terrestrial conditions but were much less pronounced [25]. It has been argued that the asymmetric redistribution of the dopant can be ascribed to "barometric diffusion" of the solutes due to the acceleration gradient in the melt arising from the rotational motion of the spacecraft [105, 106]. The basis of the argument, however, appears to ignore the presence of gravity gradient and atmospheric drag effects and does not explicitly account for the spacecraft attitude motions. It has been demonstrated [9] that melt convection can occur in response to a low magnitude steady residual acceleration, and that whenever the acceleration vector is not aligned with the ampoule axis strong asymmetries in composition can occur. Since there is a non-linear dependence of compositional uniformity on convection, there is always the possibility that the observed non-uniformities in the terrestrially grown samples will be smaller than those observed in space grown samples. Thus, convection caused by residual acceleration cannot be discounted as the origin of the non-uniformities.

Thermocapillary flow experiments require that buoyancy effects are small in comparison to capillary effects. The estimated range of accelerations to which they are sensitive lies between $5 \cdot 10^{-3}$ Hz and 2 Hz for the most sensitive cases. Unless the magnitude of the effective buoyancy force (expressed through the Grashof number) associated with a given acceleration is on the order of or greater than $Rs\,(1 + S_r^{\,2})^{1/2}$, buoyancy effects are not likely to be significant. It is possible that more subtle effects of the acceleration environment might occur (for example influencing the transition from steady to oscillatory flow) but this cannot be determined by order of magnitude analysis. It is more likely that thermocapillary flow experiments will be most sensitive to the motion of the free surface in response to g-jitter.

The response of free surfaces to g-jitter has been examined through analytical and numerical models. For cylindrical liquid bridges this has been undertaken only for axial accelerations. The shape of the surface is most responsive to disturbances close to the natural frequency of the bridge and its harmonics. The sensitive frequencies lie in the $5 \cdot 10^{-3}$ - 10 Hz range, with maximum tolerable magnitudes from 10^{-8} - 10^{-3} g depending on the sensitivity criterion and the particular model employed.

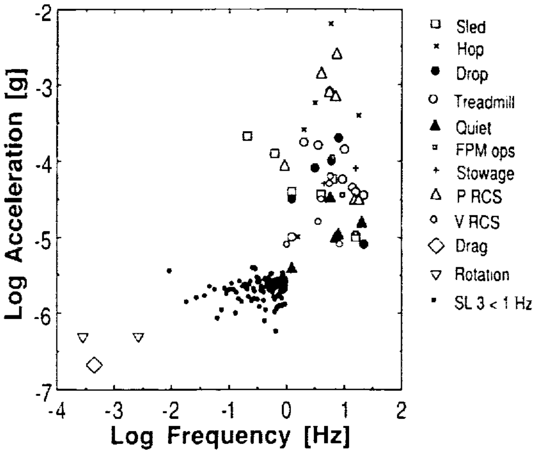

Fig. 23. Residual accelerations measured on orbit (in units of g = 9,8 m s⁻²). (Data courtesy of Dr. H. Hamacher, DLR, and M. J. B. Rogers Univ. of Alabama in Huntsville). The Spacelab 3 (SL-3) data are restricted to measured frequencies between 10⁻³ and 1 Hz. The points corresponding to Sled, Hop, Drop, Treadmill, Quiet, FPM ops, Stowage, refer to activities and experiments on the D-1 mission. FPM ops stands for Fluid Physics Module operations, P RCS and V RCS refer to the primary and vernier thrusters. The drag and rotation entries correspond to accelerations arising from slow variations in atmospheric drag during an orbit and attitude changes involving rotation

Fig. 23 depicts the range of measured acceleration amplitudes (courtesy of *Dr. H. Hamacher*, DLR, and *M. J. B. Rogers*, University of Alabama in Huntsville) as a function of frequency for several *Shuttle* missions. It should be remembered that in addition to the accelerations shown here there are gravity gradient and atmospheric drag accelerations with magnitudes on the order of 10^{-6} - 10^{-7} g which can be steady (for gravity gradient stabilized type attitudes) or have frequencies that are twice the orbital frequencies (for a solar inertial attitude). In fig. 24 we depict these together with g-tolerance curves selected from the examples discussed earlier. There is some overlap between the sensitivity curves and measured accelerations. Even if the fact that most of the curves are obtained for order of magnitude estimates is taken into account, it is clear that a careful evaluation of the interaction between experiments and the residual acceleration environment is necessary. One the experiment sensitivity has been determined (which may sometimes require a more de-

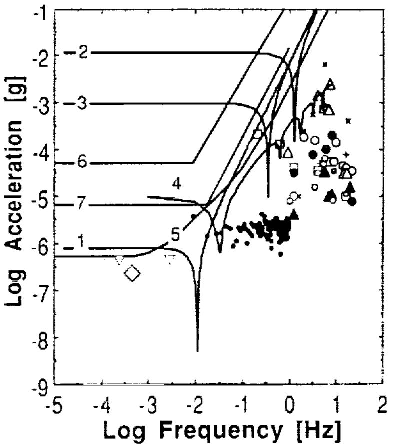

Fig. 24. Acceleration sensitivity curves from selected examples discussed earlier superimposed on fig. 23. Curves 1 and 3 correspond to the cases $n = 1$, $\Lambda = 0.9999$ and $n = 1$, $\Lambda = 0.9$ in fig. 12a, curve 2 corresponds to $n = 2$ and $\Lambda = 0.9999$ in fig. 12b. Curve 4 corresponds to the most sensitive case of zone shape change in fig. 13, and curves 5 and 6 respectively correspond to the semi-conductor and metal melt growth experiments from fig. 4. Curve 7 represents the thermo-diffusion experiment of fig. 5

tailed analysis than any discussed in this review) it should be possible for the experimenter to choose operating conditions which will minimize the effect of the predicted acceleration environment. Since flight opportunities are limited, it is particularly important that the chances of success for any given experiment be greatly improved by detailed modelling prior to flight. This will allow investigators to better anticipate undesirable effects of the prevailing residual acceleration conditions, and will ultimately lead to a better overall understanding of the physical system.

Acknowledgements

This work was supported by the National Aeronautical and Space Agency through grants NAG-8 724 and D. O. 41 from Marshall Space Flight Center. I would like to thank G. Martin and R. Naumann, for their encouragement and interest in this work, Arun Nadarajah, and Jalil Ouazzani for useful discussions, and Melissa Rogers and Franz Rosenberger for helpful discussions and their careful reading of the manuscript.

References

1. *Chassay, R. P., Schwaniger, Jr., A. J.:* NASA-TM 86585, December, 1986.
2. *Hamacher, H., Jilg, R., Mehrbold, U.:* Proc. 6th European Symposium Materials Sciences in Microgravity Conditions, Bordeaux, France (ESA SP-256 1987).
3. Proceedings of the Workshop on Measurement and Characterization of the Acceleration Environment On Board the Space Station, Guntersville Alabama, August 11–14, 1986 (Teledyne Brown Engineering, Huntsville Alabama 1987).
4. *Hamacher, H.:* In Materials Science in Space, *B. Feuerbacher, R. Naumann, H. Hamacher* (eds.) Springer, New York 1986, 31.
5. *Alexander, J. I. D., Lundquist, C. A.:* AIAA Journal 26 (1988) 34.
6. *Alexander, J. I. D., Lundquist, C. A.:* J. Astr. Sci. 35 (1987) 193.
7. *Camel, D., Favier, J. J., Rouzaud, A.:* ESA Contract Report, Gr-764.108, March 27, 1987.
8. *Monti, R.:* ESA Contract Report, R-66.525, Technosystems Report TS-7-87, April 1987.
9. *Alexander, J. I. D., Ouazzani, J., Rosenberger, F.:* J. Crystal Growth 97 (1989) 285.
10. *Beysens, D.:* In Materials Science in Space, *B. Feuerbacher, R. Naumann, H. Hamacher* (eds.) Springer, New York 1986, 191.
11. *Yoo, H.-D., Wilcox, W. R., Lal, R. B., Trollinger, J. D.:* In Materials Processing in the Reduced Gravity of Space Vol. 9, G. E. Rindone (ed.) North Holland, New York 1982, 399.
12. *van den Berg, L., Schnepple, W.:* In Materials Processing in the Reduced Gravity of Space Vol. 9., *G. E. Rindone* (ed.) North Holland, New York 1982, 349.
13. *van den Berg, L., Schnepple, W.:* Growth of Mercuric Iodide in Spacelab 3, Nuclear Instruments and Methods in Physics Research A283 (1989) 335.
14. *Wiedemeier, H., Chandra, D., Klaessig, F. C.:* J. Crystal Growth 51 (1980) 345.
15. *Cröll, A., Mueller, W., Nitsche, R.:* Proc. 6th European Symposium Materials Sciences in Microgravity Conditions, Bordeaux, France (ESA SP-256 1987) 87.
16. *Camel, D., Favier, J. J., Dupauy, M. D., Le Maguet, R.:* ibid., 317.
17. *Witt, A. F., Gatos, H. C., Lichtensteiger, M., Lavine, M. C., Hermann, C. J.:* J. Electrochem. Soc. 122 (1975) 276.
18. *Witt, A. F., Gatos, H. C., Lichtensteiger, M., Lavine, M. C., Hermann, C. J.:* J. Electrochem. Soc. 127 (1978) 832.
19. *Frohberg, G., Kraatz, K. H., Wever, H.:* Proc. 6th European Symposium Materials Sciences in Microgravity Conditions, Bordeaux, France (ESA SP-256, 1987) 585.
20. *Malméjac, Y., Frohberg, G.:* In Fluid Sciences and Materials Science in Space, A European Perspective, ed. *H. U. Walter* (Springer Berlin, 1987) 159.
21. *Brown, R. A.:* Lecture notes from the 6th International Summer School on Crystal Growth, Edinburgh, Scotland, June 1986.
22. *Polezhaev, V. I.:* Hydrodynamics, Heat and Mass Transfer during Crystal Growth, in Crystals 10 ed. *H. C. Freyhardt* (Springer Berlin, 1984).
23. *Ostrach, S.:* J. Fluids Engineering 105 (1983) 5.
24. *Rosenberger, F.:* Fundamentals of Crystal Growth I (Springer Berlin, 1979).
25. *Hurle, D. J. T., Müller, G., Nitsche, R.:* In Fluid Sciences and Materials Science in Space, A European Perspective, ed. *H. U. Walter* (Springer Berlin, 1987) 313.
26. *Taylor, G. I.:* Proc. Roy. Soc. London A 219 (1953) 186.
27. *Aris, R.:* Proc. Roy. Soc. London A 259 (1960) 370.
28. *Gill, W. N., Sankarsubramanian, R.:* Proc. Roy. Soc. London A 316 (1970) 341.
29. *Brocher, E.:* J. Fluid Mech. 133 (1983) 245.
30. *Kurzweg, U. H.:* J. Heat Transfer 107 (1985) 459.
31. *Kurzweg, U. H.:* J. Fluid Mech. 156 (1983) 291.
32. *Kavainy, M.:* Int. J. Heat and Mass Transfer 29 (1985) 2002.
33. *Joshi, C. H., Kamm, R. D., Drazen, J. M., Slutsky, A. S.:* J. Fluid Mech. 114 (1983) 245.
34. *Smith, R.:* J. Fluid Mech. 114 (1982) 379.
35. *Watson, E. J.:* J. Fluid Mech. 133 (1983) 233.
36. *Farrell, D., Larsen, W. E.:* Water Resources Res. 9 (1973) 173.
37. *Kamotani, Y., Prasad, A., Ostrach, S.:* AIAA Journal 19 (1981) 511.
38. *Monti, R., Favier, J. J., Langbein, D.:* In Fluid Sciences and Materials Science in Space, A European Perspective, ed. *H. U. Walter* (Springer Berlin, 1987) p. 637.
39. *Radcliffe, M. D., Drake, M. C., Zvan, G., Fowlis, W. W., Alexander, J. I. D., Roberts, G. D., Sutter, J. K., Bergman, E.:* In Proceedings of the American Chemical Society Meeting, New Orleans 1987.
40. *Martinez, I.:* Proc. 6th European Symposium Materials Sciences in Microgravity Conditions, Bordeaux, France (ESA SP-256, 1987) 235.
41. *Martinez, I., Haynes, J. M., Langbein, D.:* In Fluid Sciences and Materials Science in Space, A European Perspective, ed. *H. U. Walter* (Springer Berlin, 1987) 53.
42. *Langbein, D., Roth, U.:* Proc. 6th European Symposium Materials Sciences in Microgravity Conditions, Bordeaux, France (ESA SP-256, 1987) 183.
43. *Padday, J. F.:* Ibid. 49.
44. *Napolitano, L. G., Monti, R., Russo, G., Golia, C.:* Ibid. 191.
45. *Schwabe, D., Scharmann, A.:* Proc. 6th European Symposium Materials Sciences in Microgravity Conditions, Schlob Elmau FRG (ESA SP-222, 1984) 81.
46. *Napolitano, L. G., Monti, R., Russo, G.:* Ibid. 15.
47. *Rogers, M. J. B., Alexander, J. I. D.:* Submitted to the AIAA Journal of Spacecraft and Rockets (1990).
48. *Malkus, W. R.:* Science, 160865 (1968).
49. *Langbein, D.:* ESA Contract Report, BF-R-66.525, April 1987.
50. *Napolitano, L.:* Ann. N. Y. Acad. Sci. (1983) 278.
51. *Ostrach, S.:* Ann. Rev. Fluid Mech. 14 (1982) 313.
52. *Rouzaud, A., Camel, D., Favier, J. J.:* J. Crystal Growth 73 (1985) 149.
53. *Gebhardt, B.:* AIAA J. 1 (1963) 380.
54. *Dressler, R. F.:* J. Crystal Growth 54 (1981) 523.
55. *Langbein, D.:* Proc. 6th European Symposium Materials Sciences in Microgravity Conditions, Bordeaux, France (ESA SP-256, 1987) 221.
56. *Feuerbacher, B., Hamacher, H., Jilg, J.:* Preprint (DFVLR Köln, FRG, 1988).
57. *Dewandre, Th.:* Appl. Microgravity Tech. 1 (1988) 142.
58. *Fowlis, W. W., Roberts, G., Drake, M., Radcliffe, M.:* Determination of the Flow in the 3M company's space crystal growth experiments, to be published J. Crystal Growth (1989).
59. *Amin, N.:* Proc. R. Soc. Lond. A 419 (1988) 151.
60. *Robertson, S. J., Nicholson, L. A.:* Lockheed Report LMSC-HREC TR D867640 (1987).
61. *Robertson, S. J., Nicholson, L. A., Spradley, L. W.:* Lockheed Report LMSC-HREC TR D867624 (1982).
62. *Spradley, L. W., Bourgeois, S. W., Lin, F. N.:* AIAA paper 75-695 (1975).
63. *Grodzka, P. G., Bannister, T. C.:* AIAA paper 74-156 (1974).
64. *Heiss, T., Schneider, S., Straub, J.:* Proc. 6th European Symposium Materials Sciences in Microgravity Conditions, Bordeaux, France (ESA SP-256, 1987) 517.

65. *Polezhaev, V. I., Lebedev, A. P., Nikitin, S. A.:* Proc. 5th European Symposium on Materials Sciences under Microgravity, Schloß Elmau FRG, ESA SP-222 (1984) 237.
66. *McFadden, G. B., Coriell, S. R.:* In Proc. AIAA/ASME/SIAM/APS 1st National Fluid Dynamics Congress, Cincinnati, July 25th-28th (1988) p. 1572.
67. *Alexander, J. I. D., Ouazzani, J., Rosenberger, F.:* Proc. 3rd International Colloquium on Drops and Bubbles, AIP Conference Proceedings 197, ed. Taylor G. Wang (American Institute of Physics, New York, 1988) p. 112.
68. *Alexander, J. I. D., Ouazzani, J.:* Proc. 6th International Conference on Num. Methods in Laminar and Turbulent Flow, *C. Taylor, P. Gresho, R. L. Sani and J. Häuser* (eds.) Pineridge, Swandea 1989, 1035.
69. *Alexander, J. I. D., Amiroudine, S., Ouazzani, J., Rosenberger, F.:* Analysis of the Low Gravity Tolerance of the Bridgman-Stockbarger Technique. II: Transient and periodic accelerations, in preparation 1989.
70. *Arnold, W. A., Jacqmin, D. A., Chang, R., Chait, A.:* AIAA paper No. 89 (1989).
71. *Ramachandran, N., Winter, C.:* AIAA Paper No. 90-0654 (1990).
72. *Griffin, P. R., Mokatef, S.:* Appl. Microgravity Tech. 2 (1989) 121.
73. *Griffin, P. R., Mokatef, S.:* Ibid. 128.
74. *Gresho, P. M., Sani, R. L.:* J. Fluid Mech. 40 (1970) 783.
75. *Gershuni, G. Z., Zhukovitskii, E. M.:* Convective stability of incompressible fluids (Israel program for scientific translations, Jerusalem 1976).
76. *Hadid, H. B., Roux, B., Randriamapianiana, A., Crespo, E., Bontoux, P.:* Proc. NATO Conf. on Phys.-Chem. Hydrodyn. Spain, July (1986).
77. *Biringen, S., Peltier, L. J.:* Proc. 27th Aerospace Science Mtg., Reno, Nevada 1989, AIAA Paper No. 89-0068.
78. *Jacqmin, D., Duval, W. M. B.:* J. Fluid Mech. 196 (1988) 495.
79. *Jacqmin, D., Williams, M. D.:* unpublished research, NASA Lewis Research Center, Cleveland (1988).
80. *Alexander, J. I. D., Rosenberger, F.:* Bridgman Crystal Growth in low gravity: A scaling analysis to appear in Low Gravity Fluid Dynamics and Transport Phenomena, *J. Kosher* and *R. Sani* (eds.) AIAA, 1990.
81. *Ch.-H. Chun:* Proc. 6th European Symposium Materials Sciences in Microgravity Conditions, Bordeaux, France (ESA SP-256, 1987) 271.
82. *M. D. Lind:* AIAA-Paper 87-0618 (25th Aerospace Sciences Meeting, Reno, January 19-27, 1987).
83. *Camel, D., Favier, J. J.:* J. de Physique 47 (1986) 1001.
84. *Chang, C. J., Brown, R. A.:* J. Crystal Growth 63 (1983) 353.
85. *Kimura, S., Bejan, A.:* Phy. Fluids 28 (1985) 2980.
86. *Martinez, I.:* Proc. 5th European symposium on materials sciences under microgravity. Schloß Elmau FRG, ESA SP-222 (1984) 31.
87. *Haynes, J.:* Ibid. 43.
88. *Padday, J. F.:* Ibid. 251.
89. *Sekerka, R. F., Coriell, S. R.:* Proc. 3rd. Symposium on Material Science in Space, Greneble, France (ESA SP-142, 1989) 55
90. *Coriell, S. R., Hardy, S. C., Cordes, M. R.:* J. Colliod Interface Sci. 60 (1976) 126.
91. *Chang, C. E., Wilcox, W. R.:* J. Crystal Growth 28 (1975) 8.
92. *Zhang, Y. Q., Alexander, J. I. D.:* Submitted to Physics of Fluids (1990).
93. *Heywang, W.:* Z. Naturforschg. 11a (1956) 238.
94. *Coriell, S. R., Hardy, C., Cordes, M. R.:* J. Crystal Growth 42 (1977) 466.
95. *Duranceau, J. L., Brown, R. A.:* J. Crystal Growth 75 (1986) 367.
96. *Weinbaum, S.:* J. Fluid Mech. 18 (1964) 409.
97. *Schneider, S., Straub, J.:* J. Crystal Growth 97 (1989) 235.
98. *Clark, P. A., Wilcox, W. R.:* J. Crystal Growth 50 (1980) 461.
99. *Kobayashi, N., Wilcox, W. R.:* J. Crystal Growth 59 (1982) 616.
100. *McFadden, G. B., Rehm, R. G., Coriell, S. R., Clark, W., Morrish, K. A.:* Metall. Trans. A 15 (1984) 2125.
101. *Adornato, P. M., Brown, R. A.:* J. Crystal Growth 80 (1987) 155.
102. *Nadarajah, A., Rosenberger, F., Alexander, J. I. D.:* To appear J. Crystal Growth (1990).
103. *Yue, J. T., Voltmer, F. W.:* J. Crystal Growth 29 (1975) 329.
104. *Gatos, H. C.:* In Materials Processing in the Reduced Gravity Environment of Space ed. *G. Rindone* (Elsevier New York, 1982) 355.
105. *Zemskov, V. S.:* Soviet Physics Dokl. 22 (1977) 170.
106. *Zemskov, V. S., Shul'pina, I. L., Titkov, A. N., Belokurova, I., Guseva, N. B., Safarov, V. I.:* Soviet Phys. Solid State 21 (1979) 576.

Appendix 2

Sensitivity of liquid bridges subject to axial residual acceleration

91A15161

Yiqiang Zhang and J. Iwan D. Alexander
Center for Microgravity and Materials Research, University of Alabama in Huntsville, Huntsville, Alabama 35899

(Received 2 April 1990; accepted 2 August 1990)

It has become evident that the float zone crystal growth method and isothermal liquid bridges may be very sensitive to the residual acceleration environment of a spacelab. Indeed, the shape equilibria show a high degree of sensitivity and, thus, even the small steady acceleration associated with the effective low gravity environment of a spacecraft cannot be ignored. Using a slender-body approximation, the problem of determining the axisymmetric response of the shape of the free surface of a cylindrical liquid column bounded by two solid regions is modeled by a 1-D system of nonlinear equations. It is found that the sensitivity of the zone shape depends on the static Bond number, B_0, aspect ratio, and viscosity, as well as the amplitude and frequency of the disturbance. The general trend is an increase in tolerable residual gravity with increasing frequency. At the eigenfrequencies of the zone, however, there are dramatic deviations from this trend. At these frequencies the tolerable residual gravity level can be two orders of magnitude lower at this frequency. For the cases considered the values of B_0 were taken to be 0.002 and 0.02 and the dimensionless viscosities, $C = \nu(\rho/\gamma R_0)^{1/2}$, used were in the range 0.001–0.01. Aspect ratios ranging from 96.3% to 82.7% of the Rayleigh limit were examined. For these cases, the frequencies associated with the lowest tolerable acceleration have been found in the 10^{-2}–10^{-1} Hz range. In terms of previously recorded and predicted residual accelerations, the sensitive frequency ranges for the cases examined are 10^{-2}–10^{-1} Hz and 1–10 Hz. Maximum tolerable residual gravity levels as low as $10^{-6}\,g$ have been calculated. The effect of viscosity is seen to increase the tolerable acceleration level for all frequencies. The equilibrium shape, as determined by the steady background acceleration, has a pronounced effect at low frequencies. A change in slenderness of the bridge markedly changes the sensitivity to residual acceleration as the Rayleigh limit is approached.

I. INTRODUCTION

The low gravity environment of a spacecraft affords the opportunity to eliminate or minimize the often undesireable effects of gravity on fluid behavior. Both the fluid physics and the materials preparation community have an interest in the sensitivity of liquid zones to residual accelerations. A truly zero-gravity environment is never achieved and the residual acceleration that arises due to gravity gradient, atmospheric drag, crew motion, structural vibration, etc.,[1-3] is characterized by an ever changing magnitude and orientation and affects the relative motion of any mass in the spacecraft reference frame. Whether a particular space flight experiment involves the study of isothermal zone shapes, or attempts to utilize the low gravity environment to maximize the length of the liquid zone in a float-zone crystal growth experiment, the effects of residual acceleration must be considered.[4] Experiments involving free surfaces of low viscosity liquids are sensitive to acceleration. Indeed, for some space experiments, unexpected results have been attributed to residual accelerations in several cases.[5-9] Martinez[5] and Haynes[6] comment on the effects of an attitude change during the study of liquid column stability and liquid spreading kinetics on Spacelab-1. The residual acceleration environment also had a noticeable effect on stationary fluid masses. Roll rates of 0.13°/sec were apparently "...sufficient to interfere strongly with some of the fluid configurations studied... ."[8] Later experiments on D-1 that involved static and rotating liquid columns also experienced some interference that has been attributed to the residual acceleration environment.[7] In particular, Martinez recorded the following interference apparently caused by the residual acceleration environment. During the initial stages of the establishment of a long cylindrical column by liquid injection, a large amplitude deformation of the bridge was observed in response to shuttle maneuvers. Following this, a 10 cm liquid column exhibited a pronounced random oscillation.

In an experiment seeking to excite a *c*-mode deformation[7] of the bridge an amphora mode[7] resulted. The residual acceleration environment seems to have caused a shift in the stability limits. The maximum residual acceleration recorded during these experiments was $10^{-4}\,g$.

In Table I we have expressed the Bond number $B_n = (\rho g R_0^2/\gamma) g_n/g$, where γ is the surface tension, R_0 is the radius of the ends of the zone, ρ is the liquid density, g_n is the acceleration magnitude, and $g = 980$ cm sec^{-2}, for the physical properties of liquid columns used in two of the space experiments discussed earlier. These estimates indicate that the experiment involving the long liquid bridges should be more sensitive. In contrast to Martinez, none of Padday's experiments were reported to have been affected by the residual accelerations.

The numerical modeling of the response of a free liquid surface to time-dependent residual accelerations is complicated by the nonlinearity introduced by the free boundary motion. Few studies have been conducted on this subject.

0899-8213/90/111966-09$02.00 © 1990 American Institute of Physics

PRECEDING PAGE BLANK NOT FILMED

TABLE I. Dynamic Bond numbers estimated for two D-1 liquid zone experiments in which 5 cS silicone oil was used.

	Martinez[5]	Padday[6]
$\rho(\mathrm{g\,cm^{-3}})$	0.92	0.92
$L(\mathrm{cm})$	10	1.5
$\gamma(\mathrm{dyn\,cm^{-1}})$	0.2	0.19
B_n	$4.5(10)^{-4} g_n/g$	$7.1(10)^{-3} g_n/g$

Furthermore, the models to date are based on the assumption of an inviscid bridge,[10,11] or have dealt with a linearized 1-D model.[12] Thus, we have formulated a simple nonlinear 1-D model of a viscous isothermal liquid zone and used it to examine the effect of g jitter oriented parallel to the zone axis. This allows an examination of interaction between various components of a typically complex residual acceleration without the restriction that the response necessarily be linear. The model is based on a formulation developed by Lee,[13] which has been successfully applied to several types of liquid bridge problems.[10,11,14-18]

We have examined the effects of single frequency g-jitter disturbances. The zone response is described in terms of its deviation from its equilibrium shape. The equilibrium shape depends on the value of the steady background acceleration. The sensitivity is expressed in two ways: first *zone breakage*, defined in terms of the conditions under which the zone radius goes to zero, and second in terms of a *shape change criterion*, which indicates when the zone deviates more than 5% from its equilibrium shape. An optimal searching scheme is used to find the sensitivity limits of the bridge.

II. FORMULATION OF THE MODEL EQUATIONS

Consider a slender liquid bridge (see Fig. 1) held between two parallel rigid circular disks of radius R_0 separated by a distance L. The disks are aligned coaxially. The liquid is an isothermal incompressible Newtonian fluid with constant physical properties. It is held in place by capillary forces. Consistent with our aim to isolate the mechanical response of the surface to an acceleration $g(t)$ acting along the cylinder axis we make the following additional assumptions:

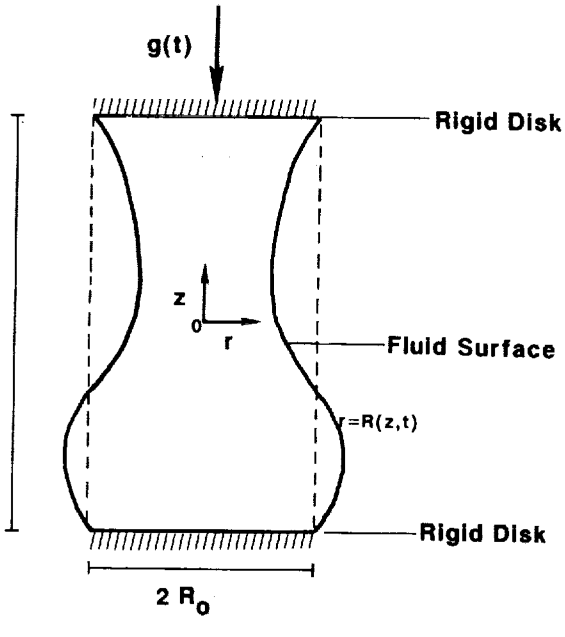

FIG. 1. Idealized liquid zone configuration.

(i) Internal motion of the liquid bridge is caused *only* by capillary pressure gradients caused by deformation of the surface.

(ii) The effect of the atmosphere around the bridge is negligible.

(iii) The interaction of the residual acceleration environment with the experiment apparatus is such that the top and bottom disks vibrate in phase and the frame of reference for the calculations is then conveniently taken to be attached to the disks.

The governing equations are rendered nondimensional using R_0, $(\rho R_0^3/\gamma)^{1/2}$, and $R_0(\rho R_0^3/\gamma)^{-1/2}$ to, respectively, scale distance, time, and velocity. Here ρ is the mass density and γ is the surface tension. The dimensionless equations for mass and momentum transfer then take the following form.

In the liquid $(0<r<R(z,t),\ -\Lambda<z<\Lambda)$,

$$\frac{1}{r}\frac{\partial(ru)}{\partial r}+\frac{\partial w}{\partial z}=0, \tag{1}$$

$$\frac{\partial u}{\partial t}+u\frac{\partial u}{\partial r}+w\frac{\partial u}{\partial z} = -\frac{\partial p^*}{\partial r}+C\left(\frac{\partial^2 u}{\partial r^2}+\frac{1\partial u}{r\,\partial r}+\frac{\partial^2 u}{\partial z^2}-\frac{u}{r^2}\right), \tag{2}$$

$$\frac{\partial w}{\partial t}+u\frac{\partial w}{\partial r}+w\frac{\partial w}{\partial z} = -\frac{\partial p^*}{\partial z}+C\left(\frac{\partial^2 w}{\partial r^2}+\frac{1\partial w}{r\,\partial r}+\frac{\partial^2 w}{\partial z^2}\right), \tag{3}$$

where p^* is a reduced pressure given by $p^*=p+B_0 g(t)z$, and $C=\nu(\rho/\gamma R)^{1/2}$ (with ν the kinematic viscosity) is a measure of the relative strength of viscous and capillary forces. The function $g(t)$ is given by $g(t)=1+(B_1/B_0)\sin\omega t$, where ω is the dimensionless circular frequency. Here, $B_0=g_0\rho R_0^2/\gamma$ is the usual static Bond number and $B_1=g_1\rho R_0^2/\gamma$ is a dynamic Bond number. We define the aspect ratio as $\Lambda=L/2R_0$, where L is the zone length. The magnitudes of the steady and time-dependent acceleration components are given by g_0 and g_1, respectively. The linear frequency (Hz) of the disturbance is given by $f=\omega(\rho R_0^3/\gamma)^{-1/2}/2\pi$.

The boundary conditions at the surface $r=R(z,t)$ are

$$p^*-\frac{2C}{(1+R_z^2)}\left[\frac{\partial u}{\partial r}+R_z^2\frac{\partial w}{\partial z}-R_z\left(\frac{\partial w}{\partial r}+\frac{\partial u}{\partial z}\right)\right] = \frac{1}{(1+R_z^2)^{3/2}}\left(\frac{1+R_z^2}{R}-R_{zz}\right)+B_0 g(t)z, \tag{4}$$

$$C\left[2R_z\left(\frac{\partial u}{\partial r}-\frac{\partial w}{\partial z}\right)\right]+(1-R_z^2)\left(\frac{\partial w}{\partial r}+\frac{\partial u}{\partial z}\right)=0, \tag{5}$$

which, respectively, represent the balance of normal and tangential force components at the surface. In addition, there is the kinematic condition

$$\frac{\partial R}{\partial t} - u + w\frac{\partial R}{\partial Z} = 0. \tag{6}$$

The conditions at $z = \pm \Lambda$ are

$$R(z,t) = 1, \quad w(r,z,t) = u(r,z,t) = 0, \tag{7}$$

which fixes the contact line between the disk and the liquid and ensures no slip of the fluid in contact with the disk. At $r = 0$ the conditions

$$u(0,z,t) = 0, \quad \frac{\partial w}{\partial r}(0,z,t) = 0, \tag{8}$$

ensure axisymmetry. The formulation is complete upon specifying suitable initial conditions that we take in the form

$$R(z,0) = R_0(z), \quad w(r,z,0) = u(r,z,0) = 0, \tag{9}$$

along with the constraint that the volume remain constant, i.e.,

$$\int_{-\Lambda}^{+\Lambda} R_0^2(z)dz = \int_{-\Lambda}^{+\Lambda} R^2(z,t)dz = 2\Lambda. \tag{10}$$

The above system of equations defines an unsteady free boundary problem since the location (and hence the shape) of the oscillating surface is *a priori* unknown and must be determined as part of the solution.

In order to calculate the response of the shape of the liquid zone to time-dependent axial accelerations, we approximate the system of equations presented in the last section and formulate a one-dimensional model. This considerably reduces the complexity of the problem and allows an examination of a relatively wide range of parameters without excessive computation times. Meseguer[10] used a one-dimensional model that is valid provided the slenderness Λ is large. (Recall that the slenderness of a static bridge is bounded from above by the Rayleigh limit, i.e., $\Lambda_{\max} = \pi$.) If radial momentum effects are neglected[15] then Eqs. (2) and (3) become decoupled and the following system of equations results:

$$\frac{1}{r}\frac{\partial (ru)}{\partial r} + \frac{\partial w}{\partial z} = 0, \tag{11}$$

$$\frac{\partial w}{\partial t} + w\frac{\partial w}{\partial z} = -\frac{\partial p^*}{\partial z} + C\frac{\partial^2 w}{\partial z^2}, \tag{12}$$

Since w is now depends only on z, Eq. (11) is easily integrated and yields

$$u(r,z,t) = -\frac{r\partial w}{2\partial z}. \tag{13}$$

Following Lee[13] and Meseguer[10] we take $S = R^2(z,t)$ and $Q = S(z,t)w(z,t)$ and substitute (13) into the kinematic boundary condition (6). This yields

$$\frac{\partial S}{\partial t} + \frac{\partial Q}{\partial z} = 0, \tag{14}$$

which expresses conservation of mass at the surface. Similarly, Eq. (12) can be recast in the form

$$\frac{\partial Q}{\partial t} + \frac{\partial}{\partial z}\left(\frac{Q^2}{S}\right) = -S\frac{\partial p^*}{\partial z} + SC\frac{\partial^2}{\partial z^2}\left(\frac{Q}{S}\right), \tag{15}$$

which expresses the conservation of momentum in the axial direction for each cross section of the zone. At the surface, the component of force balance normal to the surface reduces to

$$\begin{aligned} p^* = {} & \frac{C}{4S + (\partial S/\partial z)^2}\left\{\left[2\left(\frac{\partial S}{\partial z}\right)^2 - 4S\right]\frac{\partial}{\partial z}\left(\frac{Q}{S}\right) \right. \\ & \left. + 2S\frac{\partial S}{\partial z}\frac{\partial^2}{\partial z^2}\left(\frac{Q}{S}\right)\right\} + 4\left[4S + \left(\frac{\partial S}{\partial z}\right)^2\right]^{-3/2} \\ & \times\left[2S + \left(\frac{\partial S}{\partial z}\right)^2 - S\frac{\partial^2 S}{\partial z^2}\right] + B_0 g(t)z, \end{aligned} \tag{16}$$

where Eq. (14) and the expressions for S and Q have been used to replace u and w. Together with the following boundary and initial conditions, Eqs. (15) and (16) complete our approximate description of the physical system

$$\begin{aligned} & S(\pm\Lambda,t) = 1, \quad Q(\pm\Lambda,t) = 0, \\ & S(\pm\Lambda,0) = S_0(z), \quad Q(\pm\Lambda,0) = 0. \end{aligned} \tag{17}$$

III. SOLUTION METHOD

The time-dependent response of the shape of a liquid zone to axial residual accelerations was calculated and curves describing the tolerable acceleration as a function of the frequency of the axial acceleration were obtained for a variety of conditions. The initial shape was determined from computed static shapes corresponding to the static Bond number B_0 using a method similar to that employed by Meseguer and Sanz.[15]

A. Iteration procedure

In order to facilitate the solution of the system of equations (14)–(17) it is convenient to recast (15) and (16) in the form

$$\begin{aligned} & \frac{\partial Q}{\partial t} + \frac{\partial}{\partial z}\left(\frac{Q^2}{S}\right) \\ & \quad = -S\frac{\partial p^*}{\partial z} + CA(S)\frac{\partial^2}{\partial z^2}\left(\frac{Q}{S}\right) + CB(S)\frac{\partial}{\partial z}\left(\frac{Q}{S}\right), \end{aligned} \tag{18}$$

$$\begin{aligned} p^* = {} & \frac{C}{4S + (\partial S/\partial z)^2}\left[2S\frac{\partial S}{\partial z}\frac{\partial^2}{\partial z^2}\left(\frac{Q}{S}\right)\right] \\ & + 4\left[4S + \left(\frac{\partial S}{\partial z}\right)^2\right]^{-3/2} \\ & \times\left[2S + \left(\frac{\partial S}{\partial z}\right)^2 - S\frac{\partial^2 S}{\partial z^2}\right] + B_0 g(t)z, \end{aligned} \tag{19}$$

where

$$A(S) = S\left\{\left[8S - \left(\frac{\partial S}{\partial z}\right)^2\right]\left[4S + \left(\frac{\partial S}{\partial z}\right)^2\right]^{-1}\right\} \tag{20}$$

and

$$\begin{aligned} B(S) = S & \left\{\left[12\left(\frac{\partial S}{\partial z}\right)^3 - 24S\frac{\partial S}{\partial z}\frac{\partial^2 S}{\partial z^2}\right]\right. \\ & \left. \times\left[4S + \left(\frac{\partial S}{\partial z}\right)^2\right]^{-2}\right\}. \end{aligned} \tag{21}$$

The solution scheme is based on a fully implicit time stepping procedure. However, since the position of the surface is unknown an iterative procedure is required to obtain solutions to the differential equations and the location of the surface at each time. At the $(n+1)$th time step the iterations proceed as follows.

(i) Guess the surface shape for the initial iterate $(m=1)$.

(ii) The pressure p^* at the $(m+1)$th iterate is calculated in the following way. All terms in (19) are calculated from the previous (mth) iterate except for the leading viscous term. This is calculated from the solutions obtained at the previous [nth, $(n-1)$th] time steps using an Adams–Bashforth two-step approximation.

(iii) Q is then obtained upon solution of the momentum equation (18) and boundary conditions (17) using a Briley–McDonald implicit method.[19-21]

(iv) The surface shape at the $(m+1)$th iterate is then obtained from a time-centered discretization of (14).

(v) The surface shape is then compared with the initial guess (or the shape calculated at the mth iterate). The procedure is repeated until the condition

$$\max(|S_i^{m+1} - S_i^m|/S_i^m) < \varepsilon, \tag{22}$$

where $\varepsilon \ll 1$, is satisfied. Here a subscript "i" denotes the value of s at the ith point, while the superscript denotes the iterative step. The above procedure is repeated at each time step.

The Briley–McDonald method used to solve (18) involves the evaluation of the nonlinear advection term at the $(n+1)$th time step using

$$\left(\frac{\partial(Q^2/S)}{\partial z}\right)_i^{n+1} = \left(\frac{\partial(Q^2/S)}{\partial z}\right)_i^n + \Delta t\left[\frac{\partial}{\partial z}\left(\frac{\partial(Q^2/S)}{\partial t}\right)\right]_i^n + O[(\Delta t)^2], \tag{23}$$

where the time derivative has been approximated using a forward difference and the space derivative has been approximated with a centered difference. A Crank–Nicolson scheme is used to increase the accuracy of the solution. The discretized form of (18) then becomes

$$\begin{aligned} &\frac{Q_i^{n+1} - Q_i^n}{\Delta t} + \left(\frac{\partial(Q^2/S)}{\partial z}\right)_i^n + \frac{\Delta t}{2}\left[\frac{\partial}{\partial z}\left(\frac{\partial(Q^2/S)}{\partial t}\right)\right]_i^n \\ &= -\frac{1}{2}\left[\left(S\frac{\partial p^*}{\partial z}\right)_i^{n+1} + \left(S\frac{\partial p^*}{\partial z}\right)_i^n\right] \\ &\quad + \frac{C}{2}\left[A(S)\frac{\partial^2}{\partial z^2}\left(\frac{Q}{S}\right) + B(S)\frac{\partial}{\partial z}\left(\frac{Q}{S}\right)\right]_i^{n+1} \\ &\quad + \frac{C}{2}\left[A(S)\frac{\partial^2}{\partial z^2}\left(\frac{Q}{S}\right) + B(S)\frac{\partial}{\partial z}\left(\frac{Q}{S}\right)\right]_i^n, \end{aligned} \tag{24}$$

where a centered difference is used for spatial discretization. Equation (24) is unconditionally stable and has second-order accuracy with a truncation error of $O[(\Delta x)^2, (\Delta t)^2]$.

In addition to the boundary conditions (17) we also need to evaluate the pressure at the disks. This is achieved as follows. First we use the fact that $\partial s/\partial t = 0$ at $z = \pm\Lambda$ which implies $\partial Q/\partial z = 0$ [from (14)] and that $\partial Q/\partial t = 0$ at $z = \pm\Lambda$. We can then obtain the pressure from (18) evaluated at $z = \pm\Lambda$. This requires the evaluation of $\partial p/\partial z$ and $\partial^2 Q/\partial z^2$ at $z = \pm\Lambda$. The pressure derivative is approximated using the following standard three-point forward difference expression:

$$\left(\frac{\partial p}{\partial z}\right)_{z=\pm\Lambda} = \pm\frac{p_2 - 4p_1 + 3p_0}{2\Delta z} + O(\Delta z^3), \tag{25}$$

where, $p_0 = p(\pm\Lambda)$, $p_1 = p(\pm\Lambda \mp \Delta z)$, $p_2 = p(\pm\Lambda \mp 2\Delta z)$, and Δz is the spatial step size. Similarly, at $z = \pm\Lambda$, $\partial^2 Q/\partial z^2$ is evaluated using

$$\left(\frac{\partial^2 Q}{\partial z^2}\right)_{z=\pm\Lambda} = \frac{8Q_1 - Q_2 - 7Q_0}{2\Delta z^2} + O(\Delta z^4), \tag{26}$$

where $Q_1 = Q(\pm\Lambda \mp \Delta z)$, $Q_2 = Q(\pm\Lambda \mp 2\Delta z)$, and the fact that $\partial Q/\partial z = 0$ has been employed. Upon substitution of (25) and (26) into (18) and rearranging terms we obtain p_0 with second-order accuracy.

The system of discretized equations and boundary conditions is solved using a Thomas algorithm (method of factorization).[19]

B. Initial iterate

For this method of solution the choice of surface shape for the initial iterate at each time step affects the speed of convergence. For a poor choice the iteration may even fail to converge. To ensure that the initial iterate is reasonably close to the solution, the following formula is employed:

$$S_i^{n+1} = S_i^n + \Delta t\left(\frac{\partial S}{\partial t}\right)_i^n + \frac{1}{2}(\Delta t)^2\left(\frac{\partial^2 S}{\partial t^2}\right)_i^n. \tag{27}$$

For the computations presented here the number of iterations required was six or less whenever (22) was satisfied for the initial iterate.

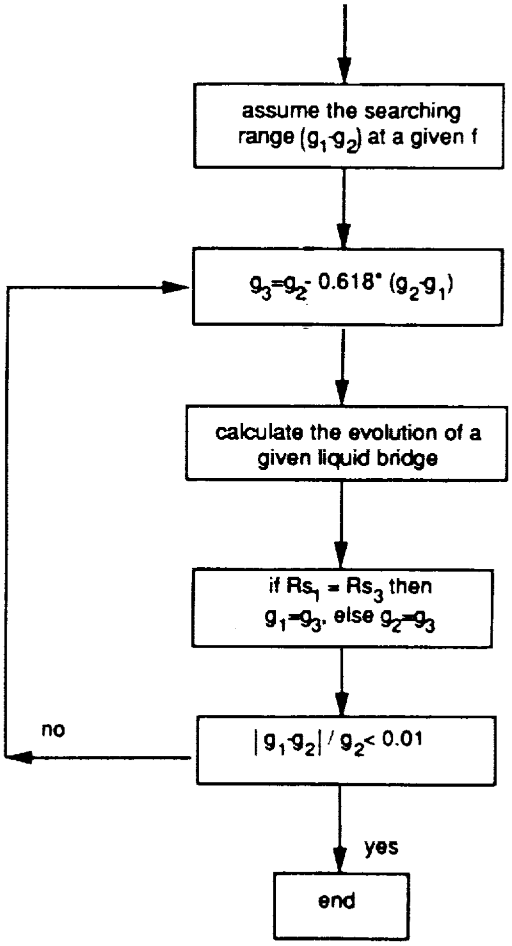
assume the searching range (g1-g2) at a given f
g3=g2- 0.618* (g2-g1)
calculate the evolution of a given liquid bridge
if Rs1 = Rs3 then g1=g3, else g2=g3
\|g1-g2\| / g2< 0.01
no
yes
end

FIG. 2. Computational flow chart.

TABLE II. Effect of changing Δt on the tolerable acceleration g_t.

Δt	ω	Λ	B_0	g_t
0.001 25	31.4	2.6	0.002	0.255
0.0005	31.4	2.6	0.002	0.256

C. Optimal searching scheme

In order to define the sensitivity limits for the liquid zone shape an optimal searching scheme was used to delineate the boundary between the regions in parameter space for which solutions either do or do not satisfy our sensitivity criterion. The scheme is described in the flow chart shown in Fig. 2. Eight to ten calculations were typically needed to obtain each point on the sensitivity curves.

D. Accuracy of the numerical scheme

An investigation into the accuracy of the results revealed that the number of time steps per period of the disturbance should be at least 160. Increasing the number of steps to 400 per period did not, however, result in any significant change in our results even at high frequencies (see Table II).

The spatial accuracy also proved to be an important consideration. Results obtained using the MacDonald–Briley scheme required 97 spatial points.

In order to test the adequacy of the 1-D model we compared results from 1-D calculations to results obtained by Sanz[16] for breaking times of an inviscid liquid bridge subject to an initial deformation of the surface area S given by

$$S(z,0) = 1 + \epsilon(\epsilon - 2)\sin(\pi z/\Lambda), \quad Q(z,0) = 0.$$

The results of the comparison are given in Table III. Our calculations are in reasonable agreement with those of Sanz. Table IV lists a comparison between our results for the first eigenfrequency, those predicted by the linearized analysis of Meseguer,[11] and experimentally obtained values.[11] Our calculated values lie between the linearized results and the experimentally obtained values. Finally, we note that the analysis of Langbein,[12] employs an expression for a damped linear oscillator together with natural frequencies of infinite liquid columns obtained by Bauer[22] and will overestimate the natural frequencies of finite bridges. This has been well documented by Sanz[16] in a thorough comparison of various methods used to simulate liquid bridge phenomenon.

TABLE III. Comparison of breaking times (T_b) and partial breaking volume (V_b) with those of Sanz[16] (T_b^*, V_b^*). Here Λ is the slenderness, ϵ is the initial perturbation amplitude, and Δz is the spatial step size used in our calculations.

Λ	ϵ	Δz	T_b	T_b^*	V_b	V_b^*
3.07	0.2	0.128	21.02	21.98	0.8525	0.8554
3.14	0.2	0.130	13.71	13.62	0.8474	0.8574
3.20	0.2	0.134	11.82	11.52	0.8427	0.8442
3.10	0.3	0.129	7.97	8.4	0.8525	0.8539
3.10	0.4	0.129	4.41	4.84	0.859 45	0.8566

TABLE IV. Comparison of the dimensionless first eigenfrequency ω_0 computed using our method, the linearized method of Meseguer[11] (ω_0^*), and experimental results[11] (ω_{0e}).

Λ	ω_0	ω_0^*	ω_{0e}
2.571	0.312	0.348	0.30
2.714	0.248	0.259	0.23
2.854	0.174	0.222	0.19

IV. RESULTS AND DISCUSSION

The calculations were undertaken for a disk radius of 0.0175 m and liquids with the following physical properties; $\rho = 920\ \mathrm{kg\ m^{-3}}$, $\gamma = 0.02\ \mathrm{N\ m^{-1}}$, and kinematic viscosities in the range 6×10^{-7}–$6\times10^{-5}\ \mathrm{m^2\ sec^{-1}}$. These viscosities cover a range of typical experimental materials (water, silicone oils, etc., used in experiments[10]). The sensitivity criteria chosen to characterize the response of the bridge represent two extremes. The first is the deviation of the the bridge shape by more than 5% from its equilibrium radius, the second is breakage of the bridge. The effects of viscosity, background steady acceleration (static Bond number, B_0), and slenderness (Λ) were examined and the results are presented below. Each point on these curves was obtained after running the calculation for times corresponding to more than ten periods of the driving force.

Figures 3 and 4 show the effect of viscosity on the tolerable acceleration, g_t, for a frequency of 5 Hz at fixed Λ and B_0, for both sensitivity criteria. The tolerance increases as the viscosity is increased. Notice, however, that for values of the dimensionless viscosity parameter C less than 10^{-1} the

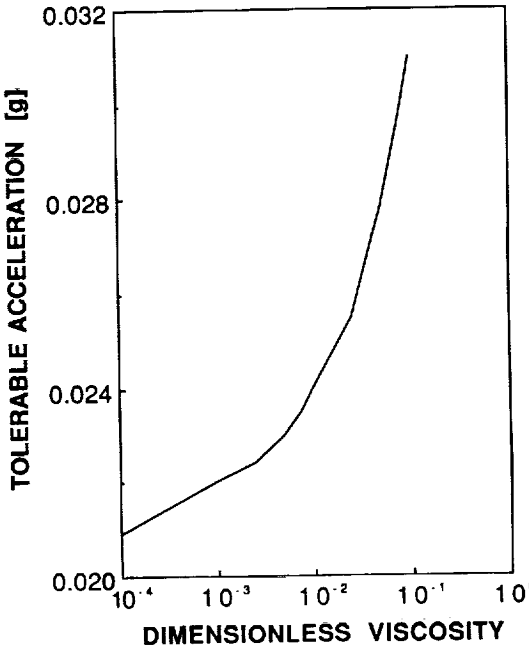

FIG. 3. Dimensionless viscosity parameter C versus tolerable acceleration for breakage of the bridge at $f = 5$ Hz, $\Lambda = 2.6$, $B_0 = 0.002$, and $g_0 = 1.42\times10^{-5}g$.

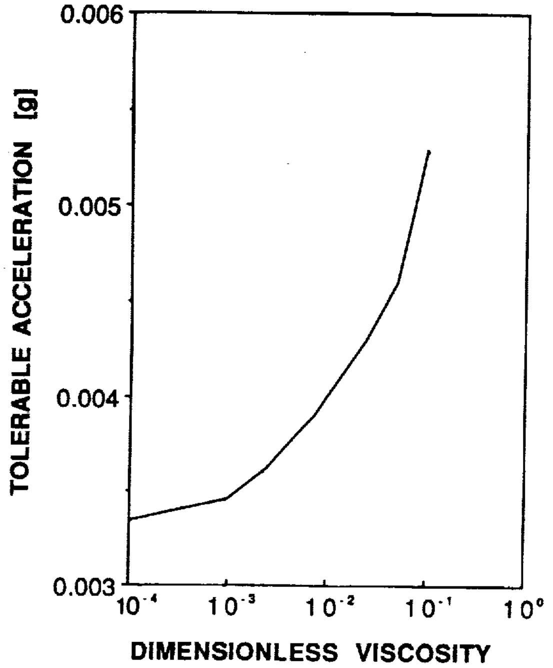

FIG. 4. Effect of viscosity on tolerable acceleration for the shape change criterion at $f = 5$ Hz, $\Lambda = 2.6$, $B_0 = 0.002$, and $g_0 = 1.42\times 10^{-5} g$.

increase in tolerance is slight even though the viscosity has been increased by two orders of magnitude. Only when C approaches 10^{-1} does the increase in tolerance become significant. Figures 5 and 6 further illustrate this point. The 5 Hz residual accelerations greater than 0.03 g would not normally be expected to occur in spacecraft laboratories so we have not examined cases with $C > 0.1$.

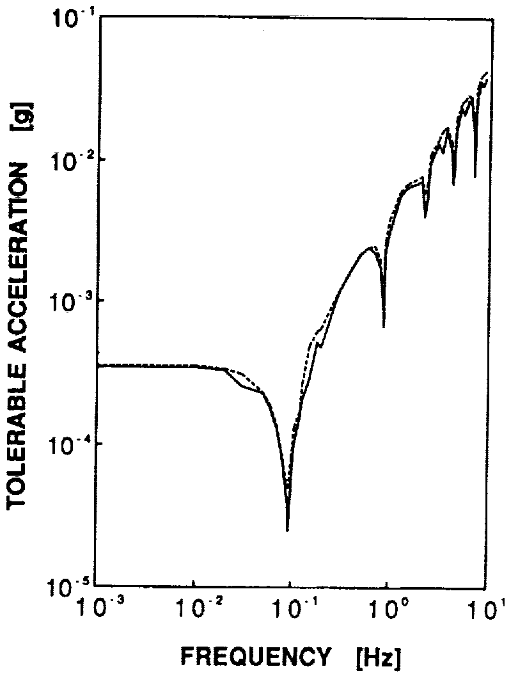

FIG. 5. Curves of tolerable acceleration versus frequency for breakage of the bridge at $B_0 = 0.002$, $g_0 = 1.42\times 10^{-5} g$, and $\Lambda = 2.6$. The solid curve and the dashed curve are the results for $C = 0.001$ and 0.01, respectively.

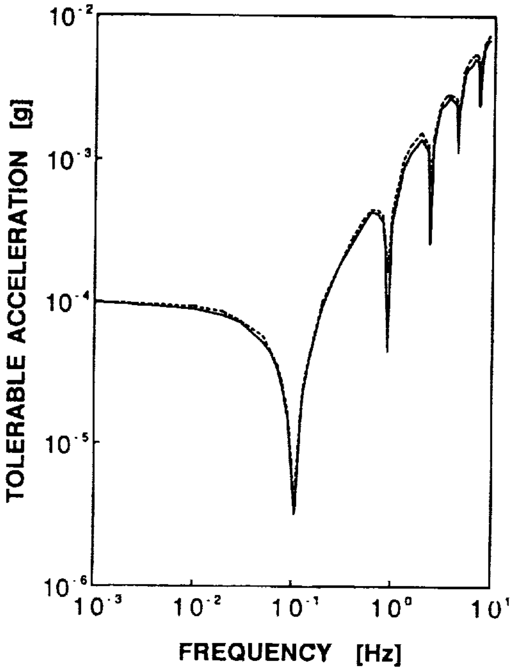

FIG. 6. Curves of tolerable acceleration versus frequency for shape change criterion at $B_0 = 0.002$, $g_0 = 1.42\times 10^{-5} g$, and $\Lambda = 2.6$. The solid curve and the dashed curve are the results for $C = 0.001$ and 0.01, respectively.

The value of the static Bond number has a more pronounced effect on sensitivity as seen in Figs. 7 and 8. This is limited, however, to the lower frequency range. With increasing frequency the differences are less pronounced. This is particularly so for the shape change criterion. It is interest-

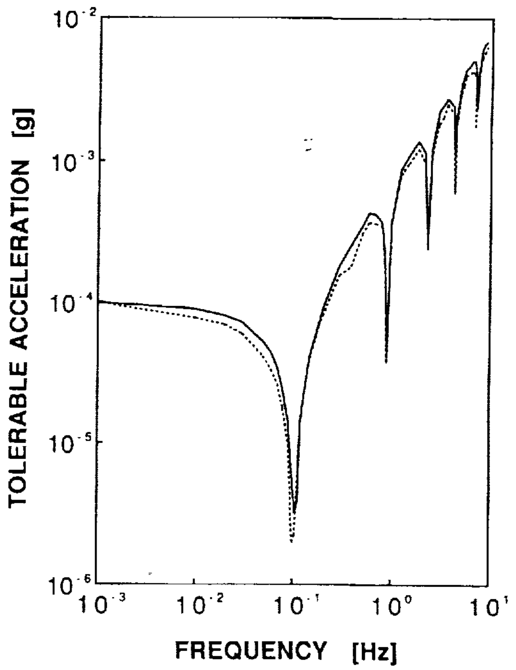

FIG. 7. Curves of tolerable acceleration versus frequency for shape change criterion at $\Lambda = 2.6$ and $C = 0.001$. The solid curve and the dashed curve are the results for $B_0 = 0.002$ ($g_0 = 1.42\times 10^{-5}$ g) and $B_0 = 0.02$ ($g_0 = 1.42\times 10^{-4} g$), respectively.

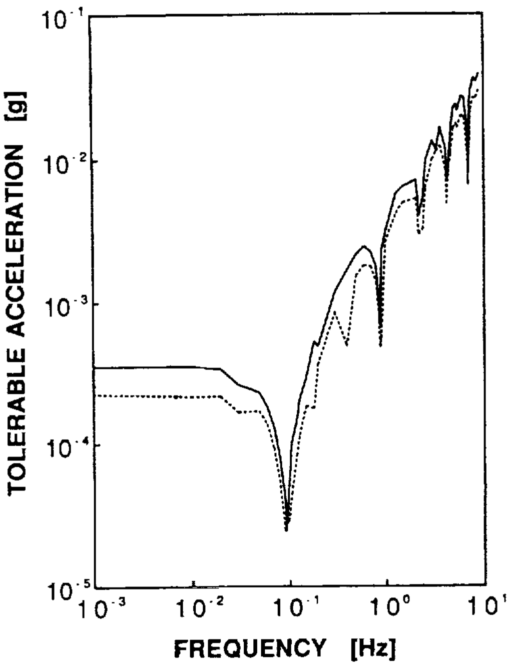

FIG. 8. Curves of tolerable acceleration versus frequency for breakage of the bridge at $\Lambda = 2.6$ and $C = 0.001$. The solid curve and the dashed curve are the results for $B_0 = 0.002$ ($g_0 = 1.42\times10^{-5}$ g) and $B_0 = 0.02$ ($g_0 = 1.42\times10^{-4}\,g$), respectively.

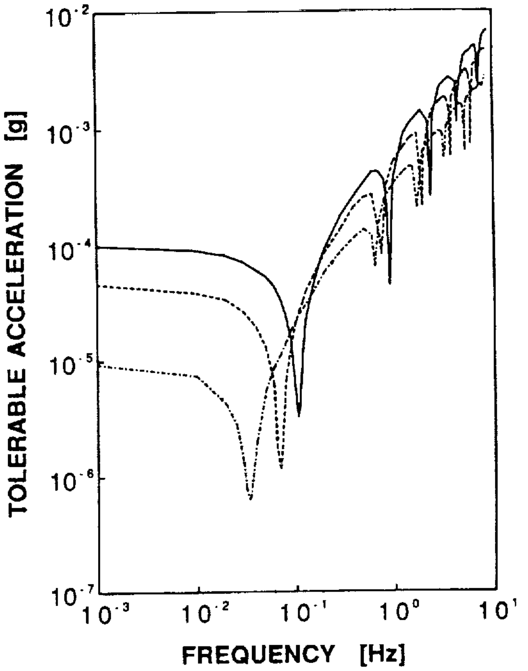

FIG. 10. Curves of tolerable acceleration versus frequency for the shape change criterion at $B_0 = 0.002, g_0 = 1.42\times10^{-5}\,g$, and $C = 0.001$. The solid curve, the dotted curve, and the dot-dashed curve are the results for $\Lambda = 2.6$, 2.826, and 3.024, respectively.

ing to note the additional deviations from the general trend for the case of zone breakage between 10^{-1} and 1 Hz.

A small decrease in the slenderness Λ changes the magnitude of tolerable acceleration markedly when Λ is close to $\Lambda_{\max}$. This is illustrated in Figs. 9 and 10. The change in tolerable acceleration magnitude becomes less significant for values of Λ less than 80% of the critical value.

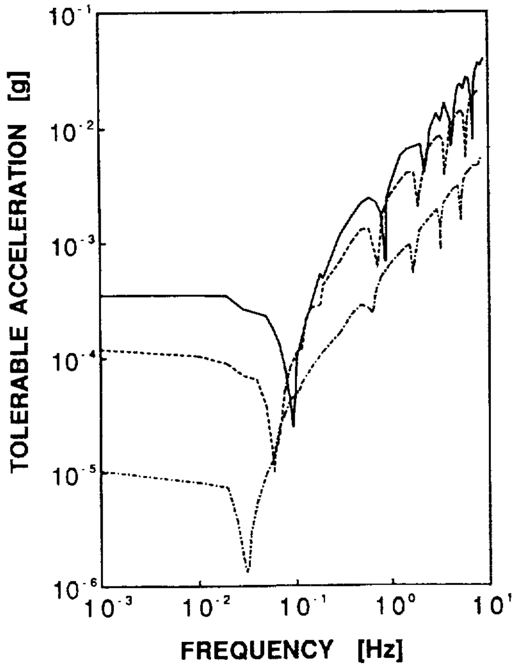

FIG. 9. Curves of tolerable acceleration versus frequency for breakage of the bridge at $B_0 = 0.002, g_0 = .42\times10^{-5}\,g$, and $C = 0.001$. The solid curve, the dotted curve, and the dot-dashed curve are the results for $\Lambda = 2.6$, 2.826, and 3.024, respectively.

Of most practical interest is the sensitivity of a given zone (i.e., Λ, B_0, and C fixed) as a function of the frequency of the disturbance. This is shown in Figs. 5–10. For both criteria the general trend is an increase in tolerable residual gravity with increasing frequency. At the eigenfrequencies of the zone there are, however, dramatic deviations from this trend. Here the liquid zone is extremely sensitive in comparison to both higher and lower frequencies. The tolerable residual gravity level can be two orders of magnitude lower at this frequency. For the values of Λ and B_0 (g_0) considered these frequencies are found in the neighborhood of 10^{-1} Hz. Associated maximum tolerable residual gravity levels as low as 10^{-3} to $10^{-6}\,g$ have been calculated. In addition, at frequencies higher than the most sensitive one there are less dramatic deviations from the general trend. The frequencies at which these deviations occur are the eigenfrequencies for

TABLE V. Most sensitive frequencies and associated tolerable acceleration (Hz) calculated using the 1-D (f_0, g_{tol}) model and Langbein's (f_0^*, g_{tol}^*) linear oscillator model.[12] For the 1-D model $B_0 = 0.002$ in all cases. Langbein's model is independent of B_0.

Λ	f_0 (Hz)	f_0^* (Hz)	g_{tol} (g)	g_{tol}^* (g)	ν(m^2 sec^{-1})
3.024	0.0334	0.0663	6.32×10^{-7}	1.11×10^{-9}	5×10^{-7}
2.826	0.0070	0.1224	1.16×10^{-6}	2.18×10^{-9}	5×10^{-7}
2.6	0.1049	0.1857	3.26×10^{-6}	3.6×10^{-9}	5×10^{-7}
2.6	0.1049	0.1857	3.53×10^{-6}	3.6×10^{-8}	5×10^{-6}

TABLE VI. Tolerable acceleration (g_t) and associated eigenfrequencies (ω^*) for two of the cases (shape change criterion).

$\Lambda = 3.024$, $B_0 = 0.002$, $C = 0$					
ω^*	0.21	4.0	11.0	20.5	33.5
g_t (m sec^{-2})	6.0×10^{-6}	6.09×10^{-4}	1.88×10^{-3}	5.10×10^{-3}	5.06×10^{-3}
$\Lambda = 2.826$, $B_0 = 0.002$, $C = 0$					
ω^*	0.44	4.7	12.56	24	38.5
g_t (m sec^{-2})	1.09×10^{-5}	7.79×10^{-4}	1.96×10^{-3}	4.76×10^{-3}	5.78×10^{-3}

the zone. As the frequency of the forcing function approaches an eigenfrequency the zone becomes more sensitive. The lowest tolerable acceleration occurs in conjunction with the smallest eigenfrequency. We note that owing to our assumption that the top and bottom disks vibrate in phase, the eigenfrequencies locally exhibiting the most sensitive response are those associated with eigenmodes having an odd number of nodes (i.e., an even number of half waves). This is in agreement with the analysis of Mesegeuer.[11] It is interesting to compare our results with linear oscillator model of Langbein.[12] Table V gives a comparison between the linear oscillator model and our 1-D model. While the results are qualitatively similar there are three distinct differences. First, for the case considered the linear oscillator model overestimates the sensitivities by almost two orders of magnitude. Second, as mentioned previously, the eigenfrequencies predicted by our model are smaller. The third difference is that Langbein's model implicitly assumes that the axial vibration will excite deformations with a both odd and even number of nodes (this is precluded in our model). If the top and bottom disks do vibrate out of phase, then our results will underestimate the response of the liquid bridge at eigenfrequencies corresponding to eigenmodes with an even number of nodes.

Table VI lists the eigenfrequencies (which can be determined independently[11]) and the associated maximum tolerable acceleration, g_t, for selected inviscid cases. For the inviscid zones, we found that whenever the higher eigenfrequency is close to an integer multiple of a lower eigenfrequency the sensitivity of the zone to disturbances with the higher frequency is increased. This noticeable increase in sensitivity is caused by nonlinear interaction and excitation of the lower mode.

The spatial deformation of the liquid zone also varies as a function of the forcing frequency. Figures 11 and 12 illustrate the evolution of the zone shape as a function of time for selected cases. Note that, owing to the small value of B_0, for these cases the initial surface shape is visually indistinguish-

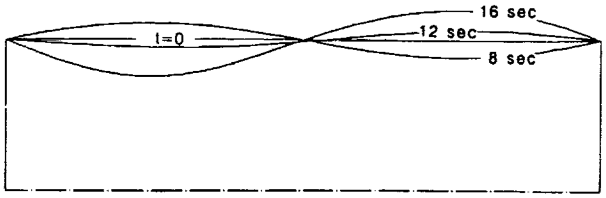

FIG. 11. Shape change as a function of time for a liquid zone with $\Lambda = 2.6$, $C = 0.001$, and $g(t) = 1 + (B_1/B_0)\sin(\omega t)$. The dimensional frequency, f, is 0.06 Hz, and $B_1/B_0 = 12$. For the physical properties considered, the maximum oscillating acceleration magnitude is $1.8\times 10^{-4}\,g$.

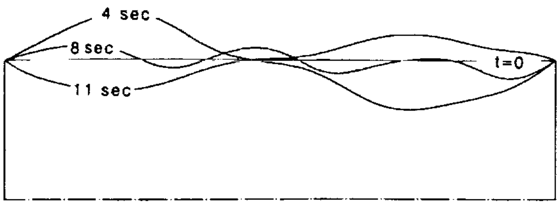

FIG. 12. Shape change as a function of time for a liquid zone with $\Lambda = 2.6$, $C = 0.001$, and $g(t) = 1 + (B_1/B_0)\sin(\omega t)$. The dimensional frequency, f, is 3 Hz, and $B_1/B_0 = 916$. For the physical properties considered, the maximum oscillating acceleration magnitude is $1.3\times 10^{-2}\,g$.

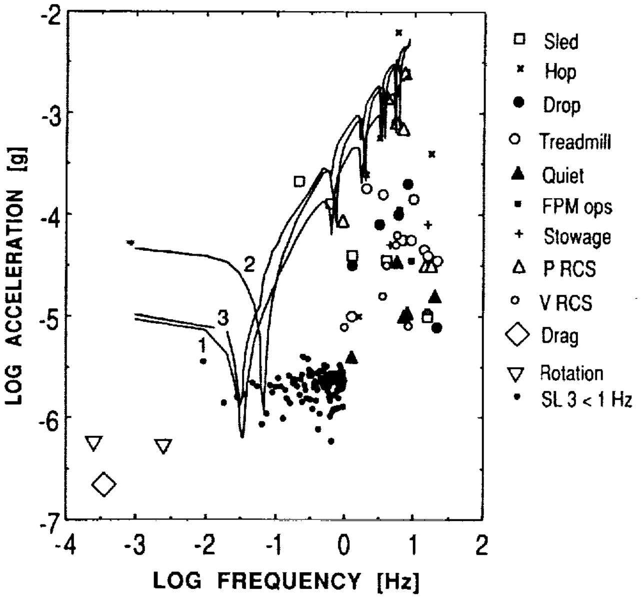

FIG. 13. Residual accelerations measured on orbit (in units of $g = 9.8$ m sec^{-2}) and selected sensitivity curves, Curves 1 and 2 correspond to $\Lambda = 2.826$ and 3.024 from Fig. 10. Curve 3 corresponds to $\Lambda = 3.024$ from Fig. 9. (Acceleration data courtesy of Dr. H. Hamacher, DLR, and M. J. B. Rogers, Univ. of Alabama in Huntsville.) The Spacelab 3 (SL-3) data are restricted to measured frequencies between 10^{-3} and 1 Hz. The points corresponding to Sled, Hop, Drop, Treadmill, Quiet, FPM ops (Fluid Physics Module operations), Stowage, refer to activities and experiments on the D-1 mission.[23] P RCS and V RCS refer to the primary and vernier thrusters. The drag and rotation entries correspond to accelerations arising from slow variations in atmospheric drag during an orbit and attitude changes involving rotation.

able from the surface of a right circular cylinder. While higher forcing frequencies are associated with more nodes, the shape of the zone is complicated by the excitations of the fundamental mode and by nonlinear interactions.

In summary, our results indicate that the zone is most sensitive to accelerations with frequencies close to or equal to the lowest natural frequency of the zone. It is useful to assess the sensitivity of the zone in terms of predicted space station and/or spacelab environments and with previous acceleration measurements. For the liquid zone cases examined we have seen that frequencies in the 10^{-2}–10^{-1} Hz range appear to be the most sensitive. Figure 13 shows sensitivity curves selected from Figs. 9 and 10 together with acceleration as a function of frequency taken data recorded on orbit. The amplitudes of low-frequency ($< 10^{-2}$ Hz) accelerations predicted for the space station should not exceed levels of $10^{-6}\,g$.[23] Higher frequencies can be associated with acceleration magnitudes of up to $10^{-2}\,g$.[24] In terms of these predicted levels, or those measured on past missions,[3,25] the practical sensitivity range is restricted to disturbances with frequencies in the range 10^{-2}–10^{-1} Hz and 1–10 Hz.

ACKNOWLEDGMENTS

The authors would like to thank Dr. Franz Rosenberger and Jalil Ouazzani for helpful discussion.

This work was performed under National Aeronautical and Space Administration Grant No. NAG8-724, in relation to the Vibration Isolation Advanced Technology Development project.

[1] J. I. D. Alexander and C. A. Lundquist, AIAA J. **26**, 193 (1988).

[2] J. I. D. Alexander and C. A. Lundquist, J. Astron. Sci. **35**, 193 (1987).

[3] H. Hamacher, R. Jilg, and U. Mehrbold, *Proceedings of the 6th European Symposium Materials Sciences in Microgravity Conditions*, Bordeaux, France, 1986, ESA SP-256 (ESA Publications Division, Noordwijk, 1987), p. 413.

[4] I. Martinez, J. M. Haynes, and D. Langbein, in *Fluid Sciences and Materials Science in Space, A European Perspective*, edited by H. U. Walter (Springer, Berlin, 1987), p. 53.

[5] I. Martinez, *Proceedings of the 5th European Symposium on Materials Sciences under Microgravity*, Schloss, Elmau, Federal Republic of Germany, 1984, ESA SP-222 (ESA Scientific and Technical Publications, Noordwijk, 1984), p. 31.

[6] J. Haynes, in Ref. 5, p. 43.

[7] I. Martinez, in Ref. 3, p. 235.

[8] J. F. Padday, in Ref. 3, p. 251.

[9] Oscillation of a molten liquid zone in low gravity, videotaped from NASA's STS-32 mission, courtesy A. Chait, NASA Lewis Research Center, 1990.

[10] J. Meseguer, J. Fluid Mech. **130**, 123 (1983).

[11] J. Meseguer, Appl. Microgravity Technol. **1**, 136 (1988).

[12] D. Langbein, in Ref. 3, p. 221

[13] H. C. Lee, IBM J. Res. Dev. **18**, 364 (1974).

[14] D. Rivas and J. Meseguer, J. Fluid Mech. **138**, 417 (1984).

[15] J. Meseguer and A. Sanz, J. Fluid Mech. **153**, 83 (1985).

[16] A. Sanz, J. Fluid Mech. **156**, 101 (1985).

[17] J. Meseguer, J. Cryst. Growth **73**, 599 (1985).

[18] J. Meseguer, A. Sanz, and J. Lopez, J. Cryst. Growth **78**, 325 (1986).

[19] R. Peyret and T. D. Taylor, *Computational Methods for Fluid Flow* (Springer, New York, 1983).

[20] W. R. Briley and H. McDonald, United Aircraft Research Laboratory Report No. M911363-6, 1973.

[21] W. R. Briley and H. McDonald, J. Comput. Phys. **24**, 372 (1977).

[22] H. F. Bauer, Z. Angew. Math. Mech. **64**, 475 (1984)

[23] H. Hamacher, R. Jilg, and U. Merbold, *Proceedings of the Nordeney Symposium on the Results of the German Spacelab Mission D-1*, Nordeney, Germany (DFVLR, Köln, 1987), p. 48.

[24] J. Sullivan (private communication, 1989).

[25] M. R. B. Rogers and J. I. D. Alexander, submitted to J. Spacecr. Rockets (1990).

Appendix 4

N15

INTERNATIONAL JOURNAL FOR NUMERICAL METHODS IN FLUIDS, VOL. 13, 000–000 (1991)

SURFACE TENSION AND BUOYANCY-DRIVEN FLOW IN A NON-ISOTHERMAL LIQUID BRIDGE

YIQIANG ZHANG AND J. IWAN D. ALEXANDER

Center for Microgravity and Materials Research, University of Alabama in Huntsville, Huntsville, AL 35899, U.S.A.

SUMMARY

The Navier–Stokes–Boussinesq equations governing the transport of momentum, mass and heat in a non-isothermal liquid bridge with a temperature-dependent surface tension are solved using a vorticity–stream-function formulation together with a non-orthogonal co-ordinate transformation. The equations are discretized using a pseudo-unsteady semi-implicit finite difference scheme and are solved by the ADI method. A Picard-type iteration is adopted which consists of inner and outer iterative processes. The outer iteration is used to update the shape of the free surface. Two schemes have been used for the outer iteration; both use the force balance normal to the free surface as the distinguished boundary condition. The first scheme involves successive approximation by the direct solution of the distinguished boundary condition. The second scheme uses the artificial force imbalance between the fluid pressure, viscous and capillary forces at the free surface which arises when the boundary condition for force balance normal to the surface is not satisfied. This artificial imbalance is then used to change the surface shape until the distinguished boundary condition is satisfied. These schemes have been used to examine a variety of model liquid bridge situations including purely thermocapillary-driven flow situations and mixed thermocapillary- and bouyancy-driven flow.

KEY WORDS Thermocapillary flow, buoyancy, free surface, finite difference, Picard iteration, ADI.

1. INTRODUCTION

The computation of solutions to the steady free boundary problem of mixed thermocapillary- and buoyancy-driven convection in a non-isothermal cylindrical liquid bridge is complicated by the strongly non-linear boundary conditions at the unknown free surface. Most studies to date have avoided the computation of the free surface shape and assumed that the liquid surface is a circular cylinder[1–6] or have imposed a non-circular cylindrical surface shape.[7] These models have involved either half-zone configurations (where the liquid bridge is held between rigid disks of different temperature) or full zones (where the liquid bridge is held between two solids of equal temperature). The full zone models are motivated by the floating zone crystal growth process.[8] Recently, Duranceau and Brown[9] have approached the full zone crystal growth problem using the finite element method and have computed the shape of the liquid surface as well as the melt–crystal and melt–feed rod surfaces together with interacting thermocapillary and buoyant convective flow. Lan and Kou[10] have also approached the full zone problem using a finite volume method but restricted their calculations to the zero-gravity case for which the surface deformation from the circular cylindrical shape is minimal and buoyancy-driven flow is absent. Hyer *et al.*[11] have used a finite element method, which is well suited to irregular geometries, to compute

0271-2091/91/000000–00$05.00
© 1991 by John Wiley & Sons, Ltd.

Received October 1990
Revised April 1991

PRECEDING PAGE BLANK NOT FILMED

interacting thermocapillary and buoyant convective flow in full and half-zone configurations bu did not consider solidification.

Recently, finite difference methods have been used to solve problems with free and movin boundary geometries using various mapping techniques.[12] These methods are also applicable tc the free boundary problem associated with liquid bridges and floating zones. Kang and Leal[1 used the finite difference method with orthogonal boundary-fitted co-ordinates to study th deformation of a bubble. The boundary-fitted mapping scheme requires the solution of a couplec set of Laplace equations to determine the new grid to be generated at each outer iteration.

In the present investigation the governing equations are recast in terms of a vorticity–stream function formulation together with a non-orthogonal co-ordinate transformation. The latte allows an irregular free boundary to coincide with a co-ordinate line (or surface) without the neec to solve a coupled set of Laplace equations. The resulting equations are discretized usin a pseudo-unsteady semi-implicit difference scheme and solved by the ADI method. The combina tion of the above methods provides a reasonably accurate and economical solution procedure Four boundary conditions are specified at the free surface: the kinematic boundary condition, th balance of energy across the surface and the balance of force normal and tangent to the surface The energy balance, tangential force balance and kinematic conditions at the free surface ar solved together with the Navier–Stokes and continuity equations, while the normal force balanc condition is distinguished[14] to determine the free surface shape. In addition, an 'outer' iterativ procedure is needed to locate the free surface. In this paper two outer iterative schemes ar reported. The first scheme involves successive approximation by the direct solution of the forc balance normal to the free surface. The second scheme, after Ryskin and Leal,[15] uses the forc imbalance between the fluid pressure, viscous and capillary forces at the free surface which arise when the boundary condition for force balance normal to the surface is not satisfied. Thi artificial imbalance is used to drive the surface shape towards its equilibrium position (i.e. unt the force balance condition is satisfied). These schemes are used to examine a variety of mode liquid bridge situations including purely thermocapillary-driven flow situations and mixe buoyancy–thermocapillary-driven flow.

[It looks as if the period has been omitted ?]

2. FORMULATION OF THE PROBLEM

2.1. *Governing equations*

Consider a cylindrical liquid bridge (see Figure 1) held between two parallel coaxial circula rigid disks of radius R_0 separated by a distance L. The liquid is a non-isothermal incompressibl Newtonian fluid. The bridge is held between the disks by surface tension. The free surface of th bridge is a gas–liquid surface and the steady surface shape is described by $r = R(z)$. Each disk maintained at a constant temperature T_0. Surface heating is provided through an ambie temperature $T_\infty(z)$. Radiative and convective heat transfer at the free surface are accounted for b a heat transfer coefficient h. In addition, we assume that the gravitational acceleration is paralle to the cylinder axis and the velocity, ~~and that the~~ temperature field and the deformation of the fre surface are axisymmetric. Furthermore, we let the surface tension at the free surface vary linearl with temperature and assume that the Boussinesq approximation holds.

math

The governing equations are made dimensionless by scaling length, time and velocity with R, R_0/U^* and U^* respectively. Here U^* is a characteristic velocity given by

$$U^* = \frac{|\gamma|\Delta T}{\mu},$$

ORIGINAL PAGE IS
OF POOR QUALITY

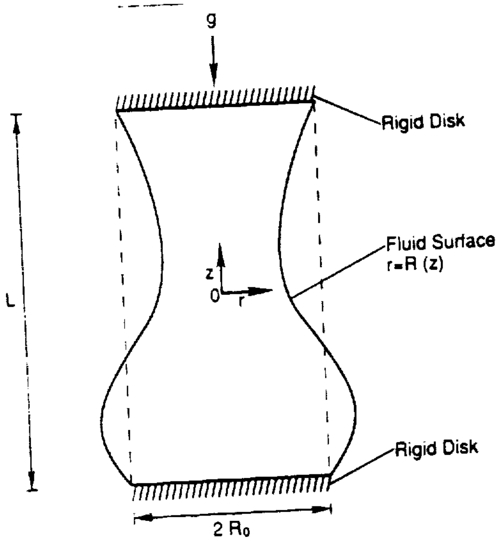

Figure 1. Liquid bridge model

where $\Delta T = T_{\max} - T_{\min}$ represents the maximum temperature difference at the surface, $|\gamma|$ is the absolute value of the derivative of the surface tension with respect to temperature and μ is the dynamic viscosity.

We shall refer to a 'half-zone' model when the end disks are held at the maximum and minimum temperatures respectively and a 'full zone' when the temperature maximum occurs between the disks. For a full zone we shall take the ambient temperature $T_\infty(z)$ to be parabolic and take $T_{\max}$ to be $T_\infty(0)$ and $T_{\min}$ to be $T(\pm\Lambda/2)$, where $\Lambda = L/R_0$ is the aspect ratio.

The non-dimensional pressure is

$$p = \frac{p^* + \rho_0 g z}{\rho_0 U^{*2}} R_0,$$

where p^* is the dimensional pressure, g is the gravitational acceleration, z is the dimensionless axial co-ordinate and ρ_0 is the density corresponding to the reference temperature. The temperature is rendered dimensionless using $T_{\max} - T_{\min}$. With these scales the dimensionless steady state equations in a cylindrical co-ordinate system can be written as

$$\frac{1}{r}\frac{\partial(ru)}{\partial r} + \frac{\partial w}{\partial z} = 0, \tag{1}$$

$$u\frac{\partial u}{\partial r} + w\frac{\partial u}{\partial z} = -\frac{\partial p}{\partial r} + \frac{1}{Re}\left(\frac{\partial^2 u}{\partial r^2} + \frac{1}{r}\frac{\partial u}{\partial r} + \frac{\partial^2 u}{\partial z^2} - \frac{u}{r^2}\right), \tag{2}$$

$$u\frac{\partial u}{\partial r} + w\frac{\partial w}{\partial z} = -\frac{\partial p}{\partial z} + \frac{1}{Re}\left(\frac{\partial^2 w}{\partial r^2} + \frac{1}{r}\frac{\partial w}{\partial r} + \frac{\partial^2 w}{\partial z^2}\right) + \frac{Gr}{Re^2} T, \tag{3}$$

$$u\frac{\partial T}{\partial r} + w\frac{\partial T}{\partial z} = \frac{1}{Ma}\left(\frac{\partial^2 T}{\partial r^2} + \frac{1}{r}\frac{\partial T}{\partial r} + \frac{\partial T}{\partial z^2}\right), \tag{4}$$

$\partial^2 T$

"insert superscript 2"

where the Reynolds number Re, Marangoni number Ma and Grashof number Gr are respectively

$$Re=\frac{R_0U^*}{\nu}, \qquad Ma=\frac{|\gamma|\Delta TR_0}{\mu\kappa}, \qquad Gr=\frac{g\beta\Delta TR_0^3}{\nu^2}.$$

Here ν is the kinematic viscosity, κ is the thermal diffusivity, β is the volumetric thermal expansion coefficient and g is the gravitational acceleration.

2.2. *Boundary conditions*

At the disks the boundary conditions are

$$u=w=T=0 \quad \text{at } z=\pm\Lambda/2, \tag{5}$$

and the symmetry conditions at the centreline $r=0$ are

$$u=\frac{\partial w}{\partial r}=\frac{\partial T}{\partial r}=0. \tag{6}$$

The boundary conditions at the free surface $r=R(z)$ take the form

$$\begin{aligned} p-Gz+\lambda=&\frac{2Re^{-1}}{1+(\partial R/\partial z)^2}\left[\frac{\partial u}{\partial r}+\left(\frac{\partial R}{\partial z}\right)^2\frac{\partial w}{\partial z}-\frac{\partial R}{\partial z}\left(\frac{\partial w}{\partial r}+\frac{\partial u}{\partial z}\right)\right]\\ &+\frac{Re^{-1}(C_0^{-1}-T)}{[1+(\partial R/\partial z)^2]^{3/2}}\left(\frac{1+(\partial R/\partial z)^2}{R}-\frac{\partial^2 R}{\partial z^2}\right), \end{aligned} \tag{7}$$

$$\left[1-\left(\frac{\partial R}{\partial z}\right)^2\right]\left(\frac{\partial u}{\partial z}+\frac{\partial w}{\partial r}\right)+2\frac{\partial R}{\partial z}\left(\frac{\partial u}{\partial r}-\frac{\partial w}{\partial z}\right)=-\left[1+\left(\frac{\partial R}{\partial z}\right)^2\right]^{1/2}\left(\frac{\partial T}{\partial z}+\frac{\partial R}{\partial z}\frac{\partial T}{\partial r}\right), \tag{8}$$

$$u+w\frac{\partial R}{\partial z}=0, \tag{9}$$

$$\frac{1}{(1+(\partial R/\partial z)^2)^{1/2}}\left(\frac{\partial T}{\partial r}-\frac{\partial R}{\partial z}\frac{\partial T}{\partial z}\right)+Bi(T-T_\infty)=0, \tag{10}$$

where

$$C_0=\frac{\gamma\Delta T}{\gamma_0}, \qquad Bi=\frac{hR_0}{\kappa}, \qquad G=\frac{gR_0}{U^{*2}}$$

are the capillary number, Biot number and dimensionless gravitational acceleration respectively and γ_0 is the mean surface tension. The force balances at the free surface in the normal and tangential directions are given by equations (7) and (8) respectively. Equation (9) is the kinematic boundary condition at the liquid–gas surface. The thermal boundary condition at the surface is given by equation (10) with the ~~equivalent~~ heat transfer coefficient Bi. The constant λ on the left-hand side of (7) represents a dimensionless reference pressure difference[9] across the surface. In liquid bridge model systems with fixed rigid disks such as the one discussed here, λ is determined by the constant volume constraint

$$V_0=\int_{-\Lambda/2}^{\Lambda/2}\pi R^2(z)\mathrm{d}z\equiv\text{constant}. \tag{11}$$

dimensionless

Finally, the condition that the contact lines between the liquid end disks are fixed is

$$R = 1 \quad \text{at } z = \pm\Lambda/2. \tag{12}$$

3. NUMERICAL METHOD

For the case of a two-dimensional axisymmetric flow the governing equations can be simplified by introducing the streamfunction ψ and vorticity ω as new dependent variables:

$$u = \frac{1}{r}\frac{\partial\psi}{\partial z}, \qquad w = \frac{-1}{r}\frac{\partial\psi}{\partial r}, \tag{13}$$

$$\omega = \frac{\partial u}{\partial z} - \frac{\partial w}{\partial r}. \tag{14}$$

From (13), (14), (2) and (3) one obtains for ω

$$u\frac{\partial\omega}{\partial r} + w\frac{\partial\omega}{\partial z} - \frac{\omega u}{r} = \frac{1}{Re}\left(\frac{\partial^2\omega}{\partial r^2} + \frac{1}{r}\frac{\partial\omega}{\partial r} + \frac{\partial^2\omega}{\partial z^2}\right) - \frac{1}{Re}\frac{\omega}{r^2} - \frac{Gr}{Re^2}\frac{\partial T}{\partial r}. \tag{15}$$

Substitution of (13) into (14) yields

$$r\omega = \frac{\partial^2\psi}{\partial r^2} - \frac{1}{r}\frac{\partial\psi}{\partial r} + \frac{\partial^2\psi}{\partial z^2}. \tag{16}$$

The original set of three equations governing mass and momentum has thus been reduced to two equations governing the streamfunction and vorticity.

The steady free boundary problem for a cylindrical liquid bridge is solved iteratively, since the location of the free surface is *a priori* unknown. To obtain a solution, we adopt a Picard iterative procedure[12] as follows.

1. Guess the free surface shape for the initial iterate.
2. Obtain the approximate temperature and velocity fields by transforming the governing equations and boundary conditions to a circular cylindrical domain via a non-orthogonal transformation and solve them using a pseudo-unsteady semi-implicit method.
3. Obtain the pressure at the free surface by integrating the transformed momentum equation.
4. Use the normal force balance condition at the free surface to decide how to update the free surface location.
5. Return to step 2. Repeat until convergence is obtained by satisfing all equations and boundary conditions to a specified degree of accuracy.

The details of this numerical procedure are discussed below.

3.1. *Non-orthogonal transformation*

At each outer iteration the region occupied by the liquid bridge is transformed into a fixed rectangular computational region using a non-orthogonal co-ordinate transformation, i.e.

$$\eta = z, \qquad \xi = \frac{r}{R(z,\tau)}. \tag{17}$$

For each iteration time τ this transforms the domain

$$-\Lambda/2 < z < \Lambda/2, \qquad 0 < r < R(z,\tau)$$

onto the rectangle

$$-\Lambda/2<z<\Lambda/2, \qquad 0<\xi<1.$$

It then follows that

$$\frac{\partial}{\partial r}\rightarrow\frac{1}{R}\frac{\partial}{\partial\zeta}, \qquad \frac{\partial}{\partial z}\rightarrow\frac{\partial}{\partial\eta}-\frac{\zeta}{R}\frac{\partial R}{\partial\eta}\frac{\partial}{\partial\zeta}. \tag{18}$$

The advantage of this transformation is that the free boundary coincides exactly with a coordinate line in a computational grid and regeneration of mesh during the outer iteration is avoided. The transformed governing equations now take the form

$$\frac{1}{R^2\zeta}\left(\frac{\partial\psi}{\partial\eta}\frac{\partial\omega}{\partial\zeta}-\frac{\partial\psi}{\partial\zeta}\frac{\partial\omega}{\partial\eta}\right)-\frac{u\omega}{R\zeta}=\frac{1}{Re}\left(\frac{\partial^2\omega}{\partial\eta^2}+A\frac{\partial^2\omega}{\partial\zeta^2}+B\frac{\partial\omega}{\partial\zeta}+C\frac{\partial^2\omega}{\partial\eta\partial\zeta}\right)-\frac{1}{Re}\frac{\omega}{R^2\zeta^2}-\frac{G_r}{Re^2}\frac{1}{R}\frac{\partial T}{\partial\zeta}. \tag{19}$$

$$\frac{1}{R^2\zeta}\left(\frac{\partial\psi}{\partial\eta}\frac{\partial T}{\partial\zeta}-\frac{\partial\psi}{\partial\zeta}\frac{\partial T}{\partial\eta}\right)=\frac{1}{Ma}\left(\frac{\partial^2 T}{\partial\eta^2}+A\frac{\partial^2 T}{\partial\zeta^2}+B\frac{\partial T}{\partial\zeta}+C\frac{\partial^2 T}{\partial\eta\partial\zeta}\right), \tag{20}$$

$$\frac{\partial^2\psi}{\partial\eta^2}+A\frac{\partial^2\psi}{\partial\zeta^2}+B^*\frac{\partial\psi}{\partial\zeta}+C\frac{\partial^2\psi}{\partial\eta\partial\zeta}=R\zeta\omega, \tag{21}$$

where

$$A=\left(\frac{\zeta}{R}\frac{\partial R}{\partial\eta}\right)^2+\frac{1}{R^2},$$

$$B=\left[2\left(\frac{1}{R}\frac{\partial R}{\partial\eta}\right)^2-\frac{1}{R}\frac{\partial^2 R}{\partial\eta^2}\right]\zeta+\frac{1}{R^2\zeta},$$

$$B^*=B-\frac{2}{R^2\zeta},$$

$$C=-\frac{2\zeta}{R}\frac{\partial R}{\partial\eta}.$$

The boundary and symmetry conditions (5)–(10) are now:

at $\eta=\pm\Lambda/2$,

$$\psi=0, \qquad \omega=\frac{1}{\zeta}\frac{\partial^2\psi}{\partial\eta^2}, \qquad T=0; \tag{22}$$

at $\zeta=0$,

$$\psi=0, \qquad \omega=0, \qquad \partial T/\partial\zeta=0; \tag{23}$$

at $\zeta=1$,

$$\psi=0, \tag{24}$$

$$\omega=\frac{1}{R}\left(\frac{\partial R}{\partial\eta}\right)^2\frac{\partial w}{\partial\zeta}-2\frac{\partial R}{\partial\eta}\frac{\partial w}{\partial\eta}+\left[2-\left(\frac{\partial R}{\partial\eta}\right)^2\right]\frac{\partial u}{\partial\eta}+\frac{1}{R}\left(\frac{\partial R}{\partial\eta}\right)^3\frac{\partial u}{\partial\zeta}+\left[1+\left(\frac{\partial R}{\partial\eta}\right)^2\right]^{1/2}\frac{\partial T}{\partial\eta}, \tag{25}$$

$$\frac{1}{(1+(\partial R/\partial\eta)^2)^{1/2}}\left[\frac{1}{R}\frac{\partial T}{\partial\zeta}-\frac{\partial R}{\partial\eta}\left(\frac{\partial T}{\partial\eta}-\frac{1}{R}\frac{\partial R}{\partial\eta}\frac{\partial T}{\partial\zeta}\right)\right]+B_i(T-T_\infty)=0, \tag{26}$$

$$p - G\eta + \lambda - \frac{2Re^{-1}}{1+((\partial R/\partial\eta)^2}\left[\frac{1}{R}\frac{\partial u}{\partial\zeta} + \left(\frac{\partial R}{\partial\eta}\right)^2\left(\frac{\partial w}{\partial\eta} - \frac{1}{R}\frac{\partial R}{\partial\eta}\frac{\partial w}{\partial\zeta}\right) - \frac{\partial R}{\partial\eta}\left(\frac{1}{R}\frac{\partial w}{\partial\zeta} + \frac{\partial u}{\partial\eta} - \frac{1}{R}\frac{\partial R}{\partial\eta}\frac{\partial u}{\partial\zeta}\right)\right]$$

$$= Re^{-1}(C_0^{-1} - T)\frac{1}{[1+(\partial R/\partial\eta)^2]^{3/2}}\left(\frac{1+(\partial R/\partial\eta)^2}{R} - \frac{\partial^2 R}{\partial\eta^2}\right). \tag{27}$$

Equations (24) and (25) are the kinematic condition for the surface (i.e. the condition that a point on the surface remain on the surface) and the balance of tangential forces respectively. The complete streamfunction, velocity and temperature fields can be determined for a given axisymmetric surface shape (e.g. starting with an initial guess) using only (19)–(26). Then, as long as the balance-of-force condition (27) is not well satisfied, the force balance residual provides a basis for determining an improved estimate of the free surface shape. This procedure continues until the convergence criteria (to be defined later) are satisfied.

3.2. *Solution method*

Various methods can be devised to obtain a steady solution of equations (~~25~~ 19)–(~~25~~ 26). For the sake of simplicity a pseudo-unsteady method in association with a semi-implicit time discretization is used.

We first consider the following system of equations:

$$\frac{\partial T}{\partial\tau} + \left(L_1 - \frac{1}{Ma}\nabla^2\right)T + S_1 = 0, \tag{28}$$

$$\frac{\partial\omega}{\partial\tau} + \left(L_2 - \frac{1}{Re}\nabla^2\right)\omega + S_2 = 0, \tag{29}$$

$$\frac{\partial\psi}{\partial\tau} - \nabla^{*2}\psi + S_3 = 0, \tag{30}$$

where

$$L_1 = \frac{1}{R^2\zeta}\left(\frac{\partial\psi}{\partial\eta}\frac{\partial}{\partial\zeta} - \frac{\partial\psi}{\partial\zeta}\frac{\partial}{\partial\eta}\right), \tag{31}$$

$$L_2 = \frac{1}{R^2\zeta}\left(\frac{\partial\psi}{\partial\eta}\frac{\partial}{\partial\zeta} - \frac{\partial\psi}{\partial\zeta}\frac{\partial}{\partial\eta}\right) - \frac{u}{R\zeta}, \tag{32}$$

$$\nabla^2 = \frac{\partial^2}{\partial\eta^2} + A\frac{\partial^2}{\partial\zeta^2} + \frac{B\partial}{\partial\zeta} \longrightarrow B\frac{\partial}{\partial\zeta} \tag{33}$$

$$\nabla^{*2} = \frac{\partial^2}{\partial\eta^2} + A\frac{\partial^2}{\partial\zeta^2} + \frac{B^*\partial}{\partial\zeta} \longrightarrow B^*\frac{\partial}{\partial\zeta} \tag{34}$$

$$S_1 = -\frac{1}{Ma}C\frac{\partial^2 T}{\partial\eta\partial\zeta}, \qquad S_2 = \frac{1}{Re}\left(\frac{\omega}{R^2\zeta} - C\frac{\partial^2\omega}{\partial\eta\partial\zeta}\right) + \frac{Gr}{Re^2}\frac{1}{R}\frac{\partial T}{\partial\zeta}, \tag{35}$$

$$S_3 = -C\frac{\partial^2\psi}{\partial\eta\partial\zeta} + R\zeta w. \tag{36}$$

We then proceed to solve this system as the (pseudo) time derivatives of T, ψ and $\omega \to 0$. For clarity we present the solution method only for the vorticity (ω) transport equation. The discretization in time employs an explicit Adams–Bashforth scheme for the non-linear convective terms and the implicit scheme for the viscous terms. Other terms in the equation are treated explicitly. For spatial discretization, central differences are used. The ADI form for the vorticity equation is then

$$\frac{2}{\Delta\tau}\left(\omega_{ij}^{n+1/2}-\omega_{ij}^{n}\right)+\tfrac{3}{2}(L_2\omega)_{ij}^{n}-\tfrac{1}{2}(L_2\omega)_{ij}^{n-1}-\frac{1}{Re}\left(\frac{\partial^2\omega}{\partial\eta^2}\right)_{ij}^{n}-\frac{1}{Re}\left(A\frac{\partial^2\omega}{\partial\zeta^2}+B\frac{\partial\omega}{\partial\zeta}\right)_{ij}^{n+1/2}+(S_2)_{ij}^{n}=0, \tag{37}$$

$$\frac{2}{\Delta\tau}(\omega_{ij}^{n+1}-\omega_{ij}^{n+1/2})+\tfrac{3}{2}(L_2\omega)_{ij}^{n}-\tfrac{1}{2}(L_2\omega)_{ij}^{n-1}-\frac{1}{Re}\left(\frac{\partial^2\omega}{\partial\eta^2}\right)_{ij}^{n+1}-\frac{1}{Re}\left(A\frac{\partial^2\omega}{\partial\zeta^2}+B\frac{\partial\omega}{\partial\zeta}\right)_{ij}^{n+1/2}+(S_2)_{ij}^{n}=0. \tag{38}$$

Here the superscript $n+1/2$ denotes the intermediate step associated with the ADI method.[16] The velocities of (25) (at the nth step) are taken from the values at the previous step. Thus, except for the thermal condition at the free boundary, these are Dirichlet boundary conditions. The heat transfer equation is also discretized in an ADI form. The resulting system of discretized equations is solved using a factorization method.[16]

We define a steady state to occur when the residuals ($\partial\omega/\partial\tau$, $\partial T/\partial\tau$, $\partial\psi/\partial\tau$) of the vorticity, energy and streamfunction equations are less than 10^{-7}, i.e.

$$\max\left|\frac{F_{ij}^{n+1}-F_{ij}^{n}}{\Delta\tau}\right|<10^{-7}. \tag{39}$$

Here F represents the vorticity, temperature or streamfunction, the subscript refers to the spatial location and the superscript refers to the iterative step. The numerical solution is second-order-accurate in space.

We have verified this solution method for steady 2D axisymmetric incompressible flow. Table I shows four examples of a comparison between the results of our code and a finite element code (FIDAP): two for buoyancy- and two for thermocapillary-driven flow. Figure 2 shows a comparison of the surface velocities using our method and the finite element method. One sees that the numerical method described here provides a reasonably accurate algorithm for computing steady 2D axisymmetric incompressible flows in rigid cavities and for mixed buoyancy- and surface-driven flows with free boundaries for the range of surface Reynolds numbers examined, $0<Re<21\,740$.

Having computed the vorticity and streamfunction for a given surface shape, it remains to iterate on the condition for the force balance normal to the surface in order to obtain the final steady surface shape. In addition, the shape must satisfy the volume constraint (11) and boundary conditions (12).

Table I. Comparison of finite difference method with results obtained using finite element code FIDAP

				This method		FIDAP	
Λ	Pr	Ra	Re	$W_{\max}$	$U_{\max}$	$W_{\max}$	$U_{\max}$
2	1	100	0	$1{\cdot}81\times10^{-1}$	$4{\cdot}27\times10^{-2}$	$1{\cdot}80\times10^{-1}$	$4{\cdot}28\times10^{-2}$
2	1	150	0	$2{\cdot}84\times10^{-1}$	$6{\cdot}64\times10^{-2}$	$2{\cdot}66\times10^{-1}$	$6{\cdot}64\times10^{-2}$
2	0·0127	0	3150	3·39	1·7	3·49	1·82
5·2	0·0127	0	5905	2·95	1·33	2·78	1·29

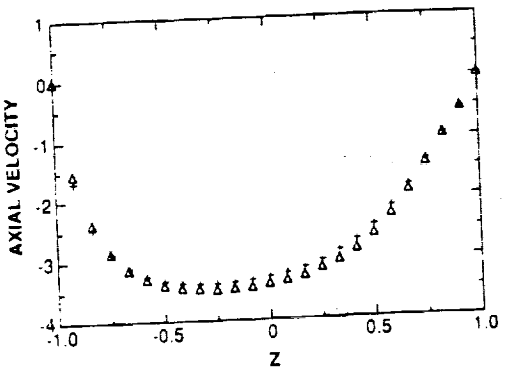

Figure 2. Comparison of surface velocities calculated for $Re = 3150$, $Gr = 0$ and $Pr = 0{\cdot}0127$ using FIDAP and our method ($N_r \times N_z = 25 \times 49$)

Two iterative schemes for determining the surface are discussed in this section. In both schemes the new velocities and temperatures are taken from the current calculated values and the pressure at the surface can be obtained by taking the η-component of the momentum equation and integrating with respect to η. This yields

$$p = \int_0^\eta \left[-\frac{1}{R}\left(\frac{\partial \psi}{\partial s}\frac{\partial w}{\partial \zeta} - \frac{\partial \psi}{\partial \zeta}\frac{\partial w}{\partial s}\right) + \frac{1}{Re}\left(\frac{\partial^2 w}{\partial s^2} + A\frac{\partial^2 w}{\partial \zeta^2} + B\frac{\partial w}{\partial \zeta} + C\frac{\partial^2 w}{\partial s \partial \zeta}\right) + \frac{Gr}{Re^2}T\right]\left(1 + \left(\frac{\partial R}{\partial s}\right)^2\right)^{1/2} \mathrm{d}s. \tag{40}$$

Scheme I is based on the following principle. A shape is assigned to the free surface with the calculated pressure, velocity and temperature. An initial guess for the pressure constant λ is made. The new surface shape is then determined directly from (27)using finite differences in conjunction with Newton's method. The integral (11) is then evaluated to check whether the volume constraint has been satisfied. If it is not satisfied, an inner iteration is made using a Newton–Raphson procedure to calculate the following improved estimate of λ:

$$\lambda^{k+1} = \lambda^k - \left(\frac{\partial V}{\partial \lambda}\right)^{-1} \Delta V, \tag{41}$$

where

$$\Delta V = \int_{-\Lambda/2}^{\Lambda/2} \pi R^2 \mathrm{d}\eta - V_0. \tag{42}$$

The above procedure for determining λ is quite effective and is repeated until the volume constraint is satisfied. $R(\eta)$ is then updated. New velocity, pressure and temperature fields are calculated using the updated value of $R(\eta)$. The outer iteration is repeated until

$$ER = \max\left|\frac{R^{m+1} - R^m}{R^m}\right| < \varepsilon, \tag{43}$$

where we took $\varepsilon = 10^{-4}$.

Scheme II, after Ryskin and Leal,[15] uses the residual of the force balance condition normal to the surface to drive the shape to its steady position. This is equivalent to equating the residual with an artificial capillary force. This effective force causes a local displacement of the surface in the direction of the force. The magnitude of the local displacement is proportional to this force. The surface shape at each iteration is thus modified so as to reduce the residual until condition (27) is met. It follows that at each iteration the new position of the surface is given by

$$R_j^{m+1} = R_j^m + \alpha Ex_j, \tag{44}$$

where Ex_j is the residual of the force balance equation at the jth surface location and the constant coefficient α is determined by numerical experiment. In order to ensure convergence, α should be small. If α is chosen to be too small, the convergence is slow and the amount of CPU time used increases substantially. If α is too large, the solution will diverge. We found that the values of α which led to rapid convergence depend on the product of Re^{-1} and C_0^{-1} (see Table II).

The change in volume between the mth and $(m+1)$th iteration can be found from the volume constraint (11) and equation (44) and neglecting higher-order terms, i.e.

$$\int_{-\Lambda/2}^{\Lambda/2} Ex_j R_j^m \mathrm{d}\eta = 0. \tag{45}$$

The pressure constant λ is contained in Ex_j and is obtained by satisfying (45). Even then the liquid bridge may still change the volume slightly at each iteration owing to numerical error and higher-order effects. These small changes can accumulate and eventually result in a gross error. To prevent this, formula (44) is modified to

$$R_j^{m+1} = R_j^m \left(\frac{V_0}{V_m}\right)^{1/2} + \alpha Ex_j. \tag{46}$$

3.3. Convergence behaviour

The rate of convergence of the two methods is shown in Figure 3 for $Re = 695$ and 2082. In both cases the shapes of the curves clearly reflect the procedure used. The curves show two distinct segments. The abrupt rise in the residual in the late stages of the calculation is caused by requiring a more accurate solution (smaller residual) for the vorticity and streamfunction.

For the calculations carried out here, the first outer iteration scheme converged slightly faster than the second. This is shown in Table III. If the guess for the initial iterate is good, the computation times are about equal. For a poor guess, however, the first scheme is 1·5 times faster. While we were able to obtain convergence for all cases attempted using scheme II, this was not the case for scheme I. We found the first scheme to be quite sensitive to the initial choice of the pressure constant λ. If the value of λ is 'physically unreasonable', the solution diverges. In order to take advantage of the speed afforded by scheme I, we employed the second scheme to calculate the value of λ for the first few iterations. This value is then taken as an initial guess for the first scheme, which is used for the remaining outer iterations.

The convergence of the solution was also checked by varying the spatial resolution of the mesh. This was particularly important at higher values of Re where, owing to the space-centred differences, the streamfunction was prone to exhibit 'wiggles' if the grid Peclet number $Pe_{\mathrm{grid}} = U^*\Delta/\kappa$ (where Δ is the interval between two grid points) exceeded 2 in the vicinity of the

Table II. Optimal values of α as a function of $Re^{-1}C_0^{-1}$

$Re^{-1}C_0^{-1}$	20	2	0·2	0·1	0·06
α	10^{-5}	10^{-4}	10^{-3}	2×10^{-3}	$3\cdot3\times10^{-3}$

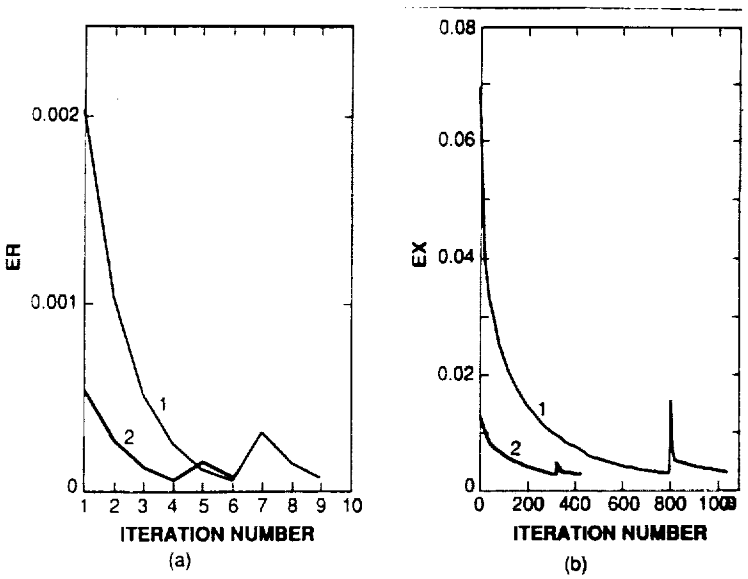

Figure 3. Comparison of convergence rates for (a) scheme I and (b) scheme II

Table III. Sample comparison of CPU times for schemes I and II and for the type of initial guess. The parameters are $\Lambda=2$, $Pr=0{\cdot}023$, $Ma=48$, $Gr=76$, $C_0=4{\cdot}5\times10^{-3}$ and $Bi=100$. A 'good guess' refers to the equilibrium shape of the bridge and a 'poor guess' specifies the surface shape as $R(z)=1+0{\cdot}006\sin[\pi(z+1)]$.

	Computation time (s)	
Initial guess	Scheme I	Scheme II
Good	70	72
Poor	130	332

disks. The wiggles are present for $N_r\times N_z=26\times61$ and are not eliminated until $N_z=101$. As observed by Ryskin and Leal,[15] an increase in the mesh resolution was found to eliminate this problem. We attempted to eliminate the wiggles and avoid the need for mesh refinement by employing second- and third-order upwind schemes for convective terms. We found that while the wiggles were certainly eliminated for $N_r\times N_z=26\times61$ (see Figure 4), the mesh still needed to be refined in order to obtain grid convergence. Since the end result was the same, we concluded that the centred difference scheme was preferable. A mesh of $N_r\times N_z=26\times51$ was found to be sufficient for the results presented here with Reynolds numbers in the range $0<Re<10000$.

We have used the method described earlier to examine the influence of various parameters on momentum and heat transport and meniscus shape. In addition, a favourable comparison for full and half-zones has been made between the results obtained using the combined scheme and those of Hyer *et al.*[11] who employed a finite element scheme.

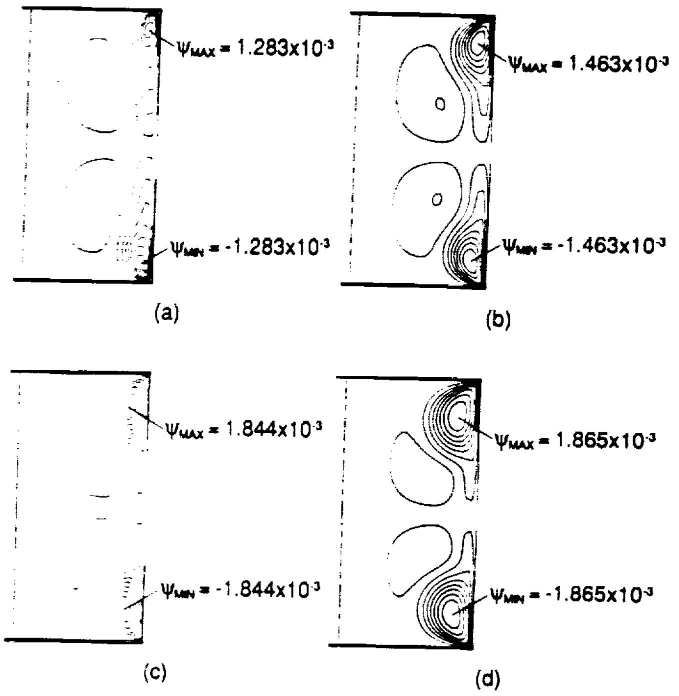

Figure 4. Comparison of results obtained using (a) $N_z=61$, central finite differences, (b) $N_z=61$, third-order upwinding, (c) $N_z=101$, central finite differences and (d) $N_z=101$, third-order upwinding

The effects of varying the temperature difference ΔT (keeping Gr/Re fixed), the Reynolds number Re, the Biot number Bi, the aspect ratio Λ and the Grashof number Gr are presented in the following section.

4. RESULTS

4.1. *Effects of an increase in ΔT at fixed Gr/Re*

Figure 5 shows the meniscus shape, dimensionless streamlines and isotherms calculated for a fluid with the properties of $Gd_5Ga_5O_{12}$, $Pr=4{\cdot}67$, $Bi=100$, $Re=21{\cdot}4$, 107, 215 and 1073 ($Ma=100$, 500, 1002 and 5010) and $Gr/Re=0{\cdot}025$. In all cases the surface tension decreases with increasing temperature. This creates a force tangent to the surface which drives the melt towards the disks and results in the formation of two toroidal rolls with opposite senses of rotation. The gravitational acceleration results in a surface shape that bulges out below $z=0$ and necks in above it. This causes an asymmetry in the structure of the two rolls, with the lower roll being more intense.

At $Re=21{\cdot}4$ ($Ma=100$) heat transport is governed by conduction. In the centre, heat is transported through and along the surface ($Bi=100$), which results in a significant component of the temperature gradient perpendicular to the surface. In the vicinity of the disks the transport of heat is mostly through conduction along the surface. At higher values of Re convection is

ORIGINAL PAGE IS
OF POOR QUALITY

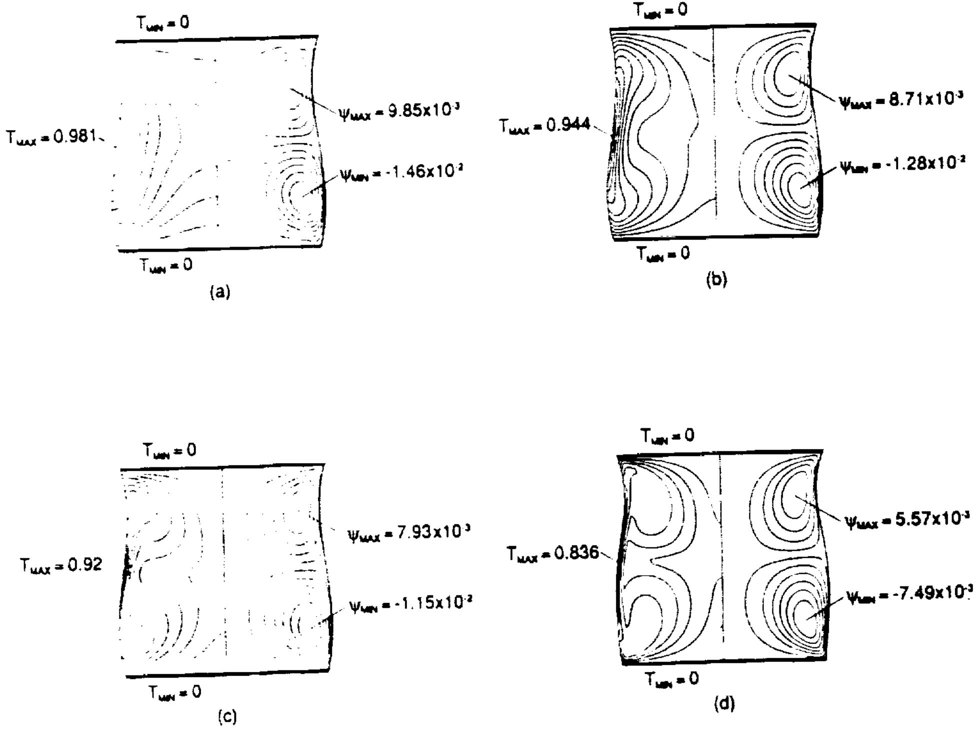

Figure 5. Meniscus shape, streamlines and isotherms calculated for a fluid with the properties of $Gd_5Ga_5O_{12}$, $Pr = 4{\cdot}67$, $Bi = 100$ and $Gr\ Re = 0{\cdot}025$: (a) $Re = 21{\cdot}4$, $c_T = 0{\cdot}089$, $c_\psi = 2{\cdot}2 \times 10^{-3}$; (b) $Re = 107$, $c_T = 0{\cdot}086$, $c_\psi = 1{\cdot}9 \times 10^{-3}$; (c) $Re = 214{\cdot}6$, $c_T = 0{\cdot}084$, $c_\psi = 1{\cdot}8 \times 10^{-3}$; (d) $Re = 1073$, $c_T = 0{\cdot}084$, $c_\psi = 1{\cdot}2 \times 10^{-3}$. The temperature and streamfunction contour intervals are c_T and c_ψ respectively

intensified. The flow velocities reach their maximum values at locations intermediate between the central portion of the surface and the disks. In the central region of the melt the outward flow towards the surface brings cooler melt from the interior and causes a steep temperature gradient perpendicular to the surface. Towards the end walls the frequency with which isotherms intersect the surface increases. This indicates a steeper temperature gradient parallel to the surface.

Figure 6 shows the effect of increasing Gr and Re at fixed Gr/Re ($= 0{\cdot}036$) for a fluid with the properties of molten silicon. As ΔT is increased, the increase in buoyancy-driven flow in the upper region results in a larger upper cell which extends into the lower half. Note that the ratio of the magnitudes of ψ_{max} to ψ_{min} increases as Gr and Re are increased. It is interesting that, even though Gr/Re is small, if the ratio remains constant but the magnitudes of Gr and Re are increased, the buoyancy-driven effect manifests itself more at higher Gr- and Re-values. There is an increase in buoyancy effect due to the (vertically) thermally unstable situation in the upper half which acts together with the radial temperature gradients throughout the liquid bridge to produce a downward motion of colder fluid in the region midway between the axis and the surface. As a result, buoyancy-driven flow becomes pervasive throughout the system and confines the more intense (thermocapillary-driven) cell to a small region in the lower half.

The effect of increasing ΔT on the free surface shape is insignificant for these cases.

ORIGINAL PAGE IS
OF POOR QUALITY

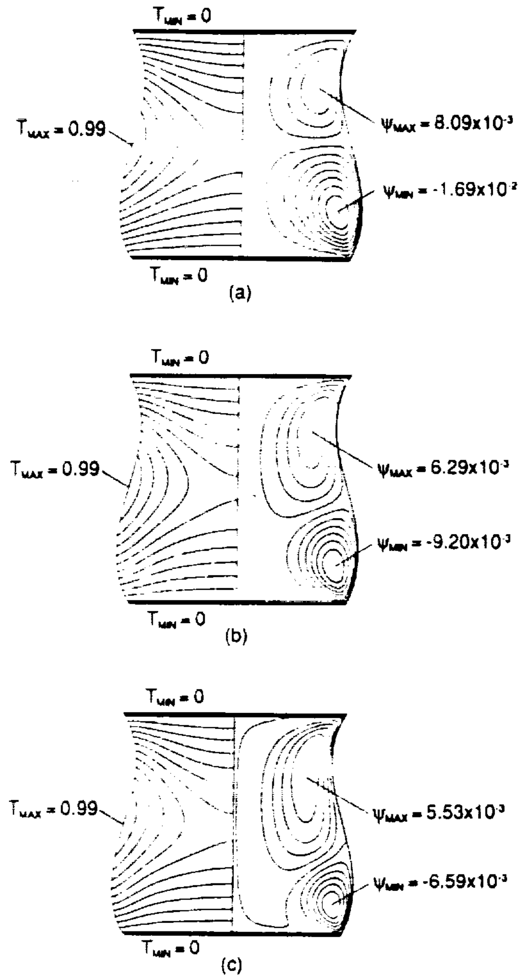

Figure 6. Meniscus shape, streamlines and isotherms calculated for a fluid with the properties of molten silicon, $Pr = 0{\cdot}023$, $Bi = 100$ and $Gr\ Re = 0{\cdot}036$: (a) $Re = 139$, $c_\psi = 2{\cdot}3 \times 10^{-3}$; (b) $Re = 1390$, $c_\psi = 1{\cdot}4 \times 10^{-3}$; (c) $Re = 2082$, $c_\psi = 1{\cdot}1 \times 10^{-3}$; $c_T = 0{\cdot}09$ for all three cases

4.2. *Effect of Biot number*

The effect of Bi on the liquid bridge shape is slight for the cases examined. The isotherm distribution is modified, however, when Bi is increased from 10 to 100 (see Figures 5(b) and 7). In the central part of the surface the temperature gradient is almost perpendicular to the surface in both cases. For $Bi = 100$ the gradient is steeper and the temperature in the central region is higher, which results in a steeper temperature gradient parallel to the surface near the disks. There is a slight decrease in flow intensify for the $Bi = 10$ case.

ORIGINAL PAGE IS
OF POOR QUALITY

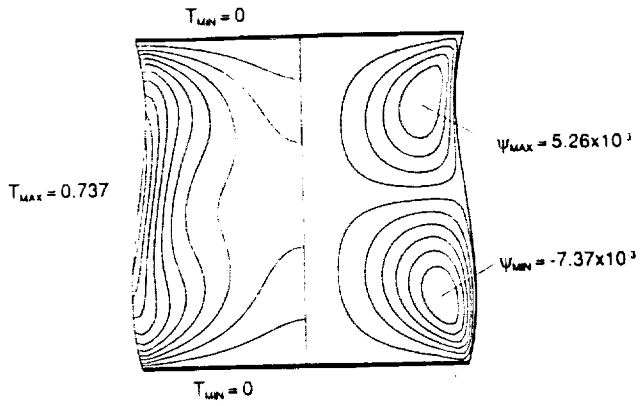

Figure 7. Effect of Bi (compare with Figure 5) for $Bi=10$, $Pr=4{\cdot}667$, $Re=107$, $C_0^{-1}=70$, $G=0{\cdot}468$ and $Gr=2{\cdot}7$. The streamfunction and temperature contour intervals are $1{\cdot}9\times10^{-3}$ and $0{\cdot}086$ respectively

4.3. *Effect of aspect ratio* (Λ)

For otherwise identical physical conditions a change in aspect ratio of the liquid bridge has a significant effect on the meniscus shape. This is illustrated in Figure 8 by a comparison of liquid bridges with $\Lambda=2{\cdot}5$ and 3. The shapes are qualitatively similar but the amplitude of the deformation from a right circular cylinder is much larger for the higher aspect ratio. For the large-aspect-ratio bridge there is a relative decrease in flow intensity in the upper part as the flow conforms to the increased curvature of the surface of the longer liquid bridge. The flow intensity of the lower cell is greater for the longer aspect ratios and the isotherms exhibit correspondingly more distortion. Results obtained for $\Lambda=3{\cdot}2$ confirm this trend (note that with a Bond number $Bo=\rho gR^2/\gamma_0=0{\cdot}7$ the $\Lambda=3{\cdot}2$ bridge is close to the stability limit[17]).

4.4. *Pure thermocapillary flow*

In the absence of gravity $Gr=B_0=0$ and the flow is driven only by surface tension gradients. Figure 9 shows the isotherms and streamlines computed for a fluid with the properties of molten silicon for values of Re up to 21 740. We computed cases with $Re=1390$, 4350, 8695 and 21 740. At $Re\geqslant4350$ we found secondary cells. There is an increase in secondary flow intensiy at higher values of Re (see Figures 9(b) and 9(c)). Even at the higher values of Re the isotherms are only slightly distorted.

For the finite gravity case ($Gr=76$) the effects of surface shape and buoyancy-driven flow are manifested (see Figure 10). Only two cells are evident in the finite gravity case. The larger cell appears to be a combination of a primary thermocapillary cell and a downward flow due to buoyancy near the axis, which extends into the central region of the lower half and interacts with a secondary flow cells associated with the thermocapillary flow. The primary thermocapillary-driven cell in the lower half is considerably smaller in extent than it is for the zero-gravity case. A comparison between zero-gravity and finite gravity conditions illustrates the interaction between the weaker buoyancy-driven flow, the secondary thermocapillary cells (see Figures 9 and 10) and the surface shape.

ORIGINAL PAGE IS
OF POOR QUALITY

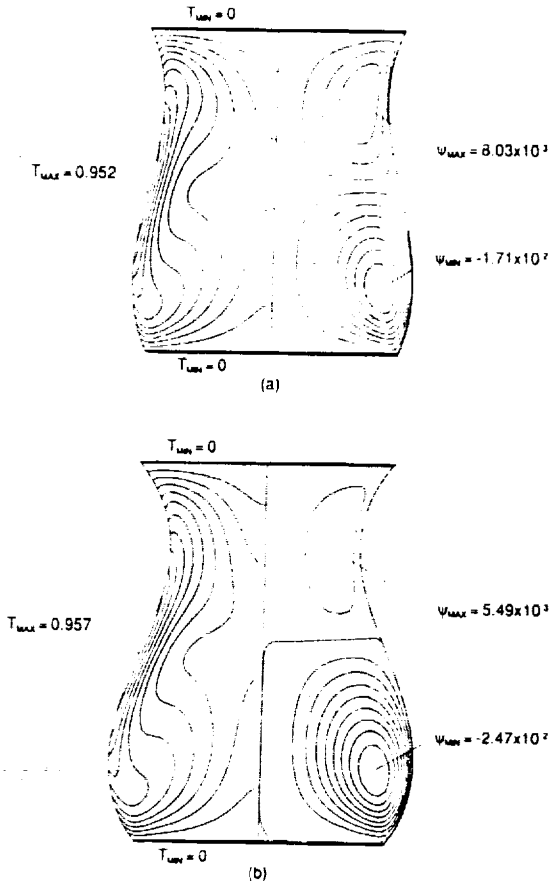

Figure 8. Effect of aspect ratio: (a) $\Lambda = 2{\cdot}5$; (b) $\Lambda = 3$; $Bi = 100$, $B_0 = 0{\cdot}7$, $Pr = 4{\cdot}667$, $Re = 107$, $C_0^{-1} = 70$, $G = 0{\cdot}468$, $Gr = 2{\cdot}7$. The streamfunction contour intervals are $1{\cdot}2 \times 10^{-3}$ and $2{\cdot}3 \times 10^{-3}$ for (a) and (b) respectively and the temperature contour interval is 0·087 for both cases

5. CONCLUSIONS

Steady solutions to the free boundary problem for a non-isothermal liquid bridge have been obtained using a Picard-type iterative scheme with a semi-implicit space-centred finite difference scheme. The method was applied to a variety of problems with Reynolds numbers in the range $0 < Re < 22000$ and for Pradtl numbers of 0·023 and 4·67. The method was found to perform well for this range of parameters examined and compared well with results obtained for buoyancy-driven and surface-tension-driven flow using a finite element method. At high Re we found that the solution was sensitive to the spatial resolution and that a larger number of grid points were necessary in order to avoid 'wiggles' in the solution. For $Re < 10000$ we found $N_r \times N_z = 26 \times 51$ points to be sufficient, but required up to 101 points in the z-direction for $Re = 21\,740$. While it was possible to remove the wiggles using upwind differences, the mesh refinement was still

ORIGINAL PAGE IS
OF POOR QUALITY

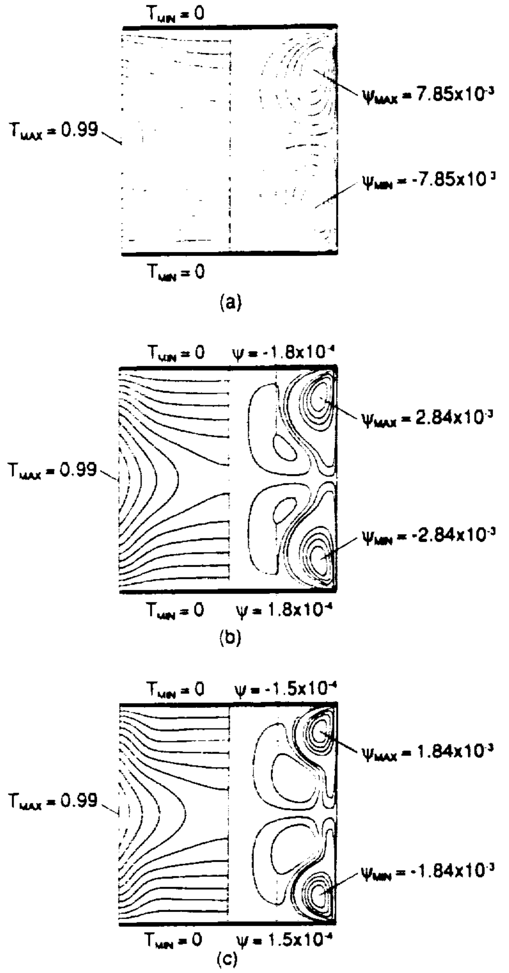

Figure 9. Meniscus shape, streamlines and isotherms calculated for a fluid with the properties of molten silicon, $Pr = 0{\cdot}023$, $Bi = 100$, $Gr = 0$ and $Re =$ (a) 1390, (b) 8695 and (c) 21740. The streamfunction contour intervals are $7{\cdot}7 \times 10^{-4}$, $3{\cdot}7 \times 10^{-4}$ and $2{\cdot}5 \times 10^{-4}$ for (a), (b) and (c) respectively and the temperature contour interval is 0·087 for all three cases

necessary in order to obtain grid convergence. Thus no advantage was obtained by using upwind differencing.

While the parametric study is by no means exhaustive, the results indicate some interesting trends. Perhaps the most interesting behaviour is the response to an increase in the effective maximum temperature difference ΔT. It was found that for a non-zero Grashof number an increase in ΔT caused an increase in intensity of the cell in the lower half of the bridge. For the low-Prandtl-number case it was found that at higher values of ΔT the spatial extent of the lower cell actualy decreased as the less intense upper cell penetrated into the lower part. This can be explained by the increasing importance of radial temperature gradients in driving buoyant flow as

ORIGINAL PAGE IS
OF POOR QUALITY

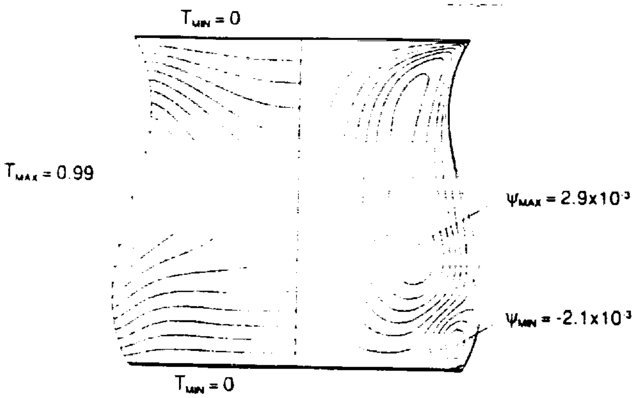

$T_{MIN} = 0$
$T_{MAX} = 0.99$
$\psi_{MAX} = 2.9 \times 10^{-3}$
$\psi_{MIN} = -2.1 \times 10^{-3}$
$T_{MIN} = 0$

Figure 10. Meniscus shape, streamlines and isotherms calculated for a fluid with the properties of molten silicon, $Pr = 0{\cdot}023$, $Bi = 100$, $Gr = 76$ and $Re = 8695$. The streamfunction contour interval is $4{\cdot}6 \times 10^{-4}$ and the temperature contour interval is 0·087

ΔT is increased. As expected from the results of previous work, the effect of changing the aspect ratio was also seen to significantly affect the flow behaviour. For non-zero gravity the increase in convexity of the lower portion of the larger-aspect-ratio bridge has a pronounced effect on the flow pattern, which is more intense for the longer liquid bridge. This increase in flow intensity appears to occur as a result of a decrease in the form drag of the surface. A comparison between the difference in flow intensity between the upper and lower halves reveals that the difference increases with increasing Λ. The form drag in the upper half increases as the magnitude of the negative curvature increases. This shows the flow in the upper half relative to the lower half of the bridge.

Slows

ACKNOWLEDGEMENTS

This work was supported by the National Aeronautics and Space Administration through grant NAG8-724 and also by the State of Alabama through the Center for Microgravity and Materials Research and the Alabama Supercomputer Network.

REFERENCES

1. C. Chang and W. R. Wilcox, 'Inhomogeneities due to thermocapillary flow in floating zone melting', *J. Cryst. Growth*, **28**, 8–12 (1975).
2. P. A. Clark and W. R. Wilcox, 'Influence of gravity on thermocapillary convection in floating zone melting of silicon', *J. Cryst. Growth*, **50**, 461–469 (1980).
3. N. Kobayashi, 'Computer simulation of the steady flow in a cylindrical float zone under low gravity', *J. Cryst. Growth*, **66**, 63–72 (1984).
4. W. W. Fowlis and G. O. Roberts, 'Confinement of thermocapillary floating zone flow', *J. Cryst. Growth*, **74**, 301–320 (1986).
5. A. Rybicki and J. M. Floryan, 'Thermocapillary effects in liquid bridges', *Phys. Fluids*, **30**, 1956–1972 (1987).
6. R. Natarajan, 'Thermocapillary flows in a rotating float zone under microgravity', *AIChE J.*, **35**, 614–624 (1989).
7. Z. Kozhoukharova and S. Slavchev, 'Computer simulation of thermocapillary convection in a non-cylindrical floating zone', *J. Cryst. Growth*, **74**, 236–246 (1986).
8. W. G. Pfann, *Zone melting*, Krueger, Huntington, NY, 1978.
9. J. L. Duranceau and R. A. Brown, 'Finite element analysis of melt convection and interface morphology in earthbound and microgravity floating zones', in T. G. Wang (ed.), *Drops and Bubbles Third Int. Colloq. 1988, AIP Conf. Proc., Vol. 197*, American Institute of Physics, New York, 1989, pp. 133–144.

ORIGINAL PAGE IS
OF POOR QUALITY

10. C. W. Lan and S. Kou, 'Thermocapillary flow and melt/solid interfaces in floating-zone crystal growth under microgravity', *J. Cryst. Growth*, **102**, 609–627 (1990).
11. J. Hyer, D. F. Jankowski and G. P. Neitzel, 'Thermocapillary convection in a model float zone', *AIAA J. Thermophys. Heat Transfer*, in the press.
12. J. M. Floryan, 'Numerical methods for viscous flows with moving boundaries', *Appl. Mech. Rev.*, **42**, 323–341 (1989).
13. I. S. Kang and L. G. Leal, 'Numerical solution of axisymmetric, unsteady free-boundary problems at finite Reynolds number. I Finite difference scheme and its application to the deformation of a bubble in a uniaxial straining flow', *Phys. Fluids*, **30**, 1929–1940 (1987).
14. H. M. Ettouney and R. A. Brown, 'Finite element methods for steady solidification problems', *J. Comput. Phys.*, **49**, 118–150 (1983).
15. G. Ryskin and L. G. Leal, 'Numerical solution of free boundary problems in fluid mechanics. Part I. The finite-difference technique', *J. Fluid Mech.*, **148**, 1–17 (1984).
16. R. Peyret and T. D. Taylor, *Computational Methods for Fluid Flow*, Springer, New York, 1983.
17. I. Martinez, J. M. Haynes and D. Langbein, 'Fluid statics and capillarity', in H. U. Walter (ed.), *Fluid Sciences and Materials Science in Space*, Springer, Berlin, 1987, pp. 53–81.

Au: details? vol. pp. & year?

to appear, October, 1991.

ORIGINAL PAGE IS
OF POOR QUALITY

Appendix 5

N/15

The sensitivity of a non-isothermal liquid bridge to residual acceleration

J. Iwan D. Alexander and Yiqiang Zhang
Center for Microgravity and Materials Research
University of Alabama in Huntsville, Huntsville, Alabama 35899, USA

Abstract

Liquid bridges appear in a variety of industrial processes, for example in the well-known floating-zone crystal growth technique. This crystal growth method has received much attention in recent years. In particular, there have been a variety of experiments on spacelab missions. These experiments are motivated by the fact that the microgravity environment affords the possibility of an increase in the stability of the melt meniscus and a reduction in buoyancy-driven convection. However, within the spacecraft there is a residual acceleration with variable magnitude and orientation. Under certain conditions, the response of the free surface of a liquid bridge to time-dependent residual accelerations will lead to zone breakage. In this paper the steady and unsteady behavior of isothermal and non-isothermal liquid bridge systems under normal and low gravity conditions is examined. The full non-linear governing equations are recast in terms of a stream-function vorticity formulation together with a non-orthogonal coordinate transformation. The latter allows an irregular free boundary to coincide with a coordinate line (or surface) without the need to solve a coupled set of Laplace equations. The resulting equations are discretized using a centered finite difference scheme for space, and an Adams-Bashforth-Crank-Nicolson scheme is used for time. The equations are solved by the A.D.I. method and a Picard type iteration is used on the boundary condition for the balance of force normal to the free surface. For non-isothermal bridges, residual acceleration affects the system by causing internal buoyancy flows and fluctuations in the shape of the bridge which interact with the thermocapillary flow caused by surface tension gradients. For the cases examined, the shape of the bridge is found to be more sensitive to typical spacecraft accelerations than the buoyancy driven flow. The effect of thermocapillary flow on the surface shape is found to be small for the range of capillary and Reynolds numbers considered.

1. Introduction

Liquid bridges appear in a variety of industrial processes, for example the well-known floating-zone crystal growth technique [1]. This crystal growth method has received much attention in recent years [2-10]. In particular, there have been several related experiments on spacelab missions [11-14]. These experiments are motivated by the fact that the microgravity environment affords the possibility of an increase in the stability of the melt meniscus and a reduction in buoyancy-driven convection. However, within the spacecraft there is a residual acceleration with variable magnitude and orientation. Under certain conditions, the response of the free surface of an isothermal liquid bridge to time-dependent residual accelerations will lead to zone breakage [13-15]. In this paper we examine the interaction between convection caused by the response of the free surface of the zone to oscillatory axial residual acceleration and convection due to thermocapillary and internal buoyancy forces.

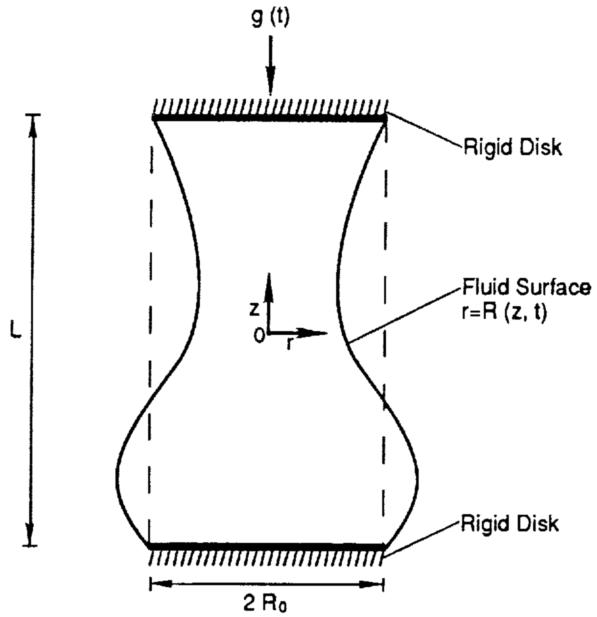

Fig. 1. The model liquid bridge.

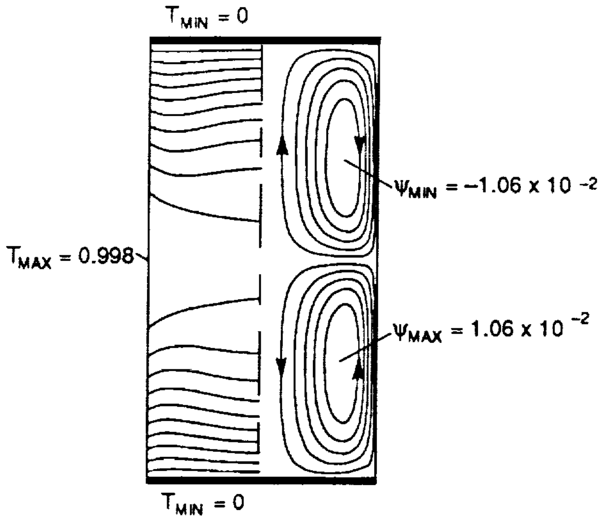

Fig. 2. The initial steady dimensionless stream-function and temperature corresponding to Re = 2899, Gr = 0.98, Λ = 4 and Pr = 0.0127.

2. Formulation

2.1 Description of the Model

A cylindrical liquid zone (see Fig. 1) is contained between two parallel coaxial circular rigid disks (radius = R_0) separated by a distance L. The liquid is a non-isothermal Newtonian fluid for which the Boussinesq approximation holds. The bridge is held between the disks by surface tension. The free surface of the bridge is a gas-liquid interface and is described by r = R(z,t). Each disk is maintained at a constant temperature $\tilde{T}_0$. Surface heating is provided through a parabolic function, $\tilde{T}_\infty$, which is a function of the axial coordinate and is an approximation to the heating profile associated with typical floating zone crystal growth experiments. The heat transfer coefficient at the free surface is denoted by h. In addition, we make the assumptions that the residual acceleration is parallel to the cylinder axis, the velocity and temperature field and the deformation of free surface are axisymmetric, and we take the surface tension at the free surface to be a linear function of the temperature. Motion of the end disks perpendicular to the axis may also occur in practice. The restriction to axial acceleration precludes an analysis of the effects of such motions.

The governing equations are made dimensionless by scaling length, time and velocity with R_0, R_0/U^* and U^*, respectively. Here U^* is a characteristic velocity given by

$$U^* = \frac{|\gamma_T|\Delta\tilde{T}}{\mu},$$

where $\Delta\tilde{T} = \tilde{T}_{MAX} - \tilde{T}_{MIN}$ represents the maximum temperature difference along the surface, $|\gamma_T|$ is the absolute value of the derivative of the surface tension with respect to temperature, and μ is the dynamic viscosity. The difference ΔT is used to non-dimensionalize temperature.

The temperature maximum in a floating zone occurs between the two ends of the zone. We shall take the dimensionless ambient temperature T_{MAX} to be $T_\infty(0)$, and T_{MIN} to be $T_\infty(\pm\Lambda/2)$, where $\Lambda = L/R_o$ is the aspect ratio.

The non-dimensional pressure is

$$p = \frac{p^* + \rho_0 g^*(t)\, z}{\rho_0 U^{*2}} R_0 ,$$

where p^* is the dimensional pressure, z is the dimensionless axial coordinate, ρ_0 is the density corresponding to the reference temperature and $g^*(\tilde{t}) = g_0 + g_1 \sin(2\pi f \tilde{t})$ is the residual gravitational acceleration.

2.2 Basic Equations

With the scales presented in *2.1* the governing dimensionless equations in a cylindrical coordinate system can be written as

$$\frac{1}{r}\frac{\partial(ru)}{\partial r} + \frac{\partial w}{\partial z} = 0 , \tag{1}$$

$$\frac{\partial u}{\partial t} + u\frac{\partial u}{\partial r} + w\frac{\partial u}{\partial z} = -\frac{\partial p}{\partial r} + \frac{1}{Re}\left(\frac{\partial^2 u}{\partial r^2} + \frac{1}{r}\frac{\partial u}{\partial r} + \frac{\partial^2 u}{\partial z^2} - \frac{u}{r^2}\right) , \tag{2}$$

$$\frac{\partial w}{\partial t} + u\frac{\partial w}{\partial r} + w\frac{\partial w}{\partial z} = -\frac{\partial p}{\partial z} + \frac{1}{Re}\left(\frac{\partial^2 w}{\partial r^2} + \frac{1}{r}\frac{\partial w}{\partial r} + \frac{\partial^2 w}{\partial z^2}\right) + \frac{Gr}{Re^2}\, T\, g(t), \tag{3}$$

$$\frac{\partial T}{\partial t} + u\frac{\partial T}{\partial r} + w\frac{\partial T}{\partial z} = \frac{1}{Ma}\left(\frac{\partial^2 T}{\partial r^2} + \frac{1}{r}\frac{\partial T}{\partial r} + \frac{\partial T}{\partial z^2}\right) , \tag{4}$$

where $g(t) = g^*(\tilde{t})/g_0$ is a time-dependent dimensionless residual acceleration, and

$$Re = \frac{R_o U^*}{\nu} \ , \quad Ma = \frac{|\gamma_T|\Delta T R_o}{\mu\kappa} , \quad Gr = \frac{|g_o|\beta\Delta T R_o^3}{\nu^2} ,$$

are, respectively, the Reynolds number, Marangoni number and Grashof number. Here, ν is the kinematic viscosity, κ is the thermal diffusivity, β is the volume thermal expansion and coefficient.

The boundary conditions at the rigid end disks are

$$u = T = 0,\ w = w^{\pm}(t),\ \text{at } z = \pm\frac{\Lambda}{2}, \tag{5}$$

where $w^{\pm}(t)$ is zero if the two disks vibrate in phase (this will admit only odd mode deformations of the zone surface [15]). The symmetry conditions at the centerline $r = 0$ are

$$u = \frac{\partial w}{\partial r} = \frac{\partial T}{\partial r} = 0, \tag{6}$$

The boundary conditions at the free surface $r = R(z)$ take the form

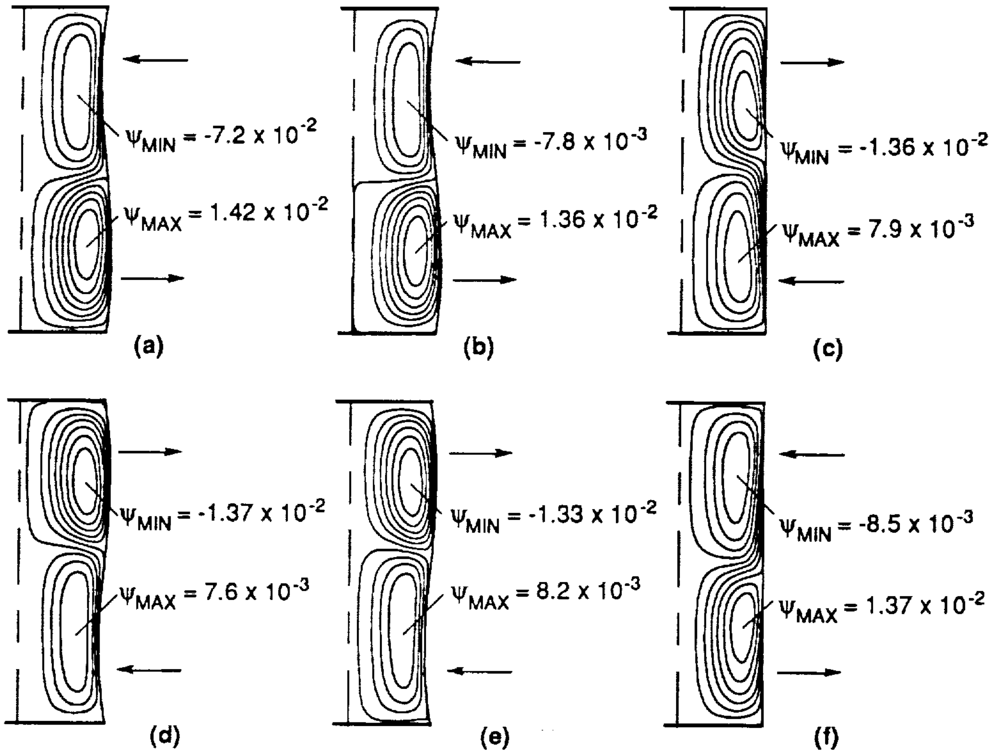

Fig. 3. The instantaneous dimensionless stream-functions with Re = 2899, Gr = 0.98, $\Lambda = 4$ and Pr = 0.0127, at (a) 0.52 s, (b) 0.59 s, (c) 1 s, (d) 1.5 s (e) 1.56 s, (f) 2 s, after application of an additional 2.5×10^{-2} g, 0.5 Hz, axial acceleration.

$$p - \frac{g(t)z}{F^2} + \lambda = \frac{2Re^{-1}}{1 + \left(\frac{\partial R}{\partial z}\right)^2}\left[\frac{\partial u}{\partial r} + \left(\frac{\partial R}{\partial z}\right)^2 \frac{\partial w}{\partial z} - \frac{\partial R}{\partial z}\left(\frac{\partial w}{\partial r} + \frac{\partial u}{\partial z}\right)\right] + \tag{7}$$

$$\frac{Re^{-1}\left(C_0^{-1} - T\right)}{\left[1 + \left(\frac{\partial R}{\partial z}\right)^2\right]^{\frac{3}{2}}}\left[\frac{1 + \left(\frac{\partial R}{\partial z}\right)^2}{R} - \frac{\partial^2 R}{\partial z^2}\right],$$

$$\left[1 - \left(\frac{\partial R}{\partial z}\right)^2\right]\left(\frac{\partial u}{\partial z} + \frac{\partial w}{\partial r}\right) + 2\frac{\partial R}{\partial z}\left(\frac{\partial u}{\partial r} - \frac{\partial w}{\partial z}\right) = -\left[1 + \left(\frac{\partial R}{\partial z}\right)^2\right]^{\frac{1}{2}}\left(\frac{\partial T}{\partial z} + \frac{\partial R}{\partial z}\frac{\partial T}{\partial r}\right), \tag{8}$$

$$\frac{\partial R}{\partial t} + u + w\frac{\partial R}{\partial z} = 0 \ , \tag{9}$$

$$\left(1 + \left(\frac{\partial R}{\partial z}\right)^2\right)^{-\frac{1}{2}}\left(\frac{\partial T}{\partial r} - \frac{\partial R}{\partial z}\frac{\partial T}{\partial z}\right) + Bi\left(T - T_\infty\right) = 0, \tag{10}$$

where the capillary number, Biot number and Froude number are, respectively,

$$C_o = \frac{|\gamma_T|\Delta T}{\gamma_o}, \ Bi = \frac{hR_o}{k}, \ F = \left(\frac{gR_o}{U^{*2}}\right)^{-\frac{1}{2}},$$

and γ_o is the mean surface tension and k is the thermal conductivity. The force balance conditions normal and tangent to the free surface are given by eqs. (7) and (8) respectively. Equation (9) is the kinematic boundary condition at the liquid-gas interface. The thermal boundary condition at the interface is given by equation (10) in which the equivalent heat transfer coefficient, h, models the effect of the radiant and convective heat transfer between the bridge and the surrounding environment. The constant λ in (7) represents a dimensionless reference pressure difference across the interface which for this system is determined by the following constant volume constraint [9,16]

$$V = \int_{\frac{-\Lambda}{2}}^{\frac{\Lambda}{2}} \pi R^2(z) dz = V_o \equiv \text{constant}. \qquad (11)$$

Finally, the condition that the contact lines between the liquid end disks are fixed is

$$R = 1 \text{ at } z = \pm \Lambda/2. \qquad (12)$$

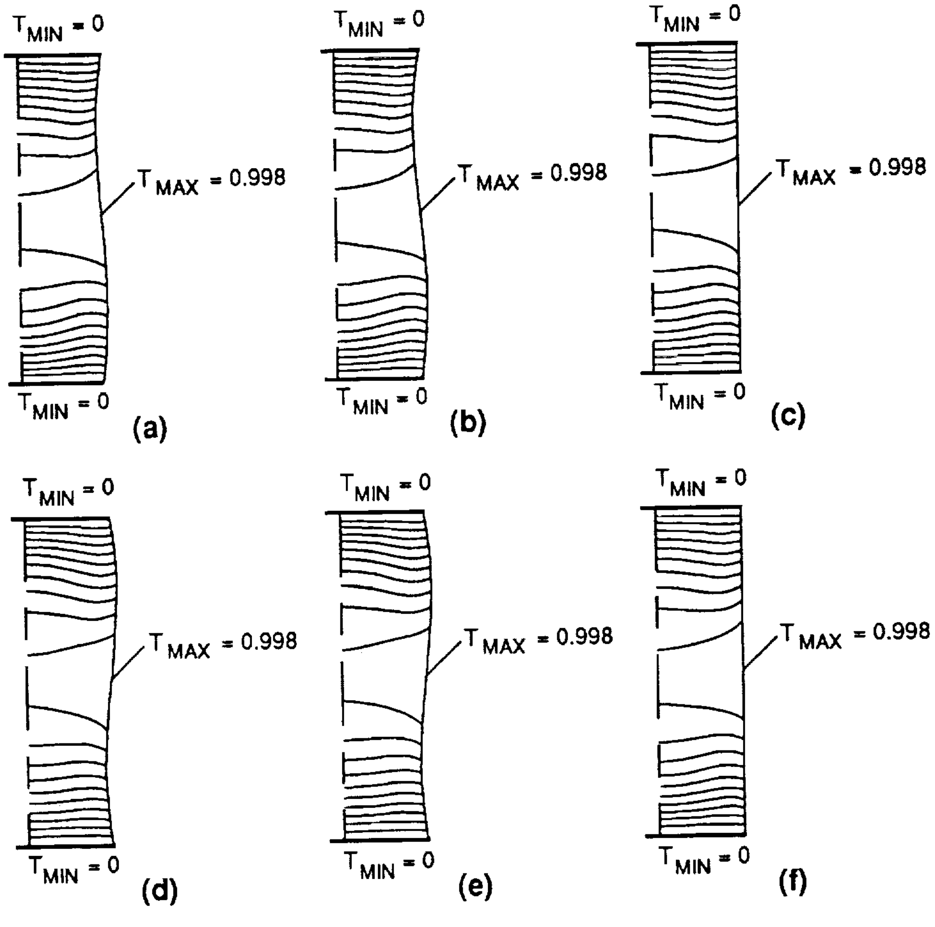

Fig. 4. The dimensionless temperature field with Re = 2899, Gr = 0.98, $\Lambda = 4$ and Pr = 0.0127, at (a) 0.52 s, (b) 0.59 s, (c) 1 s, (d) 1.5 s (e) 1.56 s, (f) 2 s, after application of an additional 2.5×10^{-2} g, 0.5 Hz, axial acceleration.

2.3 *Solution Method*

In the present investigation, the governing equations are recast in terms of a stream-function vorticity formulation. The stream-function is defined by

$$u = \frac{1}{r}\frac{\partial \Psi}{\partial z}, \quad v = -\frac{1}{r}\frac{\partial \Psi}{\partial r}. \tag{13}$$

A non-orthogonal coordinate transformation,

$$\eta = z \ , \quad \xi = \frac{r}{R(z,t)} , \tag{14}$$

allows an irregular free boundary to coincide with a cylindrical coordinate line (or surface) without the need to solve a coupled set of Laplace equations [17,18]. The resulting equations are discretized following a semi-implicit difference scheme and solved by the A.D.I. method. The conditions for force balance tangent to the surface and kinematic condition at the free surface are solved along with the Navier-Stokes and continuity equations. The condition for the force balance normal to the surface is used together with an "outer" iterative procedure to determine the free surface shape.

The unsteady free boundary problem for a cylindrical liquid zone is solved as follows. The

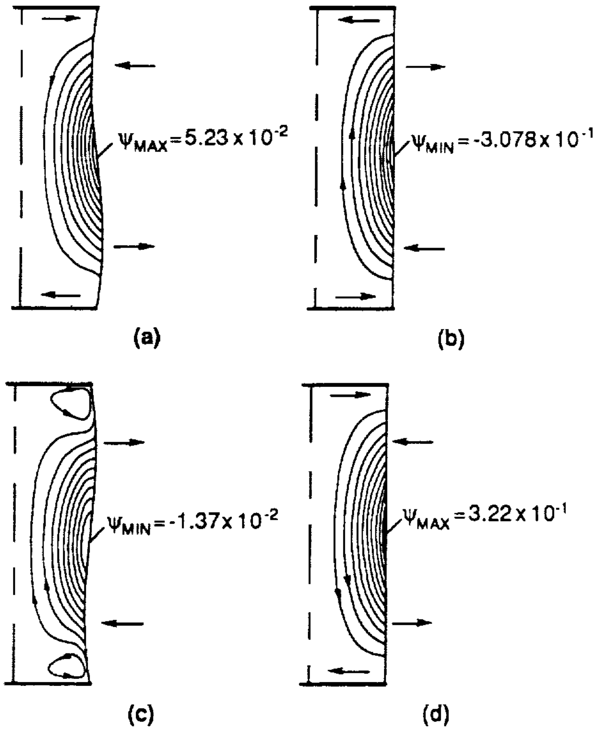

$\Psi_{MAX}=5.23\times10^{-2}$
$\Psi_{MIN}=-3.078\times10^{-1}$
(a)
(b)
$\Psi_{MIN}=-1.37\times10^{-2}$
$\Psi_{MAX}=3.22\times10^{-1}$
(c)
(d)

Fig. 5. The instantaneous dimensionless stream-function, with Re = 0, Gr = 0, $\Lambda = 4$ and Pr = 0.0127, at (a) 0.59 s, (b) 1 s, (d) 1.5 s (e) 2 s, after application of an additional 2.5×10^{-2} g, 0.5 Hz, axial acceleration. Note that for this case only, $\Psi = \Psi/\kappa R_0$, where Ψ is the dimensional stream-function cm^3 s^{-1}.

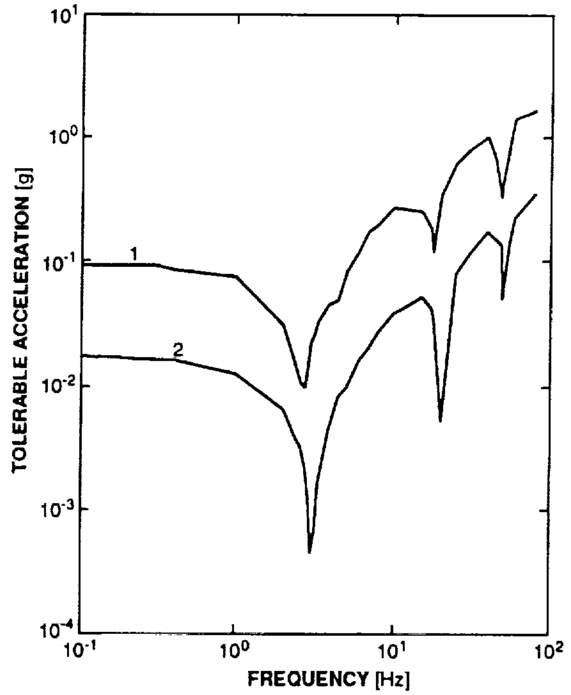

Fig. 6. Tolerable acceleration [g] vs. Frequency [Hz] predicted by the 1D model [15] for (1) breakage and (2) 10% shape change, for an isothermal liquid zone with $\Lambda = 4$ and the thermophysical properties of indium.

initial conditions correspond to either zero or finite steady residual acceleration situations with a steady thermocapillary flow. These states are calculated using a method close to that described below [16]. For the unsteady calculation our solution scheme is similar to that used by Kang and Leal [17] and Ryskin and Leal [18]. The following Picard iterative procedure [19] is adopted:

1. guess the free surface shape for the new timestep;
2. obtain the approximate temperature and stream-function, vorticity and velocity fields by transforming the governing equations and boundary conditions to a circular cylindrical domain via a non-orthogonal transformation and solve them using a semi-implicit method;
3. obtain the pressure at the free surface by integrating the transformed momentum equation;
4. use the condition for the balance of force normal to the free surface to decide how to update the free surface location;
5. return to step 2. Repeat until convergence is obtained by satisfying all equations and boundary conditions to a specified degree of accuracy for this timestep.

3. Results and Discussion

The following results were obtained for a liquid zone corresponding to the physical properties of molten indium subject to an axial acceleration with a frequency of 0.5 Hz. Fig. 2 depicts the initial state of the system. A steady axial acceleration of magnitude 10^{-4} g (10^{-3} m s^{-2}) acts along the negative z-direction. Two equidimensional toroidal rolls indicate that surface-driven flow is dominant (Re = 2899, Gr = 0.98). The isotherm distribution shows that heat transfer is mainly by conduction, although some distortion of the isotherms by the flow is evident. For indium, Lind [20] has reported that the surface tension increases with increasing temperature i.e. $\gamma_T > 0$. (Note that surface contamination may have affected the measured temperature dependence of surface tension in this case.) Thus, the flow direction at the surface is toward the center (i.e. the higher temperature region). Figs. 3 and 4 illustrate the effect of an additional acceleration component which varies sinusoidally with a frequency of 0.5 Hz. Figure 5 depicts the response of the zone to the same disturbance, but with Gr = Ma = 0. (Note that, for this case, κ/L rather than $|\gamma_T| \Delta T/\mu$ was used as the velocity scale.) In another case with Re = 2899, Gr = 0.98 and the surface constrained to be a circular cylinder, no observable response occurred. Clearly the system is more sensitive to the effects of free surface motion than internal buoyancy. Given that the value of steady acceleration used is extreme for spacecraft acceleration environments [21], we may conclude that for systems where internal buoyancy-driven effects are not manifested (in this case because they are swamped by the surface-driven flow) it suffices to examine the response of the free surface only. Furthermore, a comparison of our full axisymmetric results with those obtained with a simplified 1D isothermal model indicates that, at least for the conditions examined, the 1D model may be used to reliably predict liquid zone (isothermal and nonisothermal) sensitivity. The 1D model is described in detail in [15]. Fig. 6 shows the sensitivity of an indium liquid zone to axial acceleration. The curves are based on results obtained using two sensitivity criteria. The first is determined by breakage of the bridge, the second is whenever the bridge shape changes by more than 10% of its static shape, i.e. $R(z,t) - R(z,0) = .1R(z,0)$.

Acknowledgements

This work was supported by the State of Alabama through the Center for Microgravity and Materials Research and the Alabama Supercomputer Network, and by the National Aeronautics and Space Agency through grant NAG8-724.

4. References

[1] W.G. Pfann, *Zone Melting*, Krueger, Huntington New York (1978).

[2] C. Chang and W.R. Wilcox, J. Crystal Growth **28**, 8-12 (1975).

[3] P.A. Clark and W.R. Wilcox, J. Crystal Growth **50,** 461-469 (1980).

[4] N. Kobayashi, J. Crystal Growth **66**, 63-72 (1984).

[5] W.W. Fowlis and G.O. Roberts, J. Crystal Growth **74**, 301-320 (1986).

[6] A. Rybicki and J.M. Floryan, Phys. Fluids **30**, 1956-1972 (1987).

[7] R. Natarjan, AIChE J. **35,** 614-624 (1989).

[8] Z. Kozhoukharova and S. Slavchev, J. Crystal Growth **74**, 236-246 (1986).

[9] J.L. Duranceau and R.A. Brown, in Taylor G. Wang (ed.) *Drops and Bubbles Third International Colloquium 1988*, AIP Conference Proceedings **197**, American Institute of Physics, New York, 1989, pp. 133-144.

[10] C.W. Lan and S. Kou, J. Crystal Growth **102**, 609-627 (1990).

[11] D.T.J. Hurle, G. Müller and R. Nitsche, in *Fluid Sciences and Materials Science in Space*, Ed. H. U. Walter (Springer Verlag, Berlin, 1987) pp. 313-351.

[12] A. Cröll, W. Müller and R. Nitsche, *Proceedings of the 6th European Symposium on Materials Sciences under Microgravity Conditions*, **ESA SP-256** (ESA Publications Division, Noordwjyck, 1987) 87.

[13] I. Martinez, J.M. Haynes and D. Langbein,in *Fluid Sciences and Materials Science in Space*, Ed. H. U. Walter (Springer Verlag, Berlin, 1987) pp. 53-80.

[14] I. Martinez, *Proceedings of the 6th European Symposium on Materials Sciences under Microgravity Conditions*, **ESA SP-256** (ESA Publications Division, Noordwjyck, 1987) 235.

[15] Y.Q. Zhang and J.I.D. Alexander, *Physics of Fluids A* **2**, 1966 (1990).

[16] Y.Q. Zhang and J.I.D. Alexander, *International Journal for Numerical Methods in Fluids* in press.

[17] I.S. Kang and L.G. Leal, *Physics of Fluids* **30**, 1929-1940 (1987).

[18] G. Ryskin and L.G. Leal, *J. Fluid Mech.* **148**, 1-17 (1984).

[19] J.M. Floryan, *Appl. Mech. Rev.* **42**, 323-341 (1989).

[20] M.D. Lind, *Proceedings of the AIAA 25th Aerospace Sciences Meeting, Reno, Nevada,* AIAA-87-0618 (1987).

[21] J.I.D. Alexander, *Microgravity Science and Technology* **3**, 52 (1990).

The sensitivity of a non-isothermal liquid bridge to residual acceleration

J. Iwan D. Alexander and Yiqiang Zhang
Center for Microgravity and Materials Research
University of Alabama in Huntsville, Huntsville, Alabama 35899, USA

Abstract

Liquid bridges appear in a variety of industrial processes, for example in the well-known floating-zone crystal growth technique. This crystal growth method has received much attention in recent years. In particular, there have been a variety of experiments on spacelab missions. These experiments are motivated by the fact that the microgravity environment affords the possibility of an increase in the stability of the melt meniscus and a reduction in buoyancy-driven convection. However, within the spacecraft there is a residual acceleration with variable magnitude and orientation. Under certain conditions, the response of the free surface of a liquid bridge to time-dependent residual accelerations will lead to zone breakage. In this paper the steady and unsteady behavior of isothermal and non-isothermal liquid bridge systems under normal and low gravity conditions is examined. The full non-linear governing equations are recast in terms of a stream-function vorticity formulation together with a non-orthogonal coordinate transformation. The latter allows an irregular free boundary to coincide with a coordinate line (or surface) without the need to solve a coupled set of Laplace equations. The resulting equations are discretized using a centered finite difference scheme for space, and an Adams-Bashforth-Crank-Nicolson scheme is used for time. The equations are solved by the A.D.I. method and a Picard type iteration is used on the boundary condition for the balance of force normal to the free surface. For non-isothermal bridges, residual acceleration affects the system by causing internal buoyancy flows and fluctuations in the shape of the bridge which interact with the thermocapillary flow caused by surface tension gradients. For the cases examined, the shape of the bridge is found to be more sensitive to typical spacecraft accelerations than the buoyancy driven flow. The effect of thermocapillary flow on the surface shape is found to be small for the range of capillary and Reynolds numbers considered.

1. Introduction

Liquid bridges appear in a variety of industrial processes, for example the well-known floating-zone crystal growth technique [1]. This crystal growth method has received much attention in recent years [2-10]. In particular, there have been several related experiments on spacelab missions [11-14]. These experiments are motivated by the fact that the microgravity environment affords the possibility of an increase in the stability of the melt meniscus and a reduction in buoyancy-driven convection. However, within the spacecraft there is a residual acceleration with variable magnitude and orientation. Under certain conditions, the response of the free surface of an isothermal liquid bridge to time-dependent residual accelerations will lead to zone breakage [13-15]. In this paper we examine the interaction between convection caused by the response of the free surface of the zone to oscillatory axial residual acceleration and convection due to thermocapillary and internal buoyancy forces.

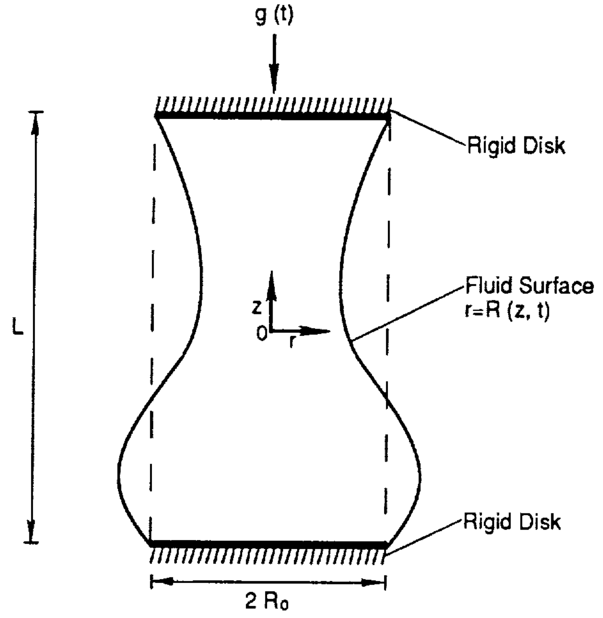

Fig. 1. The model liquid bridge.

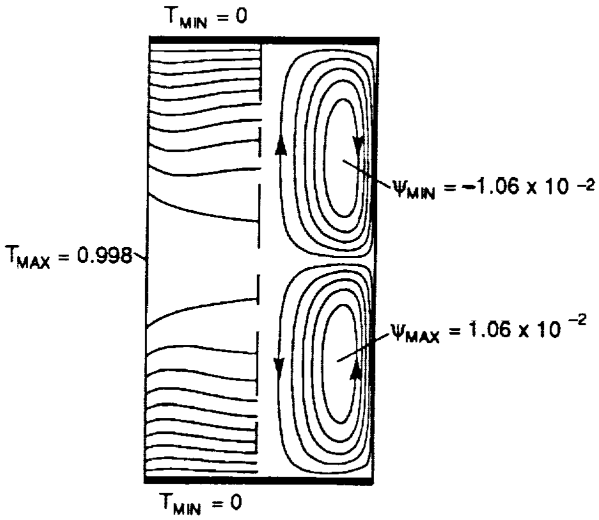

Fig. 2. The initial steady dimensionless streamfunction and temperature corresponding to Re = 2899, Gr = 0.98, $\Lambda = 4$ and Pr = 0.0127.

2. Formulation

2.1 Description of the Model

A cylindrical liquid zone (see Fig. 1) is contained between two parallel coaxial circular rigid disks (radius $= R_0$) separated by a distance L. The liquid is a non-isothermal Newtonian fluid for which the Boussinesq approximation holds. The bridge is held between the disks by surface tension. The free surface of the bridge is a gas-liquid interface and is described by $r = R(z,t)$. Each disk is maintained at a constant temperature $\tilde{T}_0$. Surface heating is provided through a parabolic function, $\tilde{T}_\infty$, which is a function of the axial coordinate and is an approximation to the heating profile associated with typical floating zone crystal growth experiments. The heat transfer coefficient at the free surface is denoted by h. In addition, we make the assumptions that the residual acceleration is parallel to the cylinder axis, the velocity and temperature field and the deformation of free surface are axisymmetric, and we take the surface tension at the free surface to be a linear function of the temperature. Motion of the end disks perpendicular to the axis may also occur in practice. The restriction to axial acceleration precludes an analysis of the effects of such motions.

The governing equations are made dimensionless by scaling length, time and velocity with R_0, R_0/U^* and U^*, respectively. Here U^* is a characteristic velocity given by

$$U^* = \frac{|\gamma_T| \Delta\tilde{T}}{\mu},$$

where $\Delta\tilde{T} = \tilde{T}_{MAX} - \tilde{T}_{MIN}$ represents the maximum temperature difference along the surface, $|\gamma_T|$ is the absolute value of the derivative of the surface tension with respect to temperature, and μ is the dynamic viscosity. The difference ΔT is used to non-dimensionalize temperature.

The temperature maximum in a floating zone occurs between the two ends of the zone. We shall take the dimensionless ambient temperature T_{MAX} to be $T_\infty(0)$, and T_{MIN} to be $T_\infty(\pm\Lambda/2)$, where $\Lambda = L/R_o$ is the aspect ratio.

The non-dimensional pressure is

$$p = \frac{p^* + \rho_0 g^*(\tilde{t})\, z}{\rho_0 U^{*2}} R_0 ,$$

where p^* is the dimensional pressure, z is the dimensionless axial coordinate, ρ_0 is the density corresponding to the reference temperature and $g^*(\tilde{t}) = g_0 + g_1 \sin(2\pi f \tilde{t})$ is the residual gravitational acceleration.

2.2 Basic Equations

With the scales presented in *2.1* the governing dimensionless equations in a cylindrical coordinate system can be written as

$$\frac{1}{r}\frac{\partial(ru)}{\partial r} + \frac{\partial w}{\partial z} = 0 , \tag{1}$$

$$\frac{\partial u}{\partial t} + u\frac{\partial u}{\partial r} + w\frac{\partial u}{\partial z} = -\frac{\partial p}{\partial r} + \frac{1}{Re}\left(\frac{\partial^2 u}{\partial r^2} + \frac{1}{r}\frac{\partial u}{\partial r} + \frac{\partial^2 u}{\partial z^2} - \frac{u}{r^2}\right) , \tag{2}$$

$$\frac{\partial w}{\partial t} + u\frac{\partial w}{\partial r} + w\frac{\partial w}{\partial z} = -\frac{\partial p}{\partial z} + \frac{1}{Re}\left(\frac{\partial^2 w}{\partial r^2} + \frac{1}{r}\frac{\partial w}{\partial r} + \frac{\partial^2 w}{\partial z^2}\right) + \frac{Gr}{Re^2}\, T\, g(t), \tag{3}$$

$$\frac{\partial T}{\partial t} + u\frac{\partial T}{\partial r} + w\frac{\partial T}{\partial z} = \frac{1}{Ma}\left(\frac{\partial^2 T}{\partial r^2} + \frac{1}{r}\frac{\partial T}{\partial r} + \frac{\partial T}{\partial z^2}\right) , \tag{4}$$

where $g(t) = g^*(\tilde{t})/g_0$ is a time-dependent dimensionless residual acceleration, and

$$Re = \frac{R_o U^*}{\nu} \quad , \quad Ma = \frac{|\,\gamma_T|\Delta T R_o}{\mu\kappa} , \quad Gr = \frac{|g_o|\beta\Delta T R_o^3}{\nu^2} ,$$

are, respectively, the Reynolds number, Marangoni number and Grashof number. Here, ν is the kinematic viscosity, κ is the thermal diffusivity, β is the volume thermal expansion and coefficient.

The boundary conditions at the rigid end disks are

$$u = T = 0, \; w = w^{\pm}(t), \text{ at } z = \pm\frac{\Lambda}{2}, \tag{5}$$

where $w^{\pm}(t)$ is zero if the two disks vibrate in phase (this will admit only odd mode deformations of the zone surface [15]). The symmetry conditions at the centerline $r = 0$ are

$$u = \frac{\partial w}{\partial r} = \frac{\partial T}{\partial r} = 0, \tag{6}$$

The boundary conditions at the free surface $r = R(z)$ take the form

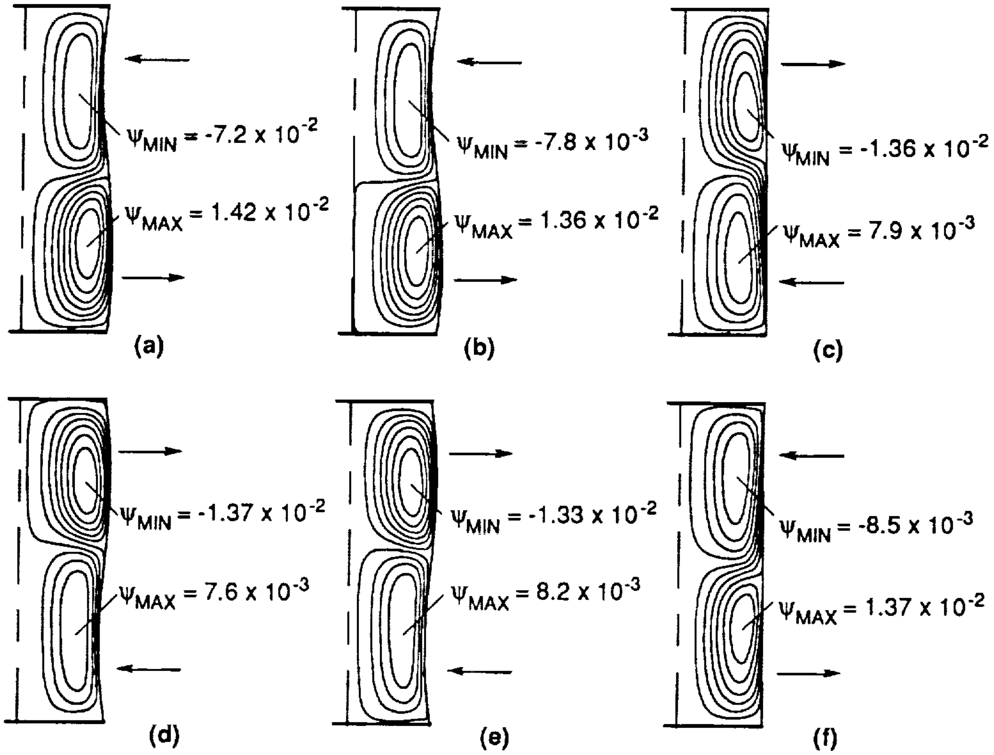
$\psi_{MIN} = -7.2 \times 10^{-2}$
$\psi_{MAX} = 1.42 \times 10^{-2}$
(a)
$\psi_{MIN} = -7.8 \times 10^{-3}$
$\psi_{MAX} = 1.36 \times 10^{-2}$
(b)
$\psi_{MIN} = -1.36 \times 10^{-2}$
$\psi_{MAX} = 7.9 \times 10^{-3}$
(c)
$\psi_{MIN} = -1.37 \times 10^{-2}$
$\psi_{MAX} = 7.6 \times 10^{-3}$
(d)
$\psi_{MIN} = -1.33 \times 10^{-2}$
$\psi_{MAX} = 8.2 \times 10^{-3}$
(e)
$\psi_{MIN} = -8.5 \times 10^{-3}$
$\psi_{MAX} = 1.37 \times 10^{-2}$
(f)

Fig. 3. The instantaneous dimensionless stream-functions with Re = 2899, Gr = 0.98, $\Lambda = 4$ and Pr = 0.0127, at (a) 0.52 s, (b) 0.59 s, (c) 1 s, (d) 1.5 s (e) 1.56 s, (f) 2 s, after application of an additional 2.5×10^{-2} g, 0.5 Hz, axial acceleration.

$$p - \frac{g(t)z}{F^2} + \lambda = \frac{2Re^{-1}}{1 + \left(\frac{\partial R}{\partial z}\right)^2}\left[\frac{\partial u}{\partial r} + \left(\frac{\partial R}{\partial z}\right)^2 \frac{\partial w}{\partial z} - \frac{\partial R}{\partial z}\left(\frac{\partial w}{\partial r} + \frac{\partial u}{\partial z}\right)\right] + \frac{Re^{-1}\left(C_0^{-1} - T\right)}{\left[1 + \left(\frac{\partial R}{\partial z}\right)^2\right]^{\frac{3}{2}}}\left[\frac{1 + \left(\frac{\partial R}{\partial z}\right)^2}{R} - \frac{\partial^2 R}{\partial z^2}\right], \tag{7}$$

$$\left[1 - \left(\frac{\partial R}{\partial z}\right)^2\right]\left(\frac{\partial u}{\partial z} + \frac{\partial w}{\partial r}\right) + 2\frac{\partial R}{\partial z}\left(\frac{\partial u}{\partial r} - \frac{\partial w}{\partial z}\right) = -\left[1 + \left(\frac{\partial R}{\partial z}\right)^2\right]^{\frac{1}{2}}\left(\frac{\partial T}{\partial z} + \frac{\partial R}{\partial z}\frac{\partial T}{\partial r}\right), \tag{8}$$

$$\frac{\partial R}{\partial t} + u + w\frac{\partial R}{\partial z} = 0 , \tag{9}$$

$$\left(1 + \left(\frac{\partial R}{\partial z}\right)^2\right)^{-\frac{1}{2}}\left(\frac{\partial T}{\partial r} - \frac{\partial R}{\partial z}\frac{\partial T}{\partial z}\right) + Bi\left(T - T_\infty\right) = 0, \tag{10}$$

where the capillary number, Biot number and Froude number are, respectively,

$$C_o = \frac{|\gamma_T|\Delta T}{\gamma_0}, \; Bi = \frac{hR_o}{k}, \; F = \left(\frac{gR_o}{U^{*2}}\right)^{-\frac{1}{2}},$$

and γ_0 is the mean surface tension and k is the thermal conductivity. The force balance conditions normal and tangent to the free surface are given by eqs. (7) and (8) respectively. Equation (9) is the kinematic boundary condition at the liquid-gas interface. The thermal boundary condition at the interface is given by equation (10) in which the equivalent heat transfer coefficient, h, models the effect of the radiant and convective heat transfer between the bridge and the surrounding environment. The constant λ in (7) represents a dimensionless reference pressure difference across the interface which for this system is determined by the following constant volume constraint [9,16]

$$V = \int_{\frac{-\Lambda}{2}}^{\frac{\Lambda}{2}} \pi R^2(z)dz = V_o \equiv \text{constant}. \tag{11}$$

Finally, the condition that the contact lines between the liquid end disks are fixed is

$$R = 1 \text{ at } z = \pm \Lambda/2. \tag{12}$$

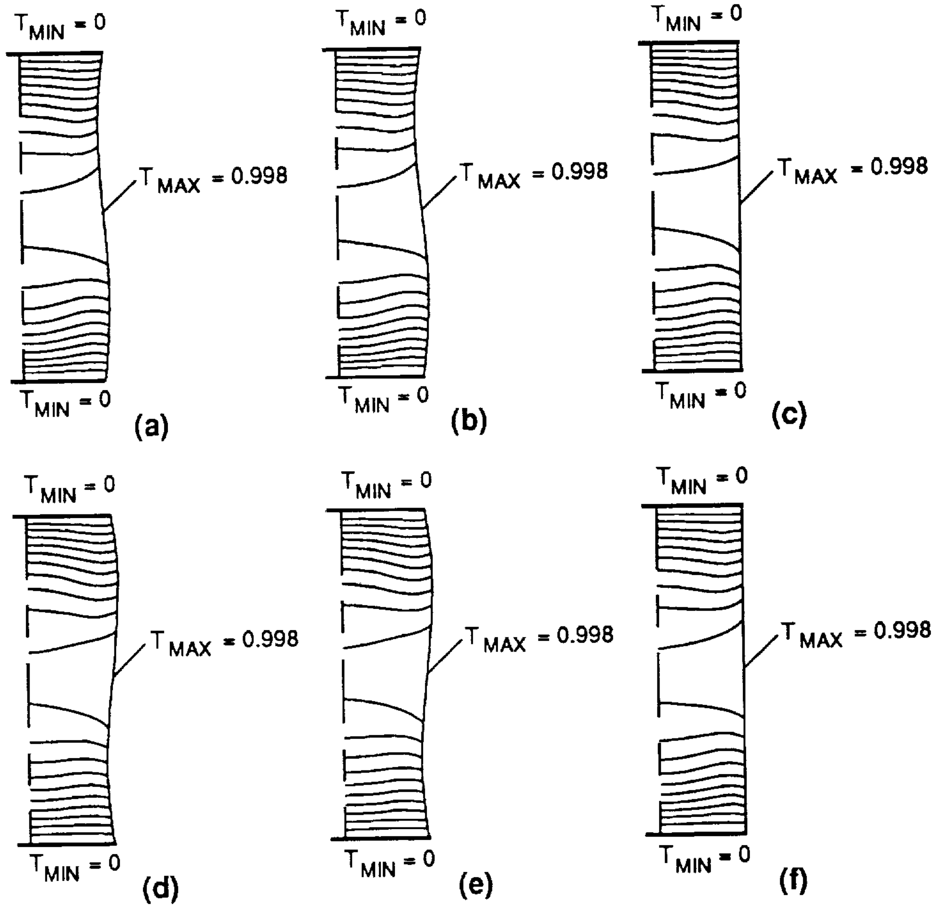

$T_{MIN} = 0$
$T_{MAX} = 0.998$
$T_{MIN} = 0$
(a)
$T_{MIN} = 0$
$T_{MAX} = 0.998$
$T_{MIN} = 0$
(b)
$T_{MIN} = 0$
$T_{MAX} = 0.998$
$T_{MIN} = 0$
(c)
$T_{MIN} = 0$
$T_{MAX} = 0.998$
$T_{MIN} = 0$
(d)
$T_{MIN} = 0$
$T_{MAX} = 0.998$
$T_{MIN} = 0$
(e)
$T_{MIN} = 0$
$T_{MAX} = 0.998$
$T_{MIN} = 0$
(f)

Fig. 4. The dimensionless temperature field with Re = 2899, Gr = 0.98, $\Lambda = 4$ and Pr = 0.0127, at (a) 0.52 s, (b) 0.59 s, (c) 1 s, (d) 1.5 s (e) 1.56 s, (f) 2 s, after application of an additional 2.5×10^{-2} g, 0.5 Hz, axial acceleration.

2.3 Solution Method

In the present investigation, the governing equations are recast in terms of a stream-function vorticity formulation. The stream-function is defined by

$$u = \frac{1}{r}\frac{\partial \Psi}{\partial z}, \quad v = -\frac{1}{r}\frac{\partial \Psi}{\partial r}. \qquad (13)$$

A non-orthogonal coordinate transformation,

$$\eta = z \ , \quad \xi = \frac{r}{R(z,t)}, \qquad (14)$$

allows an irregular free boundary to coincide with a cylindrical coordinate line (or surface) without the need to solve a coupled set of Laplace equations [17,18]. The resulting equations are discretized following a semi-implicit difference scheme and solved by the A.D.I. method. The conditions for force balance tangent to the surface and kinematic condition at the free surface are solved along with the Navier-Stokes and continuity equations. The condition for the force balance normal to the surface is used together with an "outer" iterative procedure to determine the free surface shape.

The unsteady free boundary problem for a cylindrical liquid zone is solved as follows. The

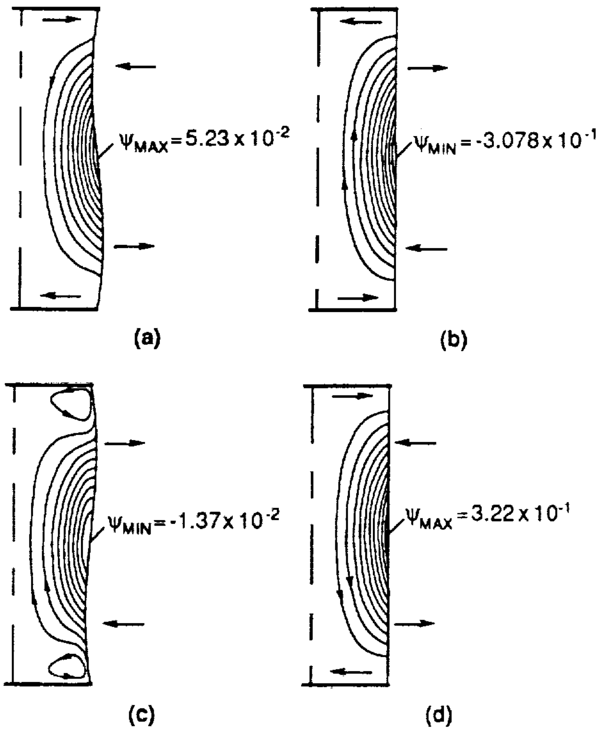

Fig. 5. The instantaneous dimensionless stream-function, with Re = 0, Gr = 0, $\Lambda = 4$ and Pr = 0.0127, at (a) 0.59 s, (b) 1 s, (d) 1.5 s (e) 2 s, after application of an additional 2.5×10^{-2} g, 0.5 Hz, axial acceleration. Note that for this case only, $\Psi = \tilde{\Psi}/\kappa R_0$, where $\tilde{\Psi}$ is the dimensional stream-function cm^3 s^{-1}.

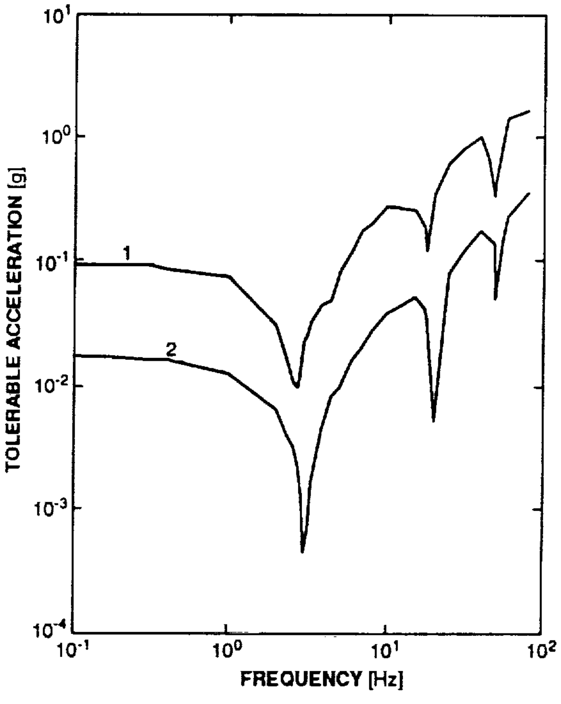

Fig. 6. Tolerable acceleration [g] vs. Frequency [Hz] predicted by the 1D model [15] for (1) breakage and (2) 10% shape change, for an isothermal liquid zone with $\Lambda = 4$ and the thermophysical properties of indium.

initial conditions correspond to either zero or finite steady residual acceleration situations with a steady thermocapillary flow. These states are calculated using a method close to that described below [16]. For the unsteady calculation our solution scheme is similar to that used by Kang and Leal [17] and Ryskin and Leal [18]. The following Picard iterative procedure [19] is adopted:

1. guess the free surface shape for the new timestep;
2. obtain the approximate temperature and stream-function, vorticity and velocity fields by transforming the governing equations and boundary conditions to a circular cylindrical domain via a non-orthogonal transformation and solve them using a semi-implicit method;
3. obtain the pressure at the free surface by integrating the transformed momentum equation;
4. use the condition for the balance of force normal to the free surface to decide how to update the free surface location;
5. return to step 2. Repeat until convergence is obtained by satisfying all equations and boundary conditions to a specified degree of accuracy for this timestep.

3. Results and Discussion

The following results were obtained for a liquid zone corresponding to the physical properties of molten indium subject to an axial acceleration with a frequency of 0.5 Hz. Fig. 2 depicts the initial state of the system. A steady axial acceleration of magnitude 10^{-4} g (10^{-3} m s^{-2}) acts along the negative z-direction. Two equidimensional toroidal rolls indicate that surface-driven flow is dominant (Re = 2899, Gr = 0.98). The isotherm distribution shows that heat transfer is mainly by conduction, although some distortion of the isotherms by the flow is evident. For indium, Lind [20] has reported that the surface tension increases with increasing temperature i.e. $\gamma_T > 0$. (Note that surface contamination may have affected the measured temperature dependence of surface tension in this case.) Thus, the flow direction at the surface is toward the center (i.e. the higher temperature region). Figs. 3 and 4 illustrate the effect of an additional acceleration component which varies sinusoidally with a frequency of 0.5 Hz. Figure 5 depicts the response of the zone to the same disturbance, but with Gr = Ma = 0. (Note that, for this case, κ/L rather than $|\gamma_T| \Delta T/\mu$ was used as the velocity scale.) In another case with Re = 2899, Gr = 0.98 and the surface constrained to be a circular cylinder, no observable response occurred. Clearly the system is more sensitive to the effects of free surface motion than internal buoyancy. Given that the value of steady acceleration used is extreme for spacecraft acceleration environments [21], we may conclude that for systems where internal buoyancy-driven effects are not manifested (in this case because they are swamped by the surface-driven flow) it suffices to examine the response of the free surface only. Furthermore, a comparison of our full axisymmetric results with those obtained with a simplified 1D isothermal model indicates that, at least for the conditions examined, the 1D model may be used to reliably predict liquid zone (isothermal and nonisothermal) sensitivity. The 1D model is described in detail in [15]. Fig. 6 shows the sensitivity of an indium liquid zone to axial acceleration. The curves are based on results obtained using two sensitivity criteria. The first is determined by breakage of the bridge, the second is whenever the bridge shape changes by more than 10% of its static shape, i.e. $R(z,t) - R(z,0) = .1R(z,0)$.

Acknowledgements

This work was supported by the State of Alabama through the Center for Microgravity and Materials Research and the Alabama Supercomputer Network, and by the National Aeronautics and Space Agency through grant NAG8-724.

4. References

[1] W.G. Pfann, *Zone Melting*, Krueger, Huntington New York (1978).
[2] C. Chang and W.R. Wilcox, J. Crystal Growth **28**, 8-12 (1975).
[3] P.A. Clark and W.R. Wilcox, J. Crystal Growth **50**, 461-469 (1980).
[4] N. Kobayashi, J. Crystal Growth **66**, 63-72 (1984).
[5] W.W. Fowlis and G.O. Roberts, J. Crystal Growth **74**, 301-320 (1986).
[6] A. Rybicki and J.M. Floryan, Phys. Fluids **30**, 1956-1972 (1987).
[7] R. Natarjan, AIChE J. **35**, 614-624 (1989).
[8] Z. Kozhoukharova and S. Slavchev, J. Crystal Growth **74**, 236-246 (1986).
[9] J.L. Duranceau and R.A. Brown, in Taylor G. Wang (ed.) *Drops and Bubbles Third International Colloquium 1988*, AIP Conference Proceedings **197**, American Institute of Physics, New York, 1989, pp. 133-144.
[10] C.W. Lan and S. Kou, J. Crystal Growth **102**, 609-627 (1990).
[11] D.T.J. Hurle, G. Müller and R. Nitsche, in *Fluid Sciences and Materials Science in Space*, Ed. H. U. Walter (Springer Verlag, Berlin, 1987) pp. 313-351.
[12] A. Cröll, W. Müller and R. Nitsche, *Proceedings of the 6th European Symposium on Materials Sciences under Microgravity Conditions*, ESA **SP-256** (ESA Publications Division, Noordwjyck, 1987) 87.
[13] I. Martinez, J.M. Haynes and D. Langbein,in *Fluid Sciences and Materials Science in Space*, Ed. H. U. Walter (Springer Verlag, Berlin, 1987) pp. 53-80.
[14] I. Martinez, *Proceedings of the 6th European Symposium on Materials Sciences under Microgravity Conditions*, **ESA SP-256** (ESA Publications Division, Noordwjyck, 1987) 235.
[15] Y.Q. Zhang and J.I.D. Alexander, *Physics of Fluids A* **2**, 1966 (1990).
[16] Y.Q. Zhang and J.I.D. Alexander, *International Journal for Numerical Methods in Fluids* in press.
[17] I.S. Kang and L.G. Leal, *Physics of Fluids* **30**, 1929-1940 (1987).
[18] G. Ryskin and L.G. Leal, *J. Fluid Mech.* **148**, 1-17 (1984).
[19] J.M. Floryan, *Appl. Mech. Rev.* **42**, 323-341 (1989).
[20] M.D. Lind, *Proceedings of the AIAA 25th Aerospace Sciences Meeting, Reno, Nevada,* AIAA-87-0618 (1987).
[21] J.I.D. Alexander, *Microgravity Science and Technology* **3**, 52 (1990).